# Synthesis and characterization of free standing Pt-Rh nanoparticles, and 2 wt. % $Pt_{0.70}Rh_{0.30}/Al_2O_3$ and 20 wt. % $Co_{1-x}Re_x/Al_2O_3$ ($0.00 \leq x \leq 0.15$) metal-on-support catalysts

Marte Eiterstraum Muri


Master thesis in Materials science and nanotechnology

60 credits

Department of Physics

Faculty of Mathematics and Natural Sciences

UNIVERSITY OF OSLO

January 26, 2015

**Acknowledgements:**
The process of this Master thesis has been equally challenging and rewarding. There were periods during the process that was difficult which created a feeling of hopelessness, while on the other side, the feeling of overcoming those obstacles was equally filled with joy. Looking back at this rollercoaster, there are certain inviduals who have contributed for bringing me to this point, and for that I am ever so grateful.

First and foremost, my thanks goes to my supervisor Anja, who's door was always open for small and large questions, who patiently guided me in the right directions and retrieved me when I was off my path. Also to my secondary supervisor, Eirini with her incredible teaching skills and patience, thank you for all your help in getting me from the very start to the finish line. Also thanks to my supervisor Helmer, for bringing new ideas to the plate.

I am also grateful to the girls in the office, four countless hours of fun and joy, and for cheering me on until the end. And to all the guys in the hall who, in addition to making the workday so much fun, all at some point have helped me along the way with good advice, and with different computer problems.

Thank you to my parents, who's support and cheering along the way has gotten me so far. And to my fiancé, a big thank you for picking me up every time I fell down, for loving me and caring for me and for helping me through every step of the way, Thank you! This thesis would not be finished without you.

**Abstract**

In this project three different chemical systems are investigated with respect to synthesis and characterization; $Pt_{1-x}Rh_x$ ($0.00 \leq x \leq 1.00$) nanoparticles (~5-17 nm), 2 wt. % $Pt_{0.70}Rh_{0.30}/Al_2O_3$ catalysts for ammonia oxidation and 20 wt. % $Co_{1-x}Re_x/Al_2O_3$ ($0.00 \leq x \leq 0.15$) catalysts for Fischer-Tropsch catalysis.

An apparatus for synthesis of monodisperse metallic nanoparticles by the 'polyol' route is constructed, and the synthesis route is established. $Pt_{1-x}Rh_x$ nanoparticles have been produced. The effect of reaction time (0.5 – 3 h) and reaction temperature (190 – 230 $^oC$) on particle size and particle size distribution are studied, keeping other essential parameters constant (metal salt precursor(s): surfactant ratio, dilution, type of solvent and surfactant). All samples have been characterized by PXD to inspect sample purity, to extract unit cell dimensions as well as to estimate particle size. Evaluations of the variation in unit cell dimensions (a-axis) with degree of Rh substitution (x) indicate that the particles form a complete solid solution. High resolution SEM is used to map the particle size distribution (typically analyzing 200 particles per sample) and to study particle morphology. For some few selected samples DLS is used to evaluate the freshly synthesized particles in suspension.

Four different 2 wt. % $Pt_{0.70}Rh_{0.30}/Al_2O_3$ catalysts are produced. The catalysts are produced by depositing free standing $Pt_{0.70}Rh_{0.30}$ particles onto two different supports. The nanoparticles are synthesized using two different approaches to synthesise nanoparticles the 'round-flask' and 'microwave' method. Both methods are based on that metal nanoparticles are produced by reducing the corresponding metal salt precursors. Morphology of the nanoparticles from the synthesis step to the ready catalysts are evaluated together will how well the particles are dispersed on the $Al_2O_3$ support. TEM, 1. BET, ICP-MS and PXD have been used in the characterisation work. The catalysts will at a later stage be externally evaluated for ammonia oxidation.

By means of *incipient wetness* impregnation some 20 wt. % $Co_{1-x}Re_x/Al_2O_3$ ($0.00 \leq x \leq 0.15$) catalysts are prepared. The samples were calcinated and reduced after the impregnation step. PXD is used investigate phase content of the samples after both the calcination- and reduction step. The materials will be used in an up-coming SXRD experiment at ESRF in Grenoble, France.

# List of abbreviations

BET - Brunauer, Emmet and Teller ‘

DLS- Dynamic Light Scattering

FTS- Fischer-Tropsch Synthesis

GTL -Gas to liquid

NP- Nanoparticle

PXD – Powder x-ray diffraction

SEM- Scanning Electron Microscope

TEM- Transmission Electron Microscope

## Table of contents

# 1. Introduction

The world population is more than 7 billion people,[6] all needing food on a daily basis. Further, both in the industrialized and the developing countries we rush to improve our living standard and material goods. An optimized chemical-, petrochemical- biochemical process industry together with environmental protection is called for to meet our needs and demands with respect to food production, energy, medical care and other high technology products. Most chemical processes are catalysed and optimized by including one or more catalysts in the production line; being either heterogeneous or homogeneous. E.g. in the $HNO_3$ production, which is an important chemical in the fabrication of nitrate based fertilizers, more than 20 different heterogeneous catalysts are added for the process optimization, several of them being composed of metallic nanoparticles deposited onto a support material.

In the methanization process for production of substituted natural gas (SNG), typically coal and biomass is converted to methane over a nickel-on-alumina catalyst. This process is of high importance in areas with big coal resources or where natural gas is spare. For health hazard considerations the produced methane gas must not contain more than 0.1 % CO. I.e. for this reason SNG is always shifted over high temperature and low temperature water gas shift reactions to reduce the CO content.[7]

The production of petroleum from synthesis gas, discovered by Fischer and Tropsch back in the1920's was of eminent importance for Germany under the World War II and more recently from around 2005 in parts of Africa. This process is referred to as Fischer-Tropsch synthesis (FTS), and is also catalysed by a heterogeneous metal-on support catalyst.[8] Catalysts for car exhaust is of importance to deal with the toxic carbon monoxide (CO) and the greenhouse gas nitric oxide, which are produced during fuel combustion. For this purpose, bimetallic particles of platinum and rhodium supported on a ceric oxide-alumina mixed oxide ($CeO_2/Al_2O_3$) has shown to be effective,[7] and the deactivation of this catalyst when in contact with lead is the reason gasoline no longer contain lead.[9] By these few examples alone, the importance of metal-on-support catalysts for industrial processes is understood, In the following, as an introduction to the objective of this work, a more detailed introduction to the chemistry and catalysis around the $HNO_3$ production and the Fischer-Tropsch synthesis will be given together with an overview of the state-of-the-art of the synthesis of free standing PtRh nanoparticles and selected metal-on-support catalysts.

## 1.1Nitric Acid Production

Nitric acid, $HNO_3$, is the starting material used for the production of nitrogen fertilizers, nylon, many dyes, explosives, and all organic compounds for nitration. For this reason $HNO_3$ must be available in large quantities.[10, 11] Nitric acid, $HNO_3$, is made via the so-called Ostwald process, and in this process heterogeneous catalysts play an important role.[10] During this process, ammonia ($NH_3$) is converted through three main steps to nitric acid, as described in equations I-III:

$$4NH_3(g) + 5O_2(g) = 4NO(g) + 6H_2O(g) \qquad \text{(Eq. I)}$$

$$2NO(g) + O_2(g) = 2NO_2(g) \quad \text{(Eq. II)}$$

$$3NO_2(g) + H_2O(l) = 2HNO_3(aq) + NO(g) \quad \text{(Eq. III)}$$

The first of these steps (Eq. I), most often operated between 1 to 9 atm and in the temperature range from 800 to 900 $^{o}$C, produce two side products ($N_2O$ and $N_2$) in addition to the targeted NO molecule. In order to suppress formation of the two side products, design of catalysts with strong selectivity control is therefore necessary. Not only to increase the output of the reactions, but also to minimize the formations of unwanted by-products, like the greenhouse gas $N_2O$. The selectivity of NO over $N_2O$ and $N_2$ has a current efficiency in the range 94-98 %, depending on the choice of process temperature, pressure and catalyst. This first step is often catalysed by gauzes woven from thin platinum - rhodium threads. However during the exothermic reaction, platinum and rhodium is lost as oxides ($PtO_2$ and $Rh_2O_3$ respectively) due to their volatility, and reconstruction of the catalyst is observed as seen in Figure 1.[11-14] The observed morphology on the spent Pt gauge shown in Figure 1 is often named cauliflowers. The described noble metal loss is a technological challenge, and important $HNO_3$ production actors are searching for mitigations to reduce the metal loss of the current Pt-Rh gauges. In addition, efforts are put into the development of completely new materials. Some oxide-based catalysts have been shown to oxidise ammonia to nitric oxide (NO) with less formation of the greenhouse gas $N_2O$.[13] Research has revealed cobalt oxide, iron oxide and chromium oxide as good catalysts with a lower selectivity towards nitrous oxide than that of platinum gauzes, however, the oxides show a lower conversion efficiency.[11] Mixed metal oxides like $CeO_2$-$TiO_2$ and several different perovskites have also been investigated for this purpose. Previous work has been done on $LaCoO_3$, $LaFeO_3$, $LaMnO_3$, amongst others showing promising results in the higher temperature reactions (+1000 $^{o}$C)[11]. Pérez-Ramírez and Vigeland have synthesised $LaFeO_3$ perovskite membranes, giving NO selectivity up to 98 % (with the remaining 2 % being $N_2$) and with no $N_2O$ formation.[13] Noble metal nanoparticles supported on oxides ($\alpha$-$Al_2O_3$ or $\gamma$-$Al_2O_3$) and mixed oxides ($CeO_2$ -$TiO_2$), have also shown good conversion efficiency and selectivity for selective oxidation of ammonia to nitric acid even at lower temperatures (+800 $^{o}$C).[12] In this particular study, the nanoparticles were first synthesized as free standing nanoparticles before they were anchored onto the support (see chapter 2.2.1 for more details on the approach). With a loading of only 0.2-0.5 wt. % of noble metal on support being sufficient,[10] cost is greatly reduced. A summary of the NO selectivity and the product distribution for Pt gauzes, Pt/$\alpha$-$Al_2O_3$, Pt/$CeO_2$ -$TiO_2$ and $CeO_2$ is given in Figure 2.[12]

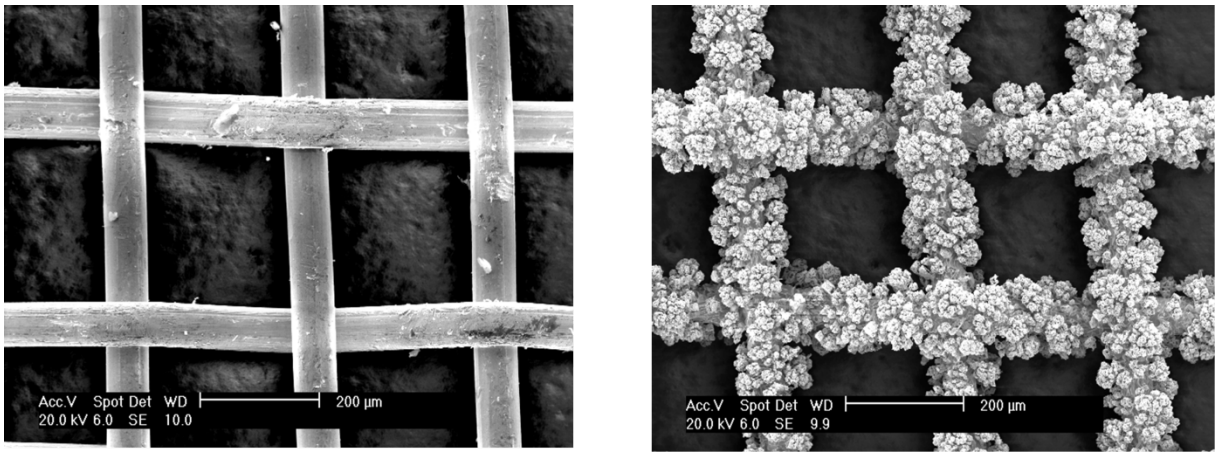


**Figure 1. Pt gauzes used for selective oxidation of ammonia to nitric acid (see Eq. I), before (left) and after (right) laboratory scale testing. After reaction a cauliflower reconstruction of the surface has occurred. (Ref internal results, UiO)**

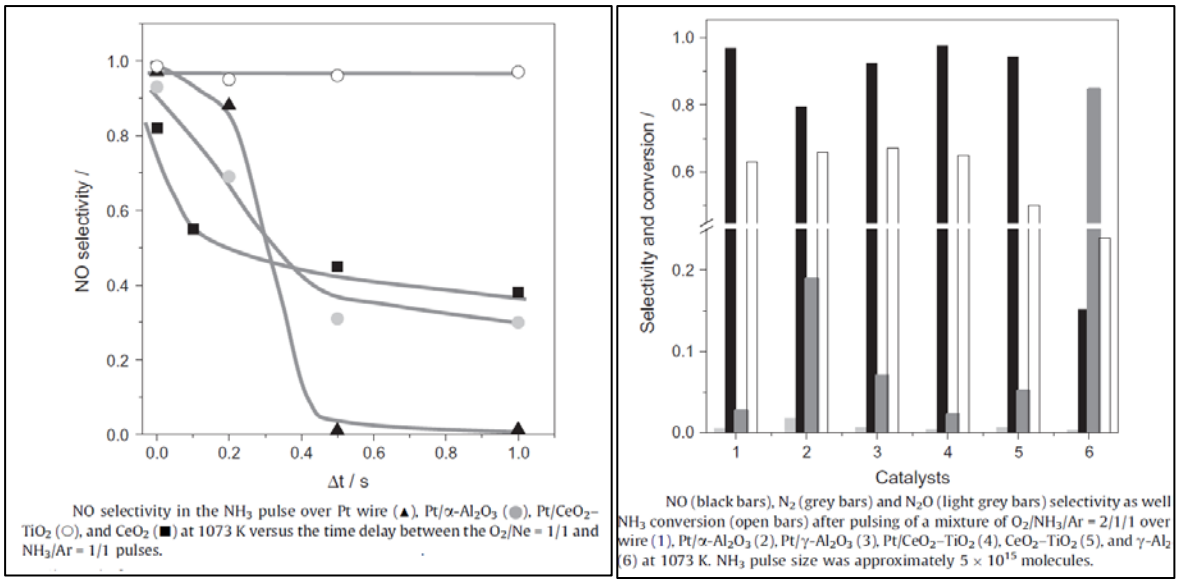


**Figure 2. Left, the NO selectivity in NH3 conversion for different catalysts. Right, the selectivity of different products (NO, N2 and N2O) of NH3 conversion from a TAP test. [12]**

## 1.2Fischer-Tropsch Synthesis

The Fischer-Tropsch technology was developed by Franz Fischer and Hans Tropsch in the 1920's[15] using iron and cobalt based catalysts.[7] The Technology uses a mixture of CO and $H_2$, known as synthesis gas, as reactants to produce paraffins (alkanes), olefins (alkenes) and small amount of oxygenates (alcohols, ethers) (Eq. IV-VI).[8, 15] Factors affecting the product distribution are the nature of the catalyst, residence time as well as reaction-temperature and pressure. Typically, the FT process is operated in the temperature range from

150 $^{o}$C to 300 $^{o}$C. Methane formation (Eq. VII) is favoured at higher temperatures, which is an undesired side product in this gas-to-liquid process (GTL). Further, the synthesis of the long chained hydrocarbons is operated at moderate temperatures (~ 20-30 atm.).[15] Higher pressures would be favourable with respect to products, but on the other hand higher pressures can lead to catalyst deactivation via coke formation.

The reactions that takes place in the Fischer-Tropsch synthesis (FTS) are highly exothermic,[15] and the total reaction for production of paraffins (Eq. IV), olefins (Eq. V) and oxygenates (Eq. VI) are as follows[8]:

$$nCO\ (g) + (2n+1)H_2\ (g) = C_nH_{2n+1}(l) + nH_2O\ \ (l) \qquad \text{(Eq. IV)}$$

$$nCO\ (g) + 2nH_2\ (g) = C_nH_{2n}(l) + nH_2O\ (l) \qquad \text{(Eq. V)}$$

$$nCO\ (g) + 2nH_2\ (g) = C_nH_{2n+2O}O\ (l) + (n-1)H_2O\ (l) \qquad \text{(Eq. VI)}$$

Some side effects also follow in addition to the methane formation (VII), namely the water-gas shift reaction (Eq. VIII) and the Boudouard reaction (Eq.IX).

$$CO\ (g) + 3\ H_2\ (g) = H_2O\ (l) + \ CH_4\ (g) \qquad \text{(Eq. VII)}$$

$$CO\ (g) + H_2O\ (l)\ = CO_2(g) + H_2\ (g) \qquad \text{(Eq. VIII)}$$

$$2CO\ (g) = C(s) + CO_2\ (g) \qquad \text{(Eq. IX)}$$

For the Fischer-Tropsch synthesis (FTS), tree reactor types are commonly used; the fixed bed reactor, the slurry reactor and the circulating fluidised bed reactor, all with their pros and cons with respect to economy, temperature control and the scale of the production. The fixed bed reactor and the slurry reactor are the ones commonly used in FTS plants today.[8, 15] The tree different reactors are illustrated in Figure 3.

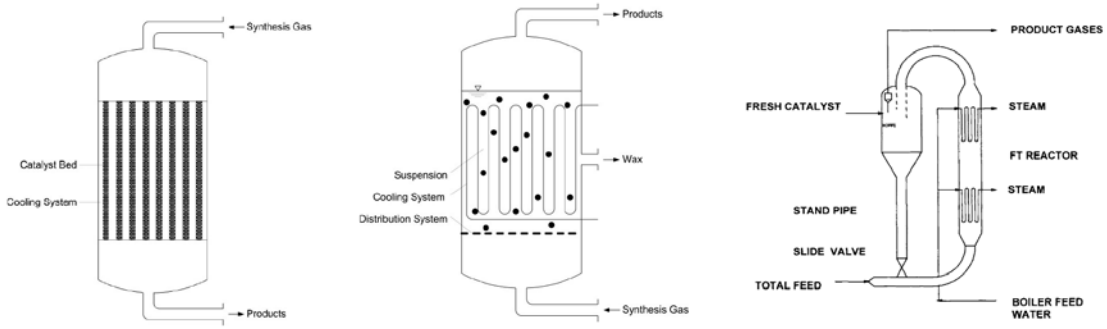


**Figure 3. The three common rector types for the Fischer-Tropsch synthesis, staring from left; the fixed bed reactor, the fluidised bed reactor and the circulating fluidized bed reactor. [4]**

The most common Fischer Tropsch catalysts today are based on nanoparticles of ruthenium, cobalt, and iron, on different supports.[8, 15] Tuning size and shape of the nanoparticles can affect both the activity and the selectivity of the FT catalyst.[16] Ruthenium is costly and is limitedly available, and iron is kinetically hindered by the presence of water. The cobalt based catalyst is effective also at low temperatures, has a long durability and has a low selectivity towards the water gas shift reaction. For these reasons Co is commonly preferred over the other catalytic components. Reformation of CO by Co catalysts has a broad spectrum of products from C5 and above. Also, further treatment is often needed to get the desired product.[8, 15] Both Shell and Statoil have developed Co based Fischer-Tropsch catalysts. The catalytic active metal is often used in combination with a promoter like platinum, palladium, rhenium and ruthenium. The metal component(s) are e.g supported on oxides like alumina, silica and titanium dioxide (titania).[15] Several plants are found around the world, including the Pearl GTL in Quatar (Shell), the Escravos GTL= in Nigeria (Sasol-Chevron) and Mossel Bay in South Africa (PetroSA)

The first generation commercial FT catalyst that Statoil developed is based on cobalt nanoparticles promoted with rhenium and deposited on a $\gamma$-$Al_2O_3$ (see e.g. refs. 17-21). For this specific catalyst, the metal components were deposited via a wet impregnation approach (see section 2.4). Important points to address in the research was to find which role Re plays as promoter, to tracing the origin of catalyst deactivation as well as to find support materials with good mechanical strength. [17-21]

## 1.3 Previous Work on Platinum Rhodium Nanoparticles

Cluster research dates back to the mid-19$^{th}$ century, and laid out the line for what is now known as nanoparticles. In 1857, Faraday held a legendary lecture about colloidal gold and its interactions with light, now known to be caused by nanoparticles of gold with various sizes.[22] He was the first to enlighten the scientific world about aqueous metal nanoparticles, and since then colloidal nanoparticles have been synthesised through several routes. There are several approaches to synthesising colloidal metallic nanoparticles such as; the hydrothermal method, soft and hard templating methods, the sol-gel process and the polyol method. Resent breakthroughs in metal nanoparticle synthesis has opened the door for much research into controlling size, shape, and composition.[23, 24] In the present project some variants of the polyol route is applied, the so-called 'round flask polyol'- and the 'microwave polyol' synthesis route. The principles behind these methods are described in detail in sections 2.1.1 and 2.1.2. In the following an overview of state-of-the art with respect to PtRh nanoparticle synthesis using these approaches is presented.

In Table 1 an overview of reported characteristics of obtained $Pt_{1-x}Rh_x$ particles synthesised using the 'round flask' approach at different conditions is presented (reaction temperature, reaction time, metal ratio, as well as metal-to-solvent ratio).[25-28] Overall, the reported average nanoparticle sizes (*D*) vary from 5.7 to 11.4 nm. Park *et al*. (ref Nano Letters 2008) synthesized alloyed PtRh nanoparticles covering the entire solid solution range, $Pt_{1-x}Rh_x$ (0.0

≤ x ≤ 1.0). In Figure 4 the obtained powder X-ray diffractograms of the as-synthesized particles are presented and all compositions are reported to crystallize in a face centred cubic packed (fcc) structure. In this study Park *et al*. focused on maintaining the PtRh nanoparticle size constant at ~ 9 ± 1 nm for the different compositions. Approximately constant particle sizes were achieved by varying the reaction temperature (185-225 $^{o}$C) and reaction time (1-2 hours), see Table 1.

In a later study, Park and co-workers (ref, 2012) performed a more detailed study of the composition $Pt_{0.5}Rh_{0.5}$. This study reports on how the particle size is influenced by increasing the metal to solvent ratio (0.025-0.200 mmol metal precursors and 20 mL 1,4 butanediol was used) keeping the reaction temperature and reaction time constant at 220 $^{o}$C and 2 hours, respectively. The average particle size, *D*, was found to increase when increasing the metal precursor concentration, see Table 1. For pure Rh nanoparticles, Queck *et al*.(ref) obtained a larger average particle size than Park and co-workers (ref) when they are increasing the reaction temperature, maintaining all other parameters constant (Table 1). All the bimetallic nanoparticles listed in Table 1 were reported as alloys, and all nanocrystals where reported to crystallize with a face centred cubic (fcc) lattice structure. No lattice parameters were reported.

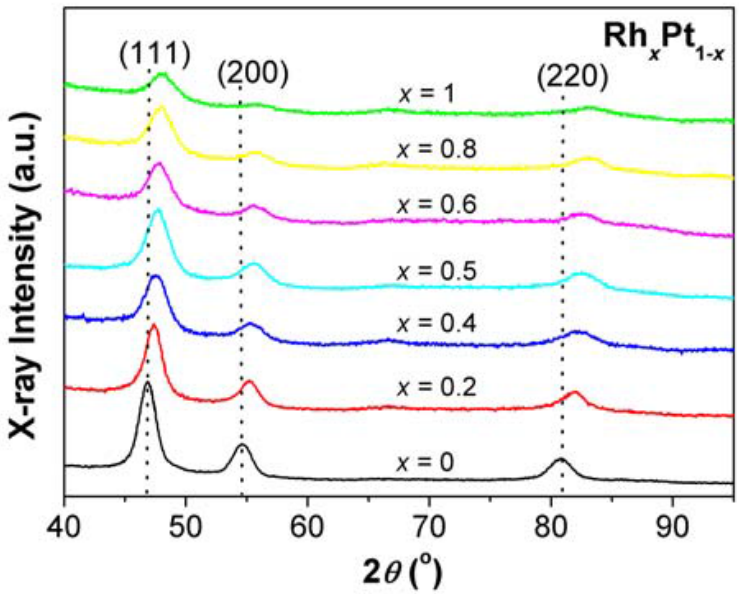


**Figure 4. Powder X-ray diffraction patterns for selected Pt $_{1-x}$Rh$_x$ compositions (Co-Kα radiation, λ = 1.79 Å). Ref Park 2008**

**Table 1. Reported average particle diameters (*D*), determined by means of TEM, of nanoparticles synthesised using the round flask polyol method with 1,4 butanediol as solvent. Note that the reported Pt nanoparticles are synthesized using the $H_2PtCl_6$ rather than the $Pt(acac)_2$, precursor, and Rh nanoparticles as reported by Queck *et al.* (ref) are synthesised using 2 mL of THF in the 1,4 butanediol mixture. For details regarding the round flask polyol method, see section 2.1.1.**

| Reference | $Pt_{1-x}Rh_x$ (x) | ∑( Pt+Rh)mmol/ mmol PVP/ mL solvent | Reaction temp. (°C) | Reaction time (h) | Average size (nm) |
|---|---|---|---|---|---|
| Park *et al.* [25] | 0.0 | 0.100/1.00/20 | 185 | 1.5 | 9.5 ± 0.8 |
| | 0.2 | 0.025/0.25/20 | 225 | 1 | 9.2 ± 2.4 |
| | 0.4 | 0.025/0.25/20 | 225 | 1 | 9.3 ± 1.2 |
| | 0.5 | 0.025/0.25/20 | 225 | 1 | 8.1 ± 0.8 |
| | 0.6 | 0.025/0.25/20 | 220 | 1 | 8.5 ± 0.9 |
| | 0.8 | 0.025/0.25/20 | 225 | 1 | 9.2 ± 1.1 |
| | 1.0 | 0.025/0.25/20 | 215 | 2 | 9.0 ± 0.8 |
| | | | | | |
| Park *et al.* [26] | 0.5 | 0.025/0.25/20 | 220 | 2 | 5.7 ± 0.7 |
| | 0.5 | 0.0125/0.125/20 | 220 | 2 | 6.8 ± 0.6 |
| | 0.5 | 0.100/1.00/20 | 220 | 2 | 8.5 ± 1.1 |
| | 0.5 | 0.200/2.00/20 | 220 | 2 | 11.0 ± 1.7 |
| | | | | | |
| Queck *et al.* [27] | 1.0 | 0.05/1.00/20 | 160 | 6 | 8.1 ± 1.1 |
| | 1.0 | 0.05/1.00/20 | 190 | 6 | 10.2 ± 2.1 |
| | 1.0 | 0.05/1.00/20 | 220 | 6 | 11.4 ± 1.9 |
| | | | | | |
| Grass *et al.* [28] | 1.0 | 1.25/12.50/120 | 225 | 2 | 6.7 ± 0.7 |
| | 1.0 | 5/50/40 | 205 | 2 | 11.3 ± 1.6 |

In Figures 5 and 6 are TEM images of nanocrystals of $Pt_{1-x}Rh_x$, with compositions x = 0.0, x = 0.2, x = 0.4, x = 0.5, x = 0.6, x = 0.8 and x = 1.0 presented, and in Figure 7 are the corresponding histograms obtained by size analysis form the TEM images in Figure 5.[25-27] The magnification of the images makes it difficult to determine the shape of all the nanoparticles precisely, however, some are identifiable: In Figure 5 a, agglomerated Pt nanoparticles can be seen. In Figure 5 b, larger hexagonal particles are visible and in Figures 5 c-f, triangle shaped particles are visible.

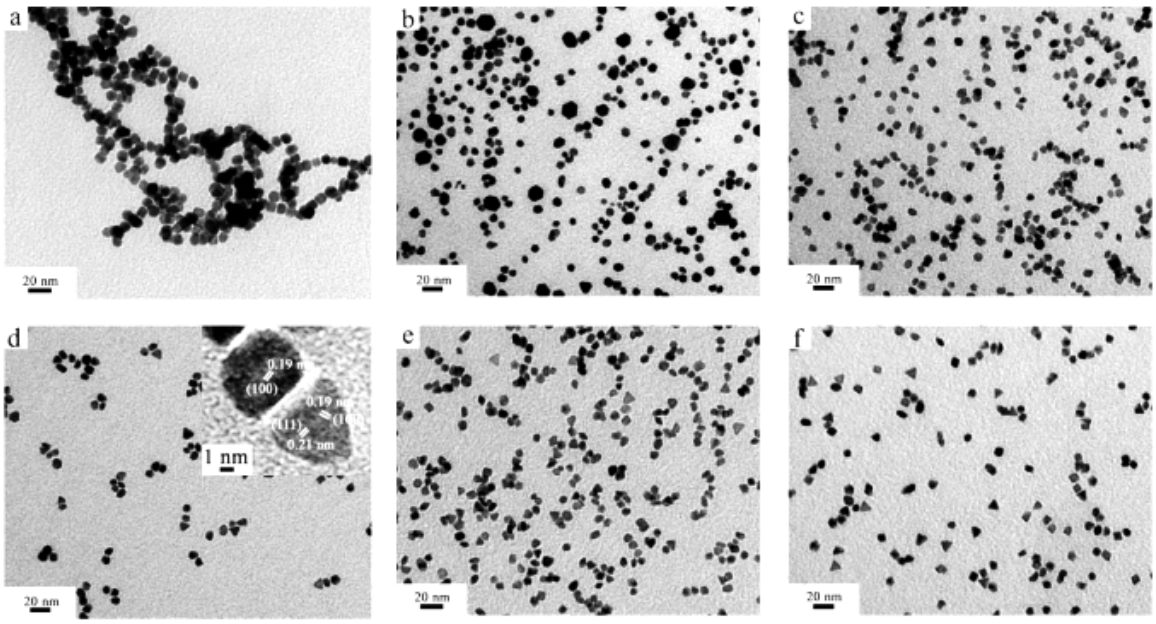


**Figure 5. TEM images of $Pt_{1-x}Rh_x$ nanocrystals: a) x = 0.0; b) x = 0.2; c) x = 0.4; d) x = 0.5; e) x = 0.6; f) x = 0.8. Inset in d) shows HRTEM image of the $Rh_{0.5}Pt_{0.5}$ nanocrystals.[25]**

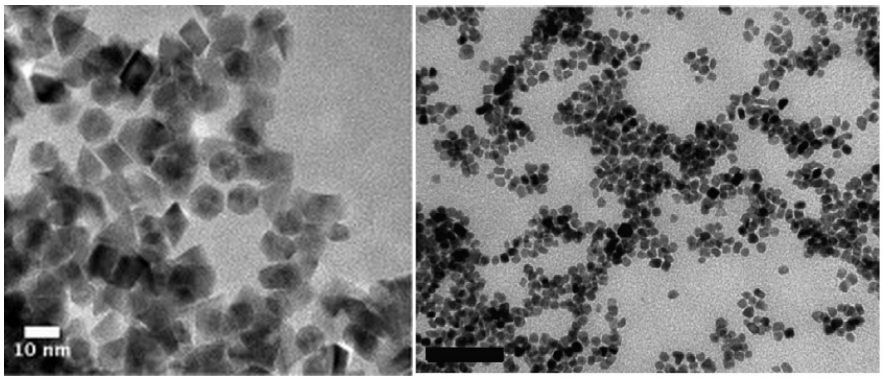


**Figure 6. Left, TEM image of Rh nanocrystals;[27] Right, TEM image of $Pt_{0.5}Rh_{0.5}$.[26]**

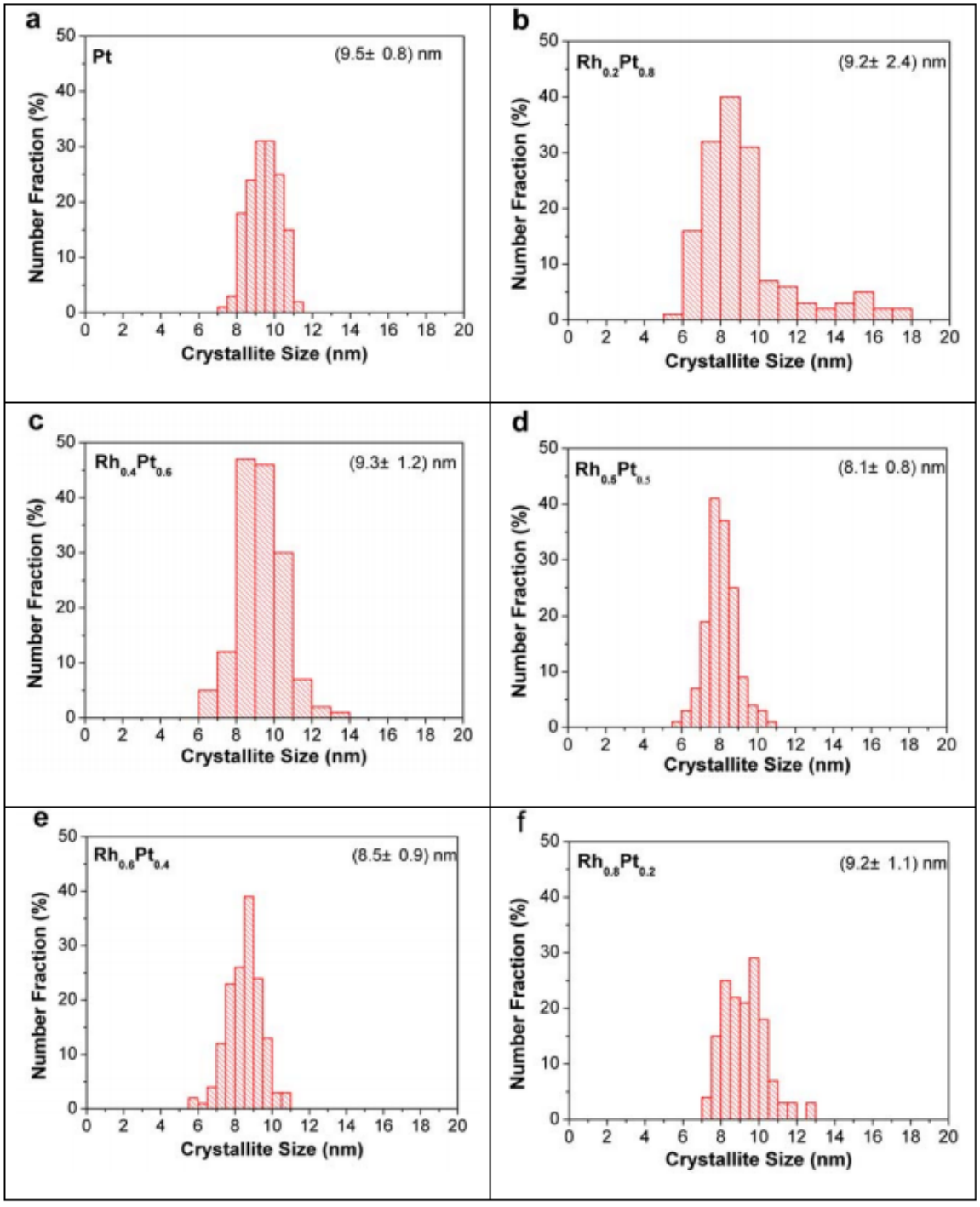


**Figure 7. Size distribution histograms of the $Rh_xPt_{1-x}$ nanocrystals as synthesized by Park et al. (supporting information) [25]. a) x = 0.0; b) x = 0.2; c) x = 0.4; d) x = 0.5; e) x = 0.6; f) x = 0.8**

The polyol microwave process (as described in detail in section 2.1.2) is also used to synthesize PtRh nanoparticles. In Table 2 is an overview of synthesis conditions and reported average sizes (*D*) of $Pt_{1-x}Rh_x$ nanoparticles synthesised using the microwave polyol approach at different conditions (composition, solvents, metal precursors and microwave effect)

presented. The microwave irradiation effect varies between 700 and 800 W, and the microwave irradiation time varies from 60-180 seconds. Shen *et al*.[29] reported sizes varying from 1.7 to 2.6 nm with increasing Rh content in the nanoparticles, and the lattice parameter is decreasing with larger Rh content.

All nanocrystals listed in Table 2 were reported to crystallize in a face centred cubic (fcc) lattice structure. Multiple phased samples or core-shell structures have not been reported for the bimetallic nanoparticles listed in Table 2. Stevanovic *et al*.[30] and Shen *et al*.[29] reported the nanocrystals to be spherical.

**Table 2. Overview of reported average particle size and their corresponding lattice parameter of PtRh nanoparticles synthesized using the microwave polyol method.**

| Reference | $Pt_{1-x}Rh_x$ (x) | Pt- and Rh precursors,Surfactant Solvent,Other additatives | Reaction time (s) Microwave effect (W) | Average particle size (nm) (Method) | *a*-axis (Å) |
|---|---|---|---|---|---|
| Stevanovic *et al*. [30] | 0 | $H_2PtCl_6 \cdot xH_2O$ Ethylene glycol (EG), NaOH, Carbon support added before MWI, | 60 700 | $1.7 \pm 0.3$ (STM) 2.5 (XRD) | 3.944 |
| Patel *et al*.[31] | 0.00 | $Na_2PtCl_4$, PVP, Ethylene glycol, | 60 800 | 30 | n.a |
| Kalyva *et al*.[32] | 0.30 | $PtCl_4$, $Rh(acac)_3$, PVP, OAm, DMF | 600 800 | $12.3 \pm 2.2$ (TEM) | n.a |
| [1]Shen *et al*. [29] | 0.00 | $H_2PtCl_6 \cdot xH_2O$, $RhCl_3 \cdot xH_2O$ EG, Carbon support added before MWI | 180 800 | 1.7 (XRD) | 3.944 |
| | 0.25 | $H_2PtCl_6 \cdot xH_2O$, $RhCl_3 \cdot xH_2O$ EG,, Carbon support added before MWI | 180 800 | 1.7 (XRD) | 3.934 |
| | 0.33 | $H_2PtCl_6 \cdot xH_2O$, $RhCl_3 \cdot xH_2O$ EG, Carbon support added before MWI | 180 800 | 1.8 (XRD) | 3.900 |
| | 0.50 | $H_2PtCl_6 \cdot xH_2O$, $RhCl_3 \cdot xH_2O$ EG, Carbon support added before MWI | 180 800 | 2.0 (XRD) | 3.864 |
| | 0.67 | $H_2PtCl_6 \cdot xH_2O$, $RhCl_3 \cdot xH_2O$ EG, Carbon support added before MWI | 180 800 | 2.4 (XRD) | 3.850 |
| | 1.00 | $H_2PtCl_6 \cdot xH_2O$, $RhCl_3 \cdot xH_2O$ EG, Carbon support added before MWI | 180 800 | 2.6 (XRD) | 3.809 |
| Harada *et al*.[33] | 0.00 | (Metal precursor not stated), PVP EG, HCl | 120 700 | 2.76 (EXAFS) | n.a. |
| | 1.00 | (Metal precursor not stated), PVP EG, HCl | 120 700 | 2.67 (EXAFS) | n.a. |

[1]PtRh nanoparticles synthesized directly onto a C support. Reported unit cell dimensions are calculated on basis on the (110) reflection.

## 1.4 Phase diagram and structural aspects of bulk $Pt_{1-x}Rh_x$ alloys

In Figure 8 the phase diagram for the binary Pt – Rh system is presented. The phase diagram represents the equilibrium situation for bulk $Pt_{1-x}Rh_x$ alloys. According to the phase diagram both Pt and Rh are high melting point ($T_b$) elements with $T_b$ = 1760 $^oC$ and 1963 $^oC$, respectively. Both Pt and Rh crystallize in cubic close packed (ccp) structures with face centered cubic lattices (space group *Fm*-3*m* ), and in Table 3 a selection of reported unit cell dimensions of the two metals is presented. Below solidus and above 760 $^oC$, $Pt_{1-x}Rh_x$ form a complete solid solution. The Hume-Rothery substitution solubility rules states that substitution of one metal into the crystal lattice of another should be possible if the size difference between the two metal radii's are less than 15 percent, they have the same preferred coordination number and they have the same crystal lattice structure.[5] As both Pt and Rh crystallizes with the same crystal structure and the size difference between the atomic radii's are 4 percent (Table 4), the criteria for expecting an existence of a solid solution is fulfilled. However, below 760 $^oC$, the phase diagram suggest that alloys in the compositional range 8 < x (at. % Rh) < 92 are within a miscibility gap, or a two-phase region. Alloys with any given total composition in the given range (and temperature), will be composed of two different phases, one Pt rich phase and one Rh rich phase.

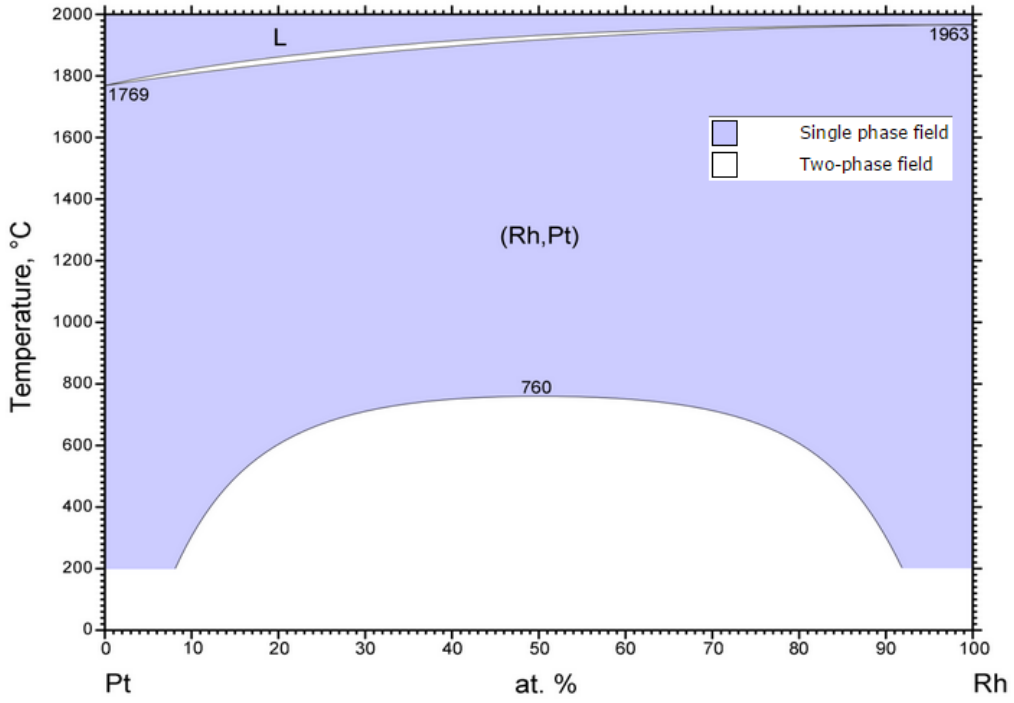


**Figure 8. Phase diagram of the of the binary platinum – rhodium system. [34]**

**Table 3. Reported latiice parameters for bulk of platinum, rhodium and $Pt_{0.50}Rh_{0.50}$**

| References | Pt a-axis (Å) | $Pt_{0.50}Rh_{0.50}$ a-axis (Å) | Rh a-axis (Å) |
|---|---|---|---|
| M. Ellner [35] | 3.922 | | |
| Manoun *et al*.[36] | 3.924(1) | | |
| Korolkov *et al*.[37] | 3.913(2) | | |
| Landolt-Börnstein [38] | 3.9231 | | 3.8043 |
| E. Raub[39] | | 3.863 | |
| E. Raub, G. Falkenburg.[40] | | 3.858 | |
| Shubin *et al*.[41] | | 3.864 | |
| M. Nuding, M. Ellner[42] | | | 3.8033 |
| Ellner *et al*.[43] | | | 3.8019 |
| Schulz *et al*.[44] | | | 3.8045 |

**Table 4. The atomic radii of platinum and rhodium [45], their crystal lattices and coordination number[46]**

| **Metal** | **Metallic Radii ($pm^{-1}$)** | **Crystal lattice** | **Coordination number** |
|---|---|---|---|
| Platinum | 139 | fcc | 12 |
| Rhodium | 134 | fcc | 12 |

## 1.5 Motivation

It is known that chemical and physical properties may become size and morphology dependent at the nanoscale. E.g. catalytic performances of metal-on-support systems depend on metal particle size, particle shape, chemical composition as well as distribution of the atoms if the metal particle is an alloy. In order to investigate performance and optimize industrial catalysts, design and routes to construct high quality model catalysts are called for. One approach towards well-defined model catalysts is to deposit free standing monodisperse metallic nanoparticles with defined shape, composition and atomic arrangement onto the support. Following this philosophy, both routes on how to deposit particles are needed as well as the understanding of how to produce metallic nanoparticles that fulfil the abovementioned criteria are called for.

This master project is part of an ongoing activity in the NAFUMA group with focus on preparation and characterization of nanoparticles and surfaces with applications in chemical process industry. Specifically, in this project attention is given to metallic $Pt_{1-x}Rh_x$ nanoparticles, and model catalysts for ammonia oxidation and Fischer-Tropsch synthesis, 2 wt. % $Pt_{0.70}Rh_{0.30}/Al_2O_3$ and 20 wt. % $Co_{1-x}Re_x/Al_2O_3$, respectively.

The so-called ‘polyol route’ for synthesis of monodisperse metallic nanoparticles will be established in our laboratory, including the design and construction of a synthesis apparatus that is suited for the purpose. In a next step the apparatus will be used to map relevant

synthesis parameters to control particle size and chemical compositions for selected compositions in the $Pt_{1-x}Rh_x$ system. Correspondingly, Pt rich nanoparticles by means of the 'microwave' approach will be synthesized. The obtained well defined $Pt_{1-x}Rh_x$ nanoparticles (by the two routes) may be used to produce high quality model catalysts, by deposition of the free standing nanoparticles dispersed in a suited solvent onto a support material like $Al_2O_3$. Obtained catalysts, 2 wt. % $Pt_{0.70}Rh_{0.30}/Al_2O_3$, will be tested for the ammonia oxidation, but the testing experiments are outside the scope of this project. The third leg of the project is to synthesize and characterize selected 20 wt. % $Co_{1-x}Re_x/Al_2O_3$ catalysts by the *incipient wetness* impregnation method.

Powder X-ray diffraction will be used to determine phase content of samples, unit cell dimensions as well as to estimate crystallite size of nanoparticles. High resolution SEM will be established as a new tool in the NAFUMA group, and the instrument will be used to investigate particle size, particle size distribution and particle morphology. Some few selected samples will be investigated by TEM for the same purpose. If applicable, DLS will be used to investigate stability of particle suspensions and to evaluate hydrodynamic diameters. ICP-MS and 1. BET will be used is some characterization work of the catalysts.

# 2. Methods and Theory

In this chapter, methods and theory on synthesis of free standing nanoparticles, the preparation of the support and the preparation of the alumina supported platinum-rhodium particles and cobalt-rhenium particles will be presented, as well as theory and methods behind the characterisation techniques used for analysis of the nanoparticles, support and catalysts.

## 2.1 Synthesis of Free Standing Nanoparticles

Nanoparticles are defined as particles with dimensions in the nanometre scale, 1-100 $\times$ $10^{-9}$ meter, can be prepared from solutions in in many ways through simple reactions such as direct reaction of ions, decomposition-, precipitation - and redox reaction of metals. If the reactions are carried out in the presence of surfactants, we get what is called surface modified nanoparticles, where inorganic nanoparticles are surrounded, or capped, by organic ligands known as surfactants as illustrated in Figure 9.[47] The capping agent binds to the surface with a "surface-interacting" functional group, common groups include amines ($R_{3-x}NH_x$), carboxylic acid (-COOH), phosphine (-$PH_3$) and phosphine oxides (-$OPX_3$) and more.[24]

Monodisperse bimetallic nanoparticles are metallic particles consisting of two metals, and can consist as colloids. Colloids are any mixtures of two phases, but usually refer to solid particles dispersed in a liquid.[48] In colloidal chemistry, surfactants are used in order to produce stable and well-dispersed nanoparticles. Different surfactants have different bonding abilities depending on the nature of the functional group(s) that attach to the particle. By clever choice of surfactant the size and shape of the nanoparticles can be fine-tuned.[24] Stronger surfactant-particle interactions normally give smaller nanoparticles. Further, high temperature together with a high surfactant to metal precursor ratio favour production of small particles.[23, 24] Other factors of importance for the size, morphology and dispersion of the nanoparticles are the nucleation and growth processes.

Typical for colloidal solutions is that the particles are precipitated from the solution. In the burst nucleation processes it is assumed that no nucleation takes place before the right conditions are in place, and that many small nuclei form simultaneously as soon as the conditions are right, followed by growth, well described by the LaMer theory, and illustrated in Figure 9 b. If the nucleation and growth processes are separated so that no new nuclei are formed during the growth process and no growth occur during the nucleation process, monodisperse particles will be formed. The growth process can be described by Ostwald ripening, where larger nuclei grow on the expense of the smaller ones; smaller particles will dissolve due to the higher solubility of small particles, and 'feed' the larger ones.[23]

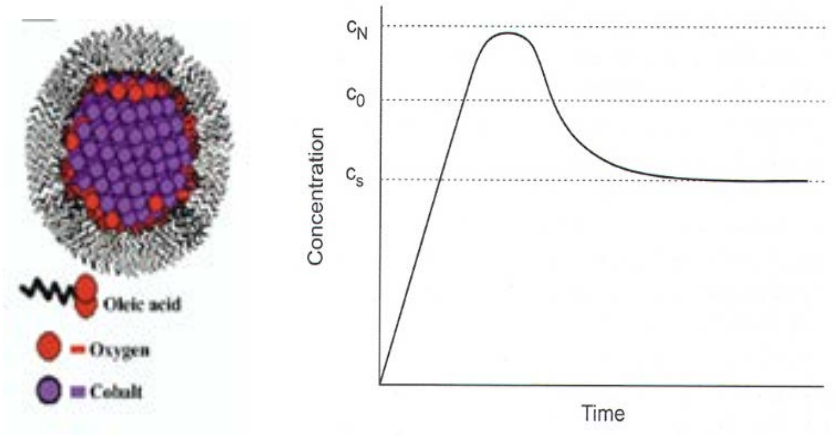


**Figure 9. Left, Capping agents surrounding a cluster of nanoparticles. Right; The process of the LaMer theory. The solution is driven to the critical supersaturation point, where nucleation takes place. The creation of nuclei decreases the saturation below the critical point, and the nuclei begin to grow.**

The nucleation and growth can also be described by thermodynamics. For spherical particles, Gibbs free energy of nucleation, $\Delta G_N$, is dependent on the loss of energy due to increased volume and the gain in energy due to decreased surface area, described by Eq. X;

$$\Delta G_N = \underbrace{\frac{4}{3}\pi r^3}_{\text{Volume of sphere}} \Delta G_V + \underbrace{4\pi r^2}_{\text{Surface area of sphere}} \gamma \qquad \text{(Eq X)}$$

Where;

$\Delta G_V$ = Change in volume free energy pr. unit volume.

$r$ = Crystal radii

$\gamma$ = crystal/liquid interfacial energy

When the nuclei reaches a critical radius, $r^*$, a stable nuclei will be formed. Below the critical radius the particles will dissolve, and above they will grow (Ostwald ripening) as illustrated in Figure 10. Illustration of the dependence of Gibbs free energy of nucleation on volume and surface.[47][23, 47]

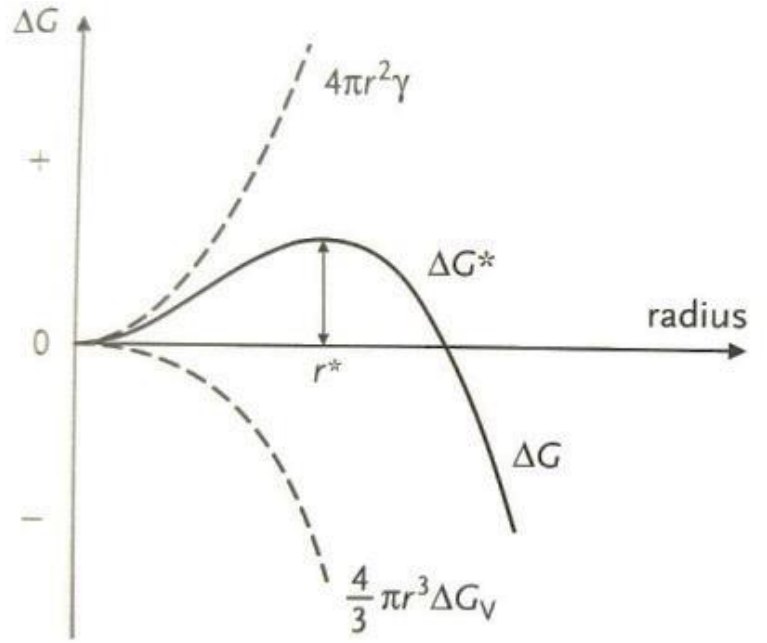


**Figure 10. Illustration of the dependence of Gibbs free energy of nucleation on volume and surface.[47]**

When a nucleation seed is formed, the most stable structure would be the one with minimum surface free energy, i.e. the energy needed for creating a new surface area. E.g. for metallic nanoparticles with the fcc structure, the {111}[1] surface is the thermodynamically most stable, followed by the {100} and {110}, which means that the fcc metallic nanoparticles should form tetrahedral- or octahedral-shaped seeds with {111} facets. However, the surface to volume ratio of a cube is smaller than both tetrahedron and octahedron, and the seeds can form both cubes and truncated octahedrons, so called Wulff polyhedrons. The Wulff polyhedron seeds can grow to form octahedrons, cubeoctahedrons and cubes. Twin formation defects in the seeds can lead to shapes like thin plates, rods and wires.[24] For platinum nanoparticles, cubes, Wulff polyhedrons (truncated octahedrons), rods and octahedrons have been found, and for rhodium nanoparticles, cubes, Wulff polyhedrons, tetrahedrons and truncated tetrahedrons have been found.[49] By varying temperature and reaction time, the nucleation rate can be controlled for a given concentration of precursor in solution.[24]

The choice of surfactant will affect the free growth of the nanoparticles, and thereby also their shape. E.g. the oxygen atoms of the surfactant PVP is known to bind preferentially and strongly to the {100} facets of metallic nanoparticles. This binding affinity facilitates growth in the preferential {111} surface, which leads to formation of cubes. However, since the PVP consist of long, randomly tangled shapes, this effect is not predominant for nanoparticles with sizes smaller than 25 nm.[24] Various shapes have been reported for metallic nanoparticles, including 2D triangles, 3D cubes, tetrahedrons, octahedrons, decahedrons and icosahedron.[24]

[1] The nomenclature is elaborated in section 2.3.

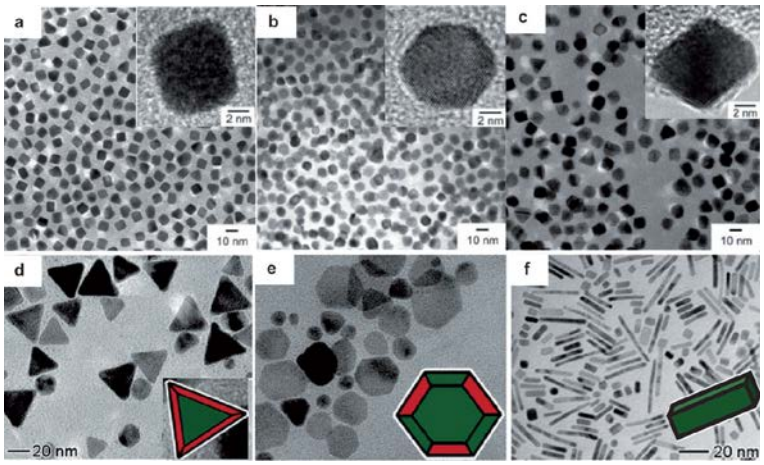


**Figure 11. TEM and high-resolution TEM (insets) images of shape controlled nanoparticles: a) Pt cubes, b) Pt cuboctahedra, c) Pt octahedra, d) Pd triangular plates e) Pd hexagonal plates, f) Pd nanobars.[24]**

Finally, co-reduction of two kinds of metal precursor may give bimetallic nanoparticles with different nanostructuring, as illustrated schematically in Figure 11. *E.g.* by mixing two noble metal precursors among Au, Pt, Pd and Rh a core-shell structure is often obtained, with the tendency of metals to occupy the shell is in the following order Au > Pt > Pd > Rh, and the tendency of metals to occupy the core is the reverse. Formation of bimetallic nanoparticles with the core-shell structure is favored only under mild reduction conditions in the presence of PVP.[50]


**Figure 12. Schematic illustration of possible distribution of elements in a synthesis targeting for a bimetallic nanoparticle. Left panel, elements are mixed on an atomic level forming a solid solution; middle panel, elements are distributed in a core-shell structure; right panel, elements distributed in different particles.**

### 2.1.1 The 'Round-Flask' Polyol Synthesis Route

Four components are essential for colloidal synthesis of metal nanoparticles using the polyol route; the metal salt precursor(s), the surfactant, the solvent, and a reducing agent. In this method the solvent is also acting as a reducing agent- The name of the synthesis route originates from the combined solvent - reducing agent alcohol with multiple hydroxyl groups. In addition, elevated temperature is often used, which is limited by the boiling point of the chosen alcohol.[24] The entire synthesis is carried out under inert conditions to prevent re-oxidation of the formed metallic nanoparticles.

The synthesis itself is typically carried out in a 3-neck round bottom flask with a stirring bar, a thermocouple, an inlet- and outlet for inert gas (typically argon), and a reflux condenser connected to a bubbler. The round flask is heated by a heating block attached to the stirring plate.[24] A photo of the constructed synthesis setup is presented in Figure 13.

The gas inlet on the round flask is connected to a gas manifold with several outlets, which in turn is connected to a flow-meter to maintain a constant gas flow to the round flask, typically 100 mL/min. The temperature in the round flask during the synthesis is controlled by a K-type thermocouple, protected by a glass tube sealed in one end, installed on one of the side arms of the round bottom flask. The temperature is logged by a Fluke 54-II thermometer. The boiling point of the solvent/reducing agent is close to the synthesis temperature, so to manage the vapours a condenser is connected to the round flask. As the solvent/reducing agent used has a narcotic effect if inhaled, special precautions must be made to make sure there is no leakage by introducing a bubbler after the condenser to have a visual control of the effluent. The bubbler is a glass construction where the gas is flown through silicon oil before reaching the outlet, and since this is a somewhat "hard" path for the gas, any leak would be easily visible by the gas no longer bubbling through the silicon oil. The entire set up is located inside a ventilated hood. See Figure 13 for details.

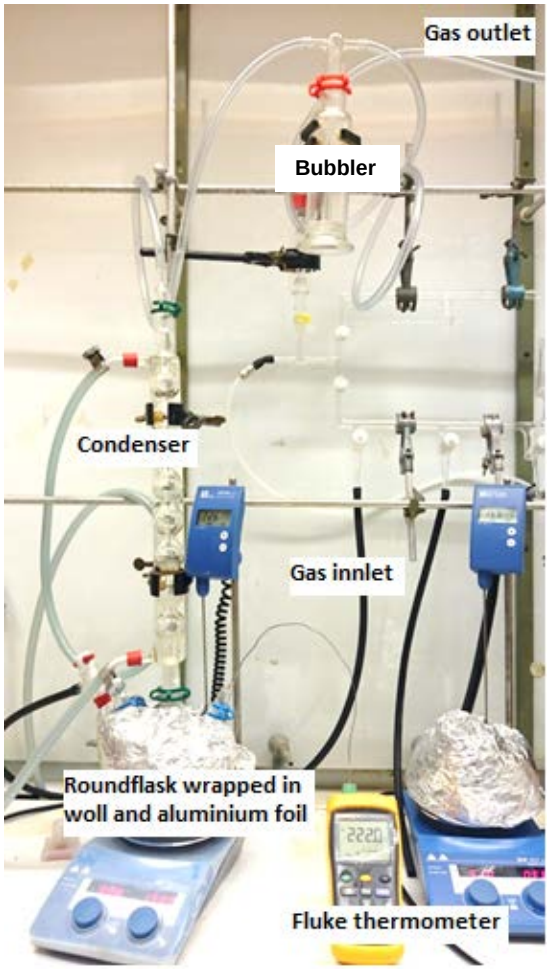


**Figure 13. Image of the synthesis equipment used in the 'round flask' synthesis method. To the left, a round flask wrapped with quartz wool and aluminium foil, connected to a condenser with water inlet/outlet (turqiose tubes) and a bubbler, with the outlet of the bubbler connected to the outlet of the fumehood. In front, thermocouple temperature logger (yellow). In the back, argon inlet (black tube) connected to the synthesis flask.**

In a typical synthesis the metal precursors are weighed out in a ratio to obtain the targeted composition of the metallic nanoparticles together with the surfactant and polyol-solvent. The metal salts and the surfactant(s) are dissolved in the solvent in a 3-neck round flask and heated to remove water and oxygen absorbed in the starting materials. This is done under a flow of inert gas and at stirring conditions. The continuous stirring and the inert gas flow has three purposes; i) facilitate removal of absorbed water and oxygen, ii) make a homogeneous reaction mixture and iii) to ensure the atmosphere in the synthesis flask is inert before the reduction step. At this point the solution is clear with a color consistent with the metal salts used (yellow for Pt and brown-orange for Rh). The liquid is visually examined to determine if the precursors are completely dissolved. The round flask is then transferred to a heating mantle preheated to 20 °C above the targeted reaction temperature to ensure fast heating of the reaction mixture, and hence short nucleation time. The condenser and bubbler are then connected quickly to the transfer arm on the round flask to avoid uncontrolled evaporation of solvent. To help rapid heating and to keep the temperature stable throughout the reaction the round flask is wrapped with quartz wool and aluminum foil. When the temperature in the round flask is 20 °C below target temperature of reaction, the temperature of the heating mantle is decreased to 4-8 °C above target temperature of reaction, °C the temperature of the mantle decreased slowly. With these steps, the temperature of the reaction is stable within a range of $\pm$3°C. After the reaction is completed, a black colloidal solution is obtained.

Once the nanoparticles are synthesised, washing is performed to remove excess surfactant, residues of dissolved and unreduced metal salts and to collect the synthesized nanoparticles. In this connection, the colloidal solution is broken (i.e. flocculate the particles) to separate the nanoparticles from the solvent. Acetone is suited for this purpose for the polyol- synthesis. After completed the flocculation, centrifugation using a high speed centrifuge separates the particles from the solvent. The supernatant is poured out gently to not remove the nanoparticles, and fresh acetone is added for a second washing cycle. After 3 washings with acetone most of the excess chemicals should be removed, and the particles are then brought back to a colloidal solution through re-dispersion.

### 2.1.2 The ‘Microwave’ Synthesis Route

A different approach to synthesise nanoparticles is the microwave (MW) process, in which the metal salt precursors are dissolved in a beaker and placed in the microwave oven, and the electromagnetic waves interact with the dipole moment of the molecules, causing heat.[31] The synthesis is dependent on the solvents ability to absorb microwaves and transfer the energy to heat, and the dielectric properties of the solvent is a critical parameter for the MW synthesis. Microwaves have frequencies in range 300MHz-300GHz, which equals wavelengths of 1-$10^{-4}$ m.[48, 51] Using microwaves as a heating source, the reaction time is shortened with a factor 20 in comparison with the traditional heating method, which may give a narrow size distribution.[31]

During the synthesis, the same 4 components for colloidal synthesis are needed as in the round flask route; surfactant(s), reducing agent, solvent and metal salt precursors. In this case,

the oleylamine functions as surfactant and reducing agent, whilst the PVP and DMF functions as additional surfactant and solvent, respectively.[52]

In a typical synthesis, equimolar concentration of the metallic precursors are dissolved in DMF together with the surfactant PVP. The mixture is kept in an oil bath under continuous stirring for 30 minutes at a temperature of 110 °C using a stirring hot plate, to ensure the solid precursors are complete dissolved and homogeneously mixed, and to remove water and oxygen. The dissolved Pt precursor with the PVP has a clear yellow colour, and the Rh precursor with the PVP has a brown- orange colour, as seen in Figure 14. The liganding solvent is then added to the solution and after 15 sec of stirring the beaker is wiped clean of oil on the outside and placed in a microwave oven operating at 900W. The total microwave irradiation (MIW) time is 10 min, in cycles of 30 sec 'on' followed by 5 sec 'off 'with stirring of the mixture using a stir plate. The stirring is included to prevent agglomeration of the particles. After the reaction a black colloidal solution is obtained. After cooling down, the nanocrystals are collected by flocculation the reaction mixture in ethanol and then separating them from the solvents using a high speed centrifuge. The particles are washed two times with ethanol and once with an ethanol-toluene mixture, before redispersion.

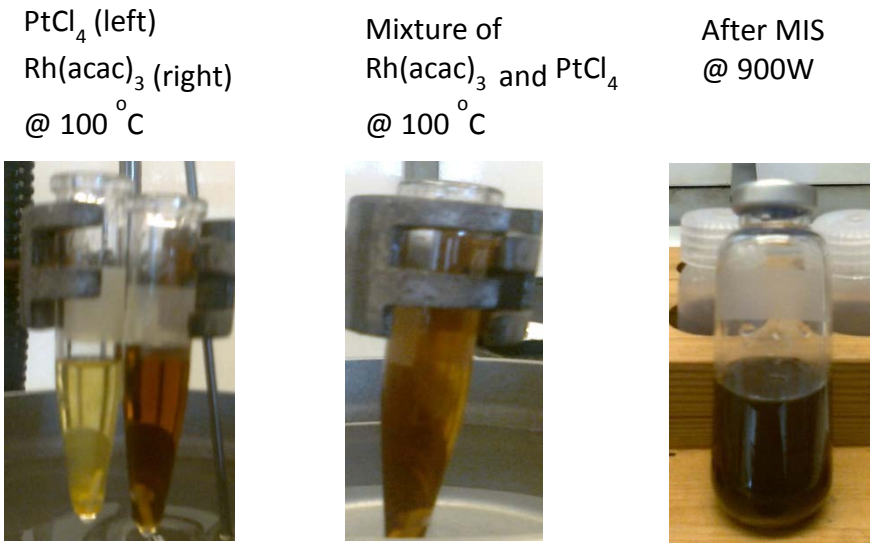


**Figure 14. Left; comparison of the dissolved Pt precursor and the dissolved Rh precursor. Middle; colour of a mixture of dissolved Pt and Rh precursors. Right; colour of a typical synthesised of nanoparticle using the microwave procedure.**

## 2.2Metal-on-support Catalysts

### 2.2.1 General Introduction

Catalysts are defined as any substance that affects a reaction without being consumed in the process. The main use has traditionally been to increase the reaction rate, but the focus has lately shifted to selectivity of the catalysts.[53] Selectivity of a catalyst means that when a reaction can have several reaction pathways and thereby different products, the catalyst makes one of the pathways more preferential, thereby "choosing" that end product.[7] Factors that affect the selectivity of a heterogeneous metal-on-support catalyst are pore size and distribution and surface area of the support, and composition and size of the metal.[8]

A metal-on-support catalyst is composed of two main components, the metallic nanoparticles and the support material. The support material acts as a carrier for the metallic nanoparticles, ideally keeping the particles separated and in a non-agglomerated form. The often high temperature used during catalysis can cause free nanoparticles to agglomerate, causing the surface area to be reduced.[23] The chemical composition and thermal pre-treatment of the carrier material is often found to affect the reactivity, stability as well as selectivity of the nanoparticles through electronic interactions between the support and the metal nanoparticles.[7]

Catalytic active metals include many of the transition metals, like Pt, Rh, Re, Fe, Ni and more, either used alone on the support or together [7, 16, 23, 53-55] Bimetallic catalysts often have one component that has the main desired function, and one component that acts as a promoter by either facilitating the main reaction more, or dealing with a side reaction.[56]

Support materials for metal on support catalysts includes silica ($SiO_2$), different types of aluminum oxides($Al_2O_3$) and titanium oxides ($TiO_2$), cerium oxides, zeolites, silicon carbides (SiC), anionic and cation clays, alkali earth oxides (M = alkali earth metal), rare earth oxides ($Ln_2O_3$; Ln = rare earth element) and carbon nanofibers.[8, 24] Oxide supports are also often categorized after their acid-base properties as this is a property that often influences the catalytic performance of the catalyst. Typically are $SiO_2$ and $TiO_2$ acidic supports, $Al_2O_3$ amphoteric and the alkali- and rare earth oxides basic.

The support material used in this thesis is alumina, $Al_2O_3$. For this reason a more detailed description of this material will be presented. Alumina exist is several modifications, γ-, δ-, θ-, η-, α-, κ- and χ- alumina, as shown in Figure 15. Several of them are high-surface area mesoporous oxides, commonly used in catalysis due to its high thermal stability and their contribution to activity and selectivity.[8, 24] Many of the different alumina modifications can be produced from boehmite, AlO(OH) (Figure 15). During heat treatment (calcination) any physically and chemically bound water is removed, and the oxide hydrate becomes an oxide, $Al_2O_3$, with different modifications depending on the temperature of the heat treatment.[57, 58]

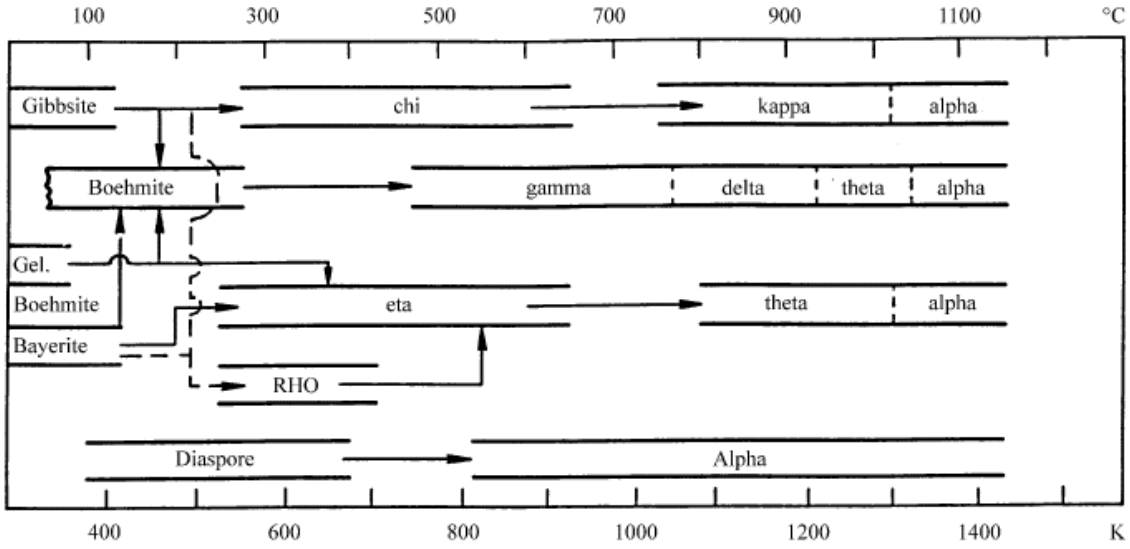


**Figure 15. Different modifications of aluminium oxide and the temperatures needed for their formation. [57]**

A comparison of the powder X-ray patterns of different $Al_2O_3$ phases is shown in Figure 16. Alpha alumina is the most crystalline modification of the different alumina modifications, and the gamma alumina has the largest surface area, with a factor 20 larger than the alpha alumina.[8, 12]

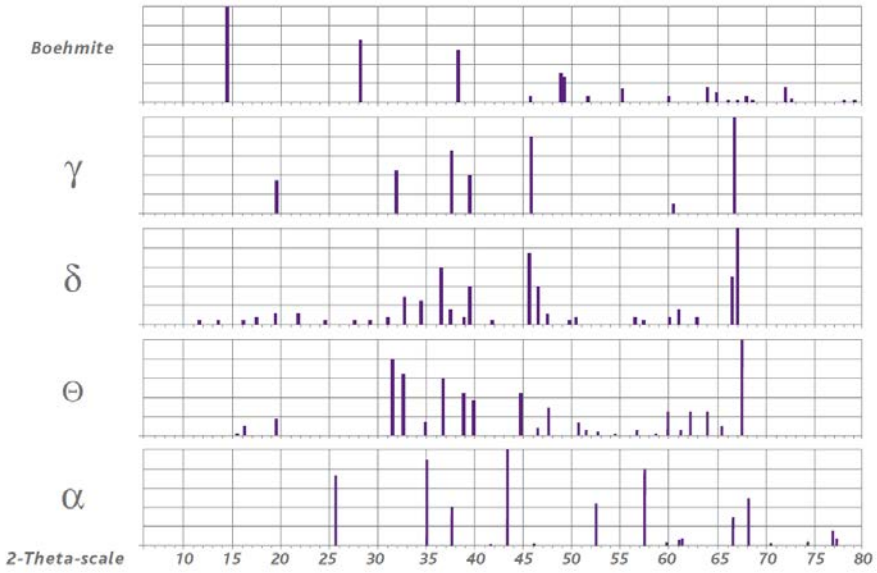


**Figure 16. Powder X-ray diffraction patterns of the different alumina phases[59]**

### 2.2.2 Preparation Methods for Metal-on-support Catalysts

The metallic nanoparticles can be deposited onto the support in a variety of ways, and is commonly done through deposition of free standing nanoparticles (section 2.2.2.1) or via the more classic wet-impregnation approach (section 2.2.2.2), as illustrated in Figure 17. In the following the principles behind the two approaches are described.

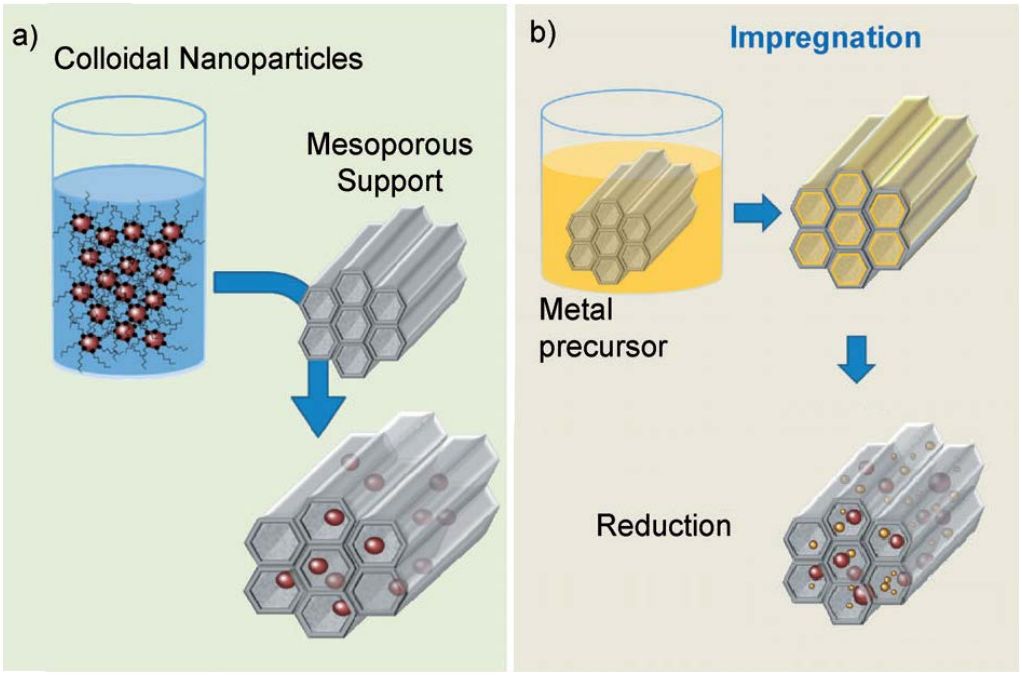


**Figure 17. Schematics showing a) Deposition of free standing nanoparticles onto a support. b) The wet impregnation technique to form metallic nanoparticles on a support. [24]**

### 2.2.3 Preparation of Metal-on-support Catalyst via Deposition of Free Standing Nanoparticles

Well defined metallic particles with respect to atomic arrangement, chemical composition, (monodisperse) particle size as well as morphology are of high importance in catalysis. When the nanoparticles are synthesised prior to the deposition onto the support, control of the mentioned parameters are possible. Figure 18 a) is a schematic flow diagram of the steps included in the method for preparation of a metal-on-support catalyst from free standing nanoparticles, and in the following some details in the procedure will be highlighted. In this work PtRh/Al2O3 metal-on-support catalyst were produced following this method.

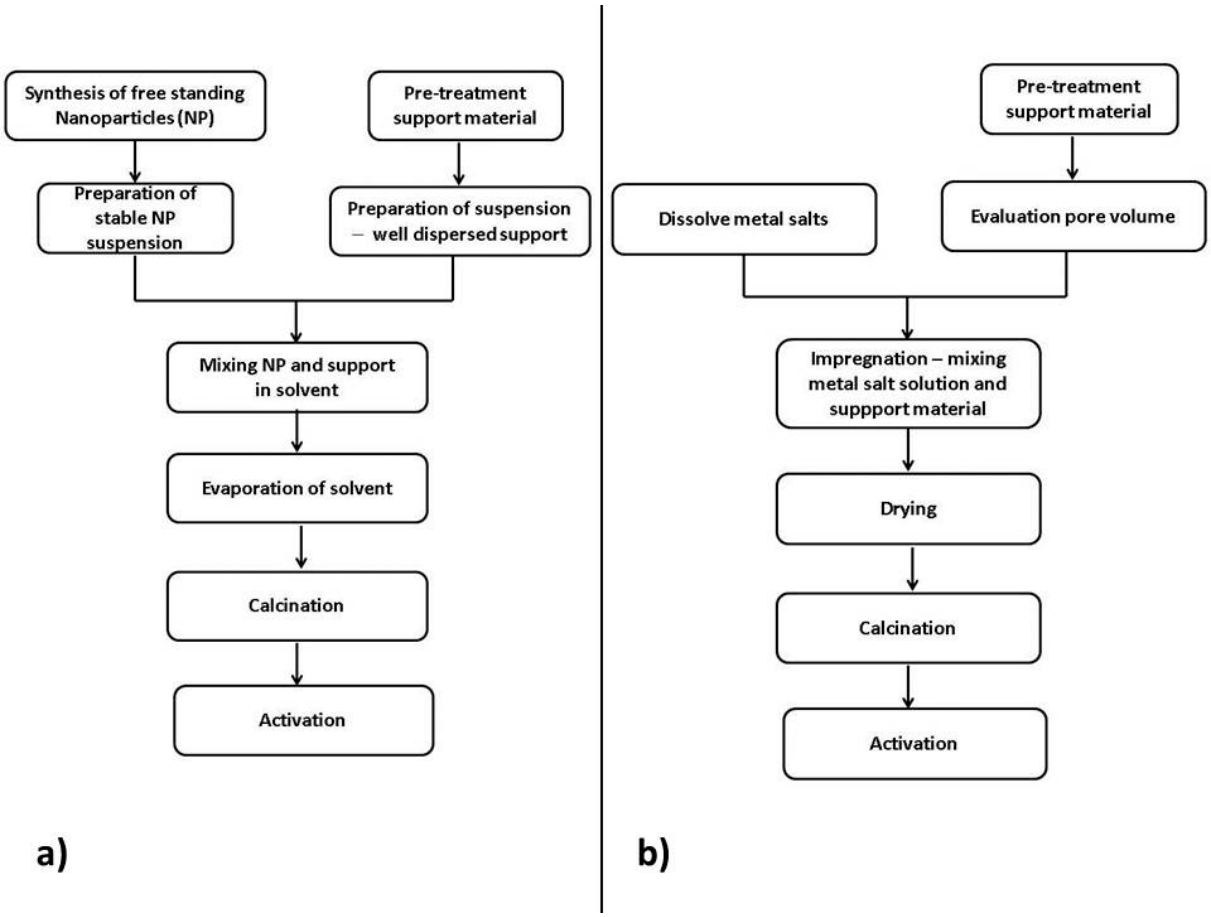


**Figure 18. Flow diagrams of the essential steps in the preparation of a metal-on-support catalyst by means of the a) deposition of free standing nanoparticles and b) by the incipient wetness impregnation route.**

Free standing $Pt_{1-x}Rh_x$ nanoparticles (NPs) are first synthesized and washed using either the 'round flask' or the 'microwave assisted' route (see sections 2.1.1 and 2.1.2), giving NPs with targeted metal composition, atomic arrangement and particle size. The free standing NPs are subsequently re-dispersed in a solvent giving a colloidal solution. In the present work typically (chloroform or toluene) were used, which boils at 61$^{o}$C and 111$^{o}$C, respectively. A colloidal metal particle solution will facilitate good dispersion of the metallic particles on the support in the deposition step. In parallel is the support material calcinated at targeted temperature to convert the boehmite to gamma-alumina with a surface area in the range 50-100 $m^2$/g. Alternatively, the boehmite is used as received from the supplier. The powdered $Al_2O_3$ support material is gently crushed and mixed with the same type of solvent as the NPs, and then sonicated. The sonication step is included to ensure that the alumina does not agglomerate, and to disperse the $Al_2O_3$ in the solution. The pre-synthesised metallic particle solution and the dispersed $Al_2O_3$ support solution is then mixed in a ratio that give a desired metal loading on the support (in this work we typically targeted for 2 wt.% metal). The mixture is kept under string conditions in a sealed container at ambient temperature for 48 hours. The purpose of this step is to allow the NPs to anchor and chemically attach to the alumina surface. Subsequently the solvent is slowly evaporated, maintaining the stirring conditions for as long as practical possible. The resulting powders where then calcinated at

elevated temperatures to burn of organic residues like the surfactant(s) and any remaining solvent, and to prepare the catalysts for conditions to be used during catalysis. A general rule is that the calcination temperature should exceed the temperature the catalyst later will be tested catalytic at. The reason for this is that both the support material and the metal nanoparticles will undergo modifications with respect to sintering etc. when exposed to elevated temperatures. This may affect the catalytic materials performance. As the metallic particles produced in this work are noble metals, the particles will not oxidize during the calcination process, so no subsequent activation step (i.e. $H_2$ reduction is required).

### 2.2.4 Preparation of Metal-on-support Catalyst via the Wet Impregnation Method

In the present work the wet impregnation method, or incipient wetness impregnation, was applied for preparation of Co-Re nanoparticles on alumina. A schematic flow diagram of the important steps for the applied method is presented in Figure 18b). In the following, the main steps in the procedure will be described.

In a typical synthesis the as-received alumina was heat treated to remove any physically adsorbed water. A water adsorption test was preformed to find the amount of water needed to fill the pores of the alumina. This was done by adding precalsined alumina to a large diameter beaker, adding water drop wise with frequent stirring and knocking of the beaker to the table in between to make sure water was filling all pores. Water was added until stirring mad mixture resemble wet snow (snowball snow), and the knocking of the beaker to the table resulted in the appearing a thin layer of water (the mixture was now resembling cake frosting), see Figure 19. The pores were then completely filled, and the amount of water added was noted. The amount of alumina to obtain a 20 wt.% loading was calculated, and recently heat treated alumina was measured out. The cobalt and rhenium precursors were completely dissolved in the amount of water estimated to fill the pores of the weighed out alumina. The solution was added to the alumina followed by stirring and knocking of the beaker to the table, this was repeated three times to ensure the solution was distributed well onto the alumina, and that the pores were filled. The mixture was placed in an oven with good air circulation at 110 °C for 3 to evaporate the water, with stirring every 15-30 minutes to ensure that all the powder was dried. During drying the powder went from pink to purple.

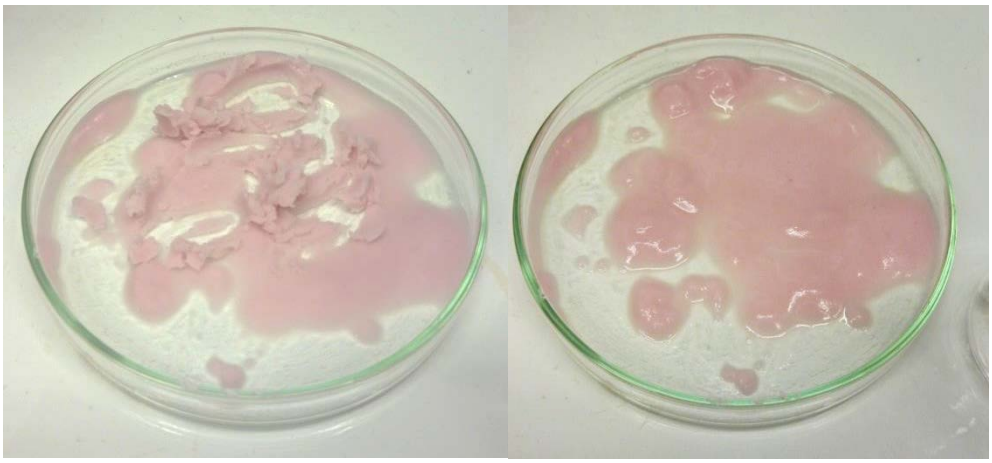

**Figure 19. Mixture of alumina and metal precursors. Right, after stirring of the mixture. Left panel, the same mixture after knocking the beaker to the table, producing a thin layer of water on top.**

The dried powder was then transferred to a quarts reactor and calcinated at 300 °C for 16 h. This was done in an air flow, with a rate of ~61mL/min. The colour change form before drying, after drying and after calcination is illustrated in Figure 16. During the calcinations, the cobalt precursor, in this case cobalt nitrate decomposes to $Co_3O_4$ with the production of nitric gases, which are highly corrosive.[55] For this reason the fumes were directed to the ventilation system in the fumehoods. The purple powder turned black/dark grey during calcination (see Figure 20). During calcination some of the $Co_3O_4$ reacts with the $Al_2O_3$ in the interface between the two, forming a spinel structure as $Co^{2+}Co^{3+}_{x}Al_{2-x}O_4$.[8]

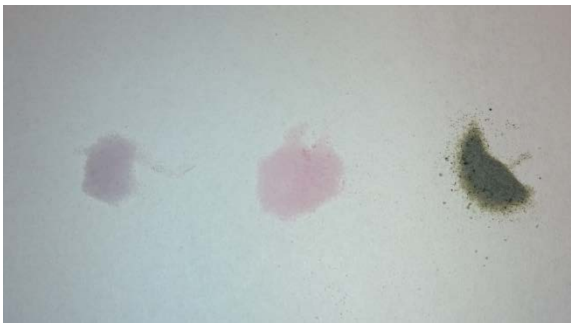

**Figure 20. The colours of samples after different steps in the impregnation method; left, after drying of the solvents; middle, before evaporation of the solvents; right, after calcination**

After calcination the powder was reduced at 350 °C for 16 hours in the quarts reactor, as described by equations XI and XII. For the reduction, a continuous flow of 4 % $H_2$ was used. To ensure that the reduced catalyst was not exposed to air, the whole reactor was sealed in the 4 % $H_2$ atmosphere, and transferred to a glove box with argon atmosphere, where the catalyst was stored. When the metal precursors are mixed with the alumina before reduction, they should form nanoparticles inside the pores and cavities of the alumina. Alumina functions as a so-called hard template, and its rigid walls and the growth of the nanoparticles are therefore confined to the pores when the precursors are reduced.[23]

$$Co_3O_4(s) + H_2(g) \rightarrow 3CoO(s) + H_2O(g) \qquad \text{(Eq. XI)}$$

$$3CoO(s) + 3H_2(g) \rightarrow 3Co(s) + 3H_2O(g) \qquad \text{(Eq. XII)}$$

During the impregnation of the particles, several factors affect the cobalt distribution, including temperature, the reducing agent, the pH of the solution and atmosphere during calcination. Both the cobalt(II) nitrate ($Co(NO_3)_2$) and the perrhenic ($HReO_4$) solution are acidic, and may therefore affect the formation of particles.[8]

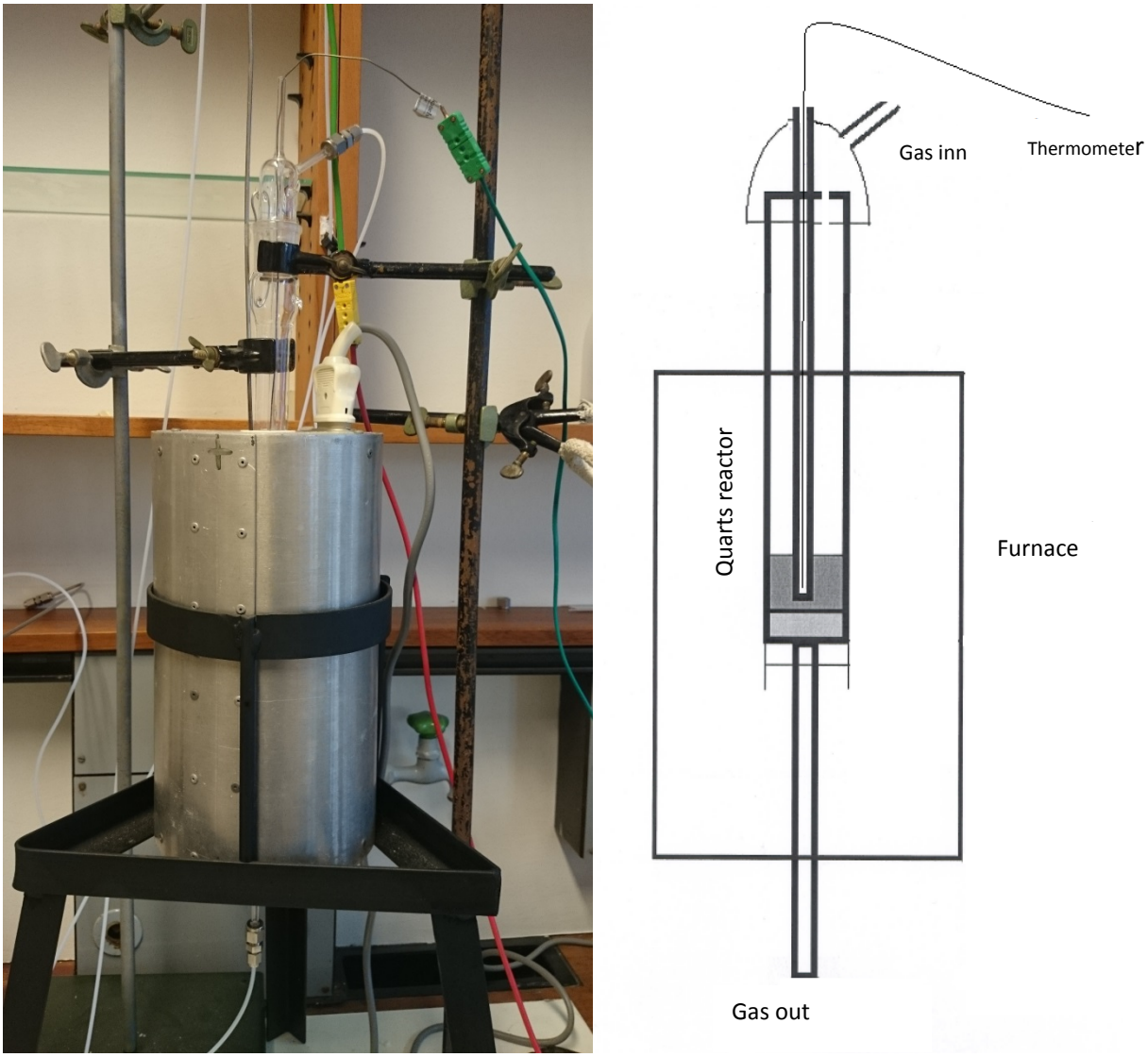


**Figure 21. The reactor for calcination and reduction of the Co-Re/Al2O3 catalysts. Left, picture of the setup. Right, illustration of the different components of the reactor – furnace system.**

## 2.3 Powder X-ray Diffraction

Powder X-ray diffraction patterns of all free standing particles and metal-on-support catalysts were recorded using diffractometers with Bragg-Brentano geometry or with a geometry very similar to the Bragg-Brentano geometry (only some few samples). In the Bragg-Brentano geometry, the X-ray source is mounted in a locked position, the sample is rotated at an angle θ around one axis, and the detector rotates at the same axis at an angle 2θ as shown in

Figure 22.

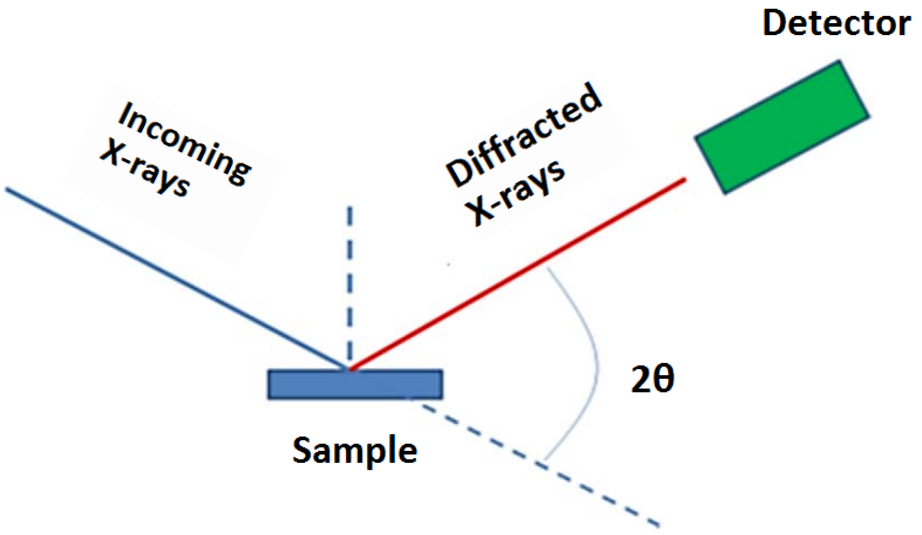


**Figure 22. Illustration of the Bragg-Brentano geometry.[60]**

The characteristic X-ray radiation used as the incoming X-rays, arises when a tungsten filament is bombarding an anode material (typically Cu, Mo, Co or Ag) with electrons, which results in emission of core shell electrons from the anode that is subsequently replaced by an electron falling down from the L or M shell to the K shell, sending out its excess energy in the form of X-rays at the same time. The characteristic X-rays that are produced from the L to K electron transitions are K$\alpha_1$and K$\alpha_2$, and the X-rays produced from the M to K transition are the K$\beta$. In order to obtain a monochromatic radiation, the K$\alpha_2$ and K$\beta$ are removed by a single crystal (typically Ge(111)) monochromator. In the case where a monochromator is applied, the powder diffraction pattern is collected using the monochromatic K$\alpha_1$beam, and measures the radiation diffracted from the crystalline materials. The most commonly used radiation is CuK$\alpha_1$. However, if the sample under investigation contain certain elements, e.g. cobalt, Mo radiation or Co radiation is more suited in order to supress fluorescence. Fluorescence occurs when an electron in the K shell of an element in the sample is knocked out by the incoming X-ray beam and replaced by an electron falling down from a higher shell. The excess energy of this electron is sent out as fluorescence, giving rise to low signal to noise ratio. This process can be avoided by changing the energy of the incoming X-ray beam, i.e. use another anode material.

The intensity of radiation scattered in the sample is measured as a function of the scattering angle θ, and from these angles, information about the spacing in between equal scattering planes is collected in a diffractogram. When the Bragg conditions are fulfilled for discreet angles, constructive interference will intensify the signal as illustrated in Figure 23 a and b, causing peaks in the diffractogram. The Bragg equation gives the geometrical relation between the crystal planes and the scattering angles;

$$n\lambda = 2dsin\theta \qquad \text{(Eq. XIII)}$$

Where;

$n$ = the order of reflection

$\lambda$ = wavelength of the radiation, for Cu K$\alpha_1$ this is 1.5406 Å, for Mo K$\alpha_1$ = 0.7093 Å

$d$ = spacing of the crystal lattice planes giving rise to the diffraction peak (Å)

$\theta$ = diffraction angle ($^o$)

The diffraction pattern collected in this work were used for; phase identification by looking at the position and intensity of diffracted peaks and comparing them to a database of the diffractograms of other well-known samples; to determine if the sample is phase pure by looking for the presence of peaks not belonging to the phase; to calculate the lattice parameters by the d-value of one of the peak positions (Eq XIV); and to estimate the particle sizes using the Scherrer equation (Eq. XVI) by measuring the width of the peak at its half maximum intensity (FWHM).

The spacing between the crystal lattice planes can be used to find the unit cell dimensions. E.g., both platinum and rhodium are described with cubic close packing, having a face centred cubic (fcc) lattice. The face centred cubic lattice has lattice points at the corners of a cubic box spanned by the lattice vector **a**, and at each face of this box as seen in Figure 23 c below. As the figure illustrates, these lattice points span planes in the crystals, which are the lattice planes diffracting the X-ray beam. The planes are described by the Miller indices *h, k* and *l*, which for a cubic crystal are related to the lattice vector by equation XIV. The indices are reciprocal of the unit cell, and notes how the plane cuts the edges of a unit cell. When the plane follows the face of the unit cell, as for the (100) plane, the plane is parallel to the **b** and **c** axis, e.g. never cuts the axis', and *k* and *l* is therefore noted as 0. In the notation *h* is 1 here, meaning that the plane cuts through the **a** axis only once per unit cell. The cubic face centred symmetry gives rice to destructive interference at some planes making only some of the planes present visible in the X-ray diffractogram. For a reflection to be allowed in the fcc lattice, the Miller indices must be all odd or all even, making the first peak visible in the diffractogram the (111) peak, the second the (200) and so on.

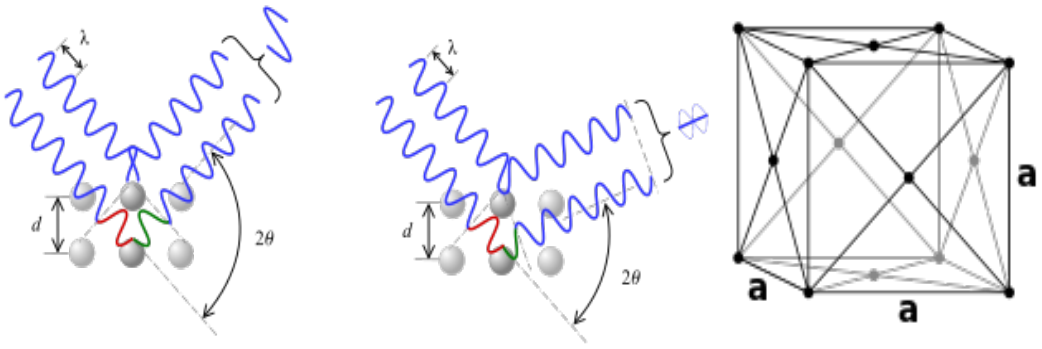


Figure 23, a) Illustration of the Bragg conditions being fulfilled, leading to amplified signals. b) Illustration of Bragg conditions not being fulfilled, leading to destructive interference of the signal. [3] c) The face centred cubic lattice (to describe cubic close packing).[5]

For a cubic crystal, the distance d relates to the lattice vector **a** by;

$$a = \sqrt{d \cdot (h^2 + k^2 + l^2)} \qquad \text{(Eq. XIV)}$$

Where the diffracting plane is spanned by *h*, *k* and *l*.[5, 61]

Vegard's law is an empirical rule that states that there will be a linear relation between the substitution grade and lattice parameters of an alloy of two metallic elements and the concentration of the constituent elements as shown in Eq. XV and Figure 24. It is assumed that the two elements have the same crystal structure. Although Vegard's law is almost never exactly obeyed, this can be used as an indication of the substitution grade of a binary solid solution composed of two elements crystallizing with the same crystal structure. Positive and negative deviation from the straight line plot often occurs, and for metals these deviations arises from repulsive and attractive atomic interaction, respectively.

$$x = \frac{a_3 - a_1}{a_2 - a_1} \qquad \text{(Eq. XV)}$$

$x$ = molar fraction of element 2

$a_1$ = lattice parameter of element 1

$a_2$ = lattice parameter of element 2

$a_3$ = lattice parameter of the solid solution composed of both elements 1 and 2.[5]

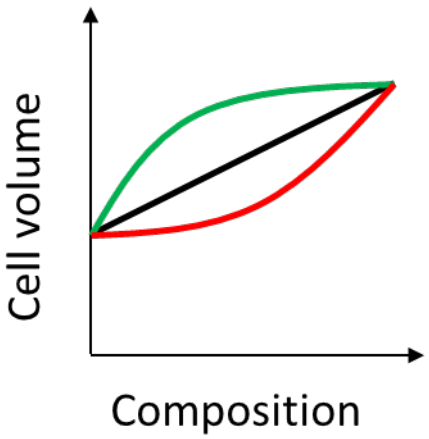


**Figure 24. Schematic illustration of the linear relationship of Vegard's law with positive (green line) and negative (red line) deviations marked.**

A method was established to determine the a-axis and the substitution grade of rhodium into platinum. For each sample two PXD-patterns were collected without moving the sample in between, one with a small step interval around the peaks of a NIST silicon standard that is mixed with the sample to get an accurate shape and peak position (described with a minimum of 7-8 points), and the other with a much larger step size but improved counting statistics from the nanoparticles. The silicon standard with well-known lattice parameters will give the same Si-diffraction pattern every time, and can therefore be used to correct for height errors in the diffractogram by comparing it to a database diffractogram. When producing a diffractogram, the $2\theta$ value is assigned with the assumption that the samples is at given position, and any height-deviation of this assumption will affect the path of the radiation, and give a slight shift of the measured $2\theta$ value. The position of the nanoparticle peaks, after shifting the powder diffractogram optimized according to the silicon peaks (during ex-situ analysis), can then be used to accurately determine the a-axis of the $Pt_{1-x}Rh_x$ nanoparticles. For the determinations in this work, the d-spacing at the maximum intensity of the peak was used to determine the a-axis. The alternative method with using the d-spacing from the middle of the peak gave a difference of 0.004 Å at most, and this value was used as a measurement of error in the method.

The width of the diffracted X-ray peaks in the obtained powder X-ray diffractograms relates to the crystallite size or particle size. Under the assumptions that inhomogeneous strain and compositional variations in the crystallites do not contribute to the peak broadening, the crystallite particle size can be determined from the width of the diffracted peak(s) after correcting for the broadening arising from the diffractometer. The broadening arising from the diffractometer itself depends on the instrument geometry and the alignment. The instrumental broadening can be determined experimentally by collecting the powder X-ray diffractogram of a reference material that do not have strain, compositional heterogeneities and a crystallite size of around 1 μm. In this work NIST silicon standard was used also to find the instrumental broadening by measuring the width of its peaks, since the silicon peak would be infinitely narrow if no instrumental broadening was present. The NIST silicon standard is a highly crystalline and pure reference material with particle size 4.9 μm.

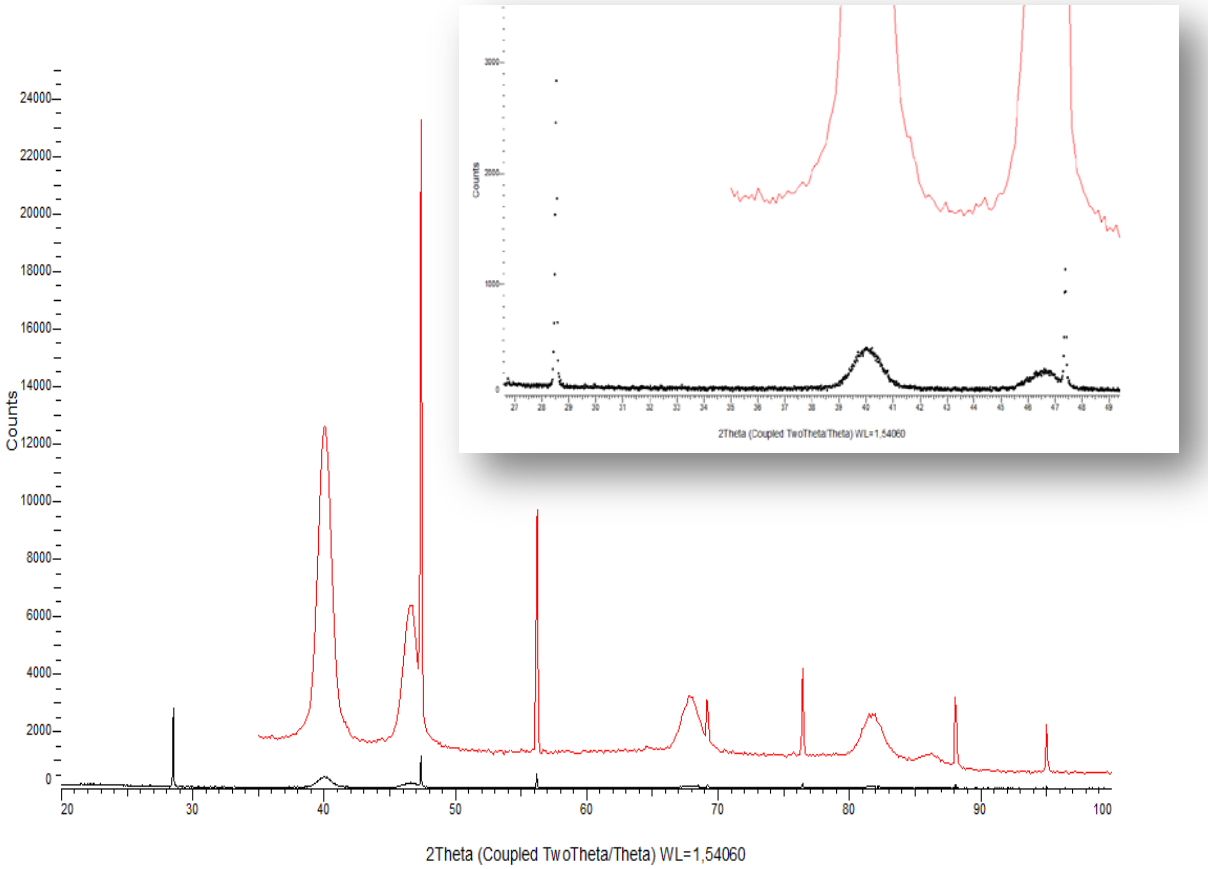


**Figure 25. A diffractogram collected with a small step interval around the NIST silicon peaks (black line), and with higher counting statistics around the nanoparticle peaks (red line). The inset shows the measured points around the NIST silicon peak, described with more than the minimum 7-8 points.**

The diameters of the nanoparticles were determined using the Scherrer equation (Eq. XVI);

$$\overline{D}_{XRD} = \frac{K\lambda}{\beta \cos\theta} \qquad \text{(Eq. XVI)}$$

$$\beta = \sqrt{B^2 - b^2} \qquad \text{(Eq. XVII)}$$

Where:

$\overline{D}_{XRD}$ = average particle diameter (nm)

$K$ = shape factor (here taken to be 0.89)

$B$ = Full with half maximum (FWHM) of the peak

$b$ = instrumental broadening factor.[8]

Through this method it is the average diameter of the particles that is estimated, however size and diameter is used interchangeably throughout the text.

For determination of the d in the diffractograms, the program function create area was used for all samples. This function choses the point on the peak with the highest intensity, rather than the middle point of the peak. For some samples the highest point of the peak also equalled the middle point of the peak, however, for others this was two very separate points. The insecurity of the method was therefore estimated by comparing the a-axis of the two methods on a sample where max and mid were very different.

## 2.4Dynamic Light Scattering

Dynamic light scattering was used to find how the particles behaved with respect to each other in solution, weather they were agglomerated or separated. The instrument measures Brownian motions of the particles in solution by sending a beam of monochromatic coherent light through the sample at different angles, and detects fluctuations of intensity as a function of time. These fluctuations are dependent on the speed of the particles, which again is dependent on the temperature, the viscosity of the dispersing fluid and the size of the particles or particle agglomerates. The fluctuations are interpreted using an autocorrelation function, which compares the signal to its self at given time intervals. The size of the particles and the size distribution are then extracted from the shape of correlation function. The Brownian motion is described by the translation diffusion coefficient, D, which relates to the hydrodynamic radii of the particles by the Stokes-Einstein equation, assuming spherical particles;

$$d(H) = \frac{kT}{3\eta\pi D} \qquad \text{(Eq. XVIII)}$$

Where

$d(H)$ = the hydrodynamic diameter of the particle (Å)

$k$ = the Boltzmann constant

$T$ = temperature in Kelvin

$\eta$ = the viscosity of the fluid

$D$ = translation diffusion coefficient ($Å^2$/s)

The instrument gives information about the mean size of the particles and the size distribution. Different sized particles/agglomerates will have different Brownian motion, and smaller sized particles, which have faster Brownian motion, will have faster fluctuation as illustrated in Figure 26. The hydrodynamic diameter measured by DLS is typically larger than the one determined by TEM or SEM due to the capping agent and the interaction between the capping agent and the solvent. [1, 62]

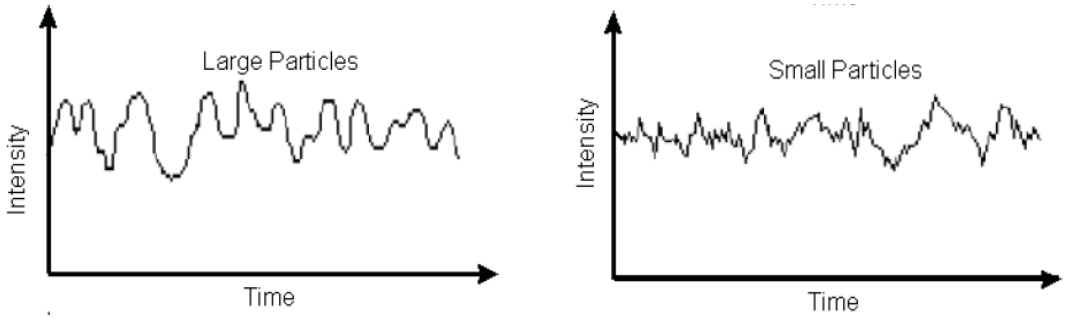


Figure 26. The intensity fluctuations arising from large (left) and small (right) particles. [1]

A vast dilution minimizes interactions between the particles in solution, ensuring free motion of the particles. Larger particles give more intense signals, so that the presence of some very large particles in the solution can dominate and mask the presence of smaller particles in the spectre, so good sample preparation is important for the use of this instrument. For this reason, samples should be to remove larger dust particles.

## 2.5Scanning Electron Microscope

The nanoparticles and metal-on-support catalysts synthesised in this work were investigated in a scanning electron microscope (SEM). The instrument has a column with an electron gun on top, followed by differ lenses and deflection coils that, in short terms, produces a narrow, well defined electron beam, as illustrated in Figure 28. Below the column in the specimen chamber sits the sample surrounded by different detectors, which for the SEM used in this thesis include; the energy dispersive x-ray spectrometer (EDS), the top -, upper -, lower – and scanning transmission electron microscopy (STEM) detector.

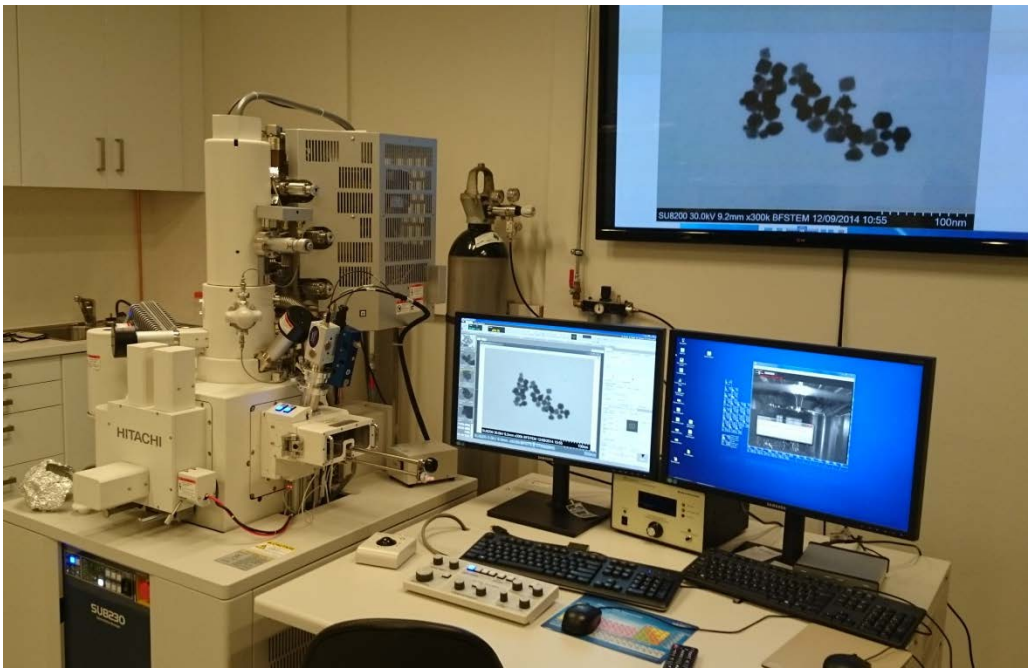


**Figure 27. Image of the SEM used for the thesis, with Pt nanoparticles synthesised as described in chapter 2.1.1. on the screens.**

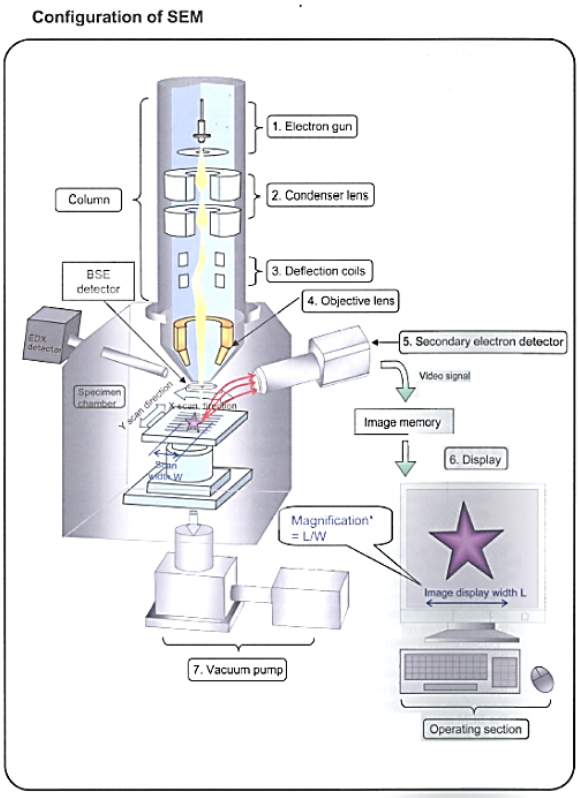


**Figure 28. The configuration of the scanning electron microscope [2]**

***Creating a SEM image***

The cold field emission gun (Cold FE gun) produces the electron beam by applying a high electric field to the emission tip at ambient temperature, which extracts the electrons. The gun tip is then a cathode, and the applied field acts like an anode. A second anode is placed just below, and accelerates the electrons to higher kV. The two anodes also act as a condensing lens by produces a crossover of the beam, defining the diameter of the beam. Several lenses and apertures in the microscope focus the beam to a narrow beam with a low energy spread. The resolution of the instrument is greatly affected by the diameter of the beam and energy spread which, for the cold FE gun, is 5 nm and 0.2 eV respectively. The well-focused beam gives a high resolution; the theoretical resolution of the microscope used for this thesis is 0.7 nm[63], where resolution is refers to the smallest distance that can be perceived as two separate points. An image is collected when the beam is scanned over the sample, detecting the signals arising as a function of time; each time corresponds to a specific x, y coordination, a so called pixel.[61, 64]

When the sample is irradiated by the electron beam, a number of different signals arise, and give rise to different images, as shown in Figure 31. The signals commonly analysed in the electron microscope are backscattered electrons, secondary electrons, X-rays and more recently, cathodoluminescence. A detector for the latter is not a part of the instrument in this thesis and is therefore not described.

***The different detectors; EDS, top, upper, lower and STEM***

The energy dispersive X-ray spectrometer (EDS) detects and analyse characteristic X-ray spectra as a function of energy, and plots it in a spectrum like the example shown in Figure 29. The detector consists of a solid state detector of a semiconductor and a multi-channel pulse height analyser, where each channel can detect energy spread of 5 eV. When characteristic X-rays generated in the sample hit the detector, an electron-hole pair is generated, and a bias voltage make the electrons move to the anode and the hole to the cathode, where they create an electron current pulse. The intensity of the X-rays is measured from the number of pulses, and the X-ray energy is measured from the height of the electrical current pulse[2]. Since the EDS detector does not have infinite resolution and the characteristic X-rays of different element may have the same energy, some peaks may overlap. However all atoms have several electron transitions, so each element present should give several peaks in the spectrum. The heavier elements will normally display the transitions from higher shells (L/M) in the interval we are looking at, while lighter elements will have K transitions. The characteristic X-rays are most effectively produced when the energy of the incident electron is approximately 2.5 times the binding energy of the electron.The obtained peaks in the EDS spectrum (Figure 29) created is analysed with respect to the intensity, and a composition of the measured area is estimated. However, the X-ray signals arise from a big volume (the excitation volume) of the sample, and EDS is therefore not a surface technique but rather a volume composition tool.

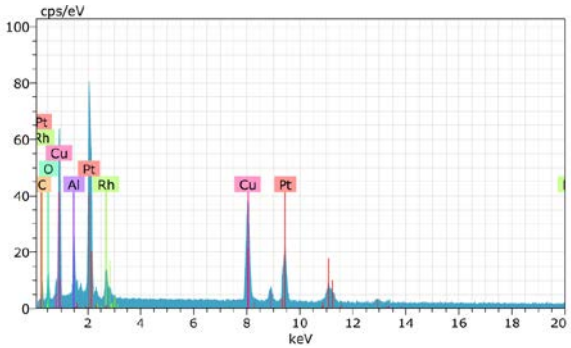


**Figure 29. An energy dispersive spectrum with the different elements corresponding to the peaks marked.**

The signals arising from electrons from the sample have different energies, and are divided into secondary or backscattered electrons, and their energy difference can be seen in Figure 30. Backscattered electrons give atomic number contrast, and arise when the incoming electrons are scattered back after interactions with the sample. The probability of the electrons being scattered back rises with the atomic number of the element detected because of stronger interactions with the electron. The secondary electrons arise when the energy lost from the incident electron is transferred to an atom, which ejects an electron, and this electron is then shot out into the vacuum. As seen in Figure 30 c), the energy of the ejected electron is low compared to the incident electron (elastically scattered electron), and one incident electron can give rise to several hundred secondary electrons. [61] Secondary electrons can also arise from interaction with the high energy back scattered electrons, and the secondary electron signal is usually strong. However since they have such low energies they have a shorter traveling distance, and the signal reaching the detector usually arise from no more than 10 nm into the sample. Because of the short traveling distance, secondary electrons give more surface topography contrast, where edges and peaks will give away more electrons than bulk

Secondary electrons may be detected by the lower and upper detectors, whiles back scattered electrons are detected by the upper- and top detector. The electrons hitting the common upper detector can be controlled by a signal varying mechanism, which uses an electromagnetic filter to decide where the electrons of different energy will go, this process is described in Figure 30 a and b.

The backscattered electrons are detected using the upper or top detector, where the top gives only compositional contrast and the upper give both compositional and topographical contrast as seen in Figure 31. The low angle backscattered electrons (LA-BSE) are the bottom blue lines in the figure, and also contain some topographical information from the sample. When the control electrode is set to a negative potential, these secondary electrons generated in the electrode by LA-BSE will hit the upper detector, giving a signal with both compositional and topographical contrast. The high angle backscattered electrons (HA-BSE) contain only compositional contrast (long blue lines) so the secondary electrons generated by the electrode they hit will make a flat, compositional image like the top left in Figure 31 b).

The secondary electrons are for most parts only detected using the upper detector and lower detector. When using the upper detector, Figure 30 a) demonstrates how only the secondary electrons from the sample are selected.

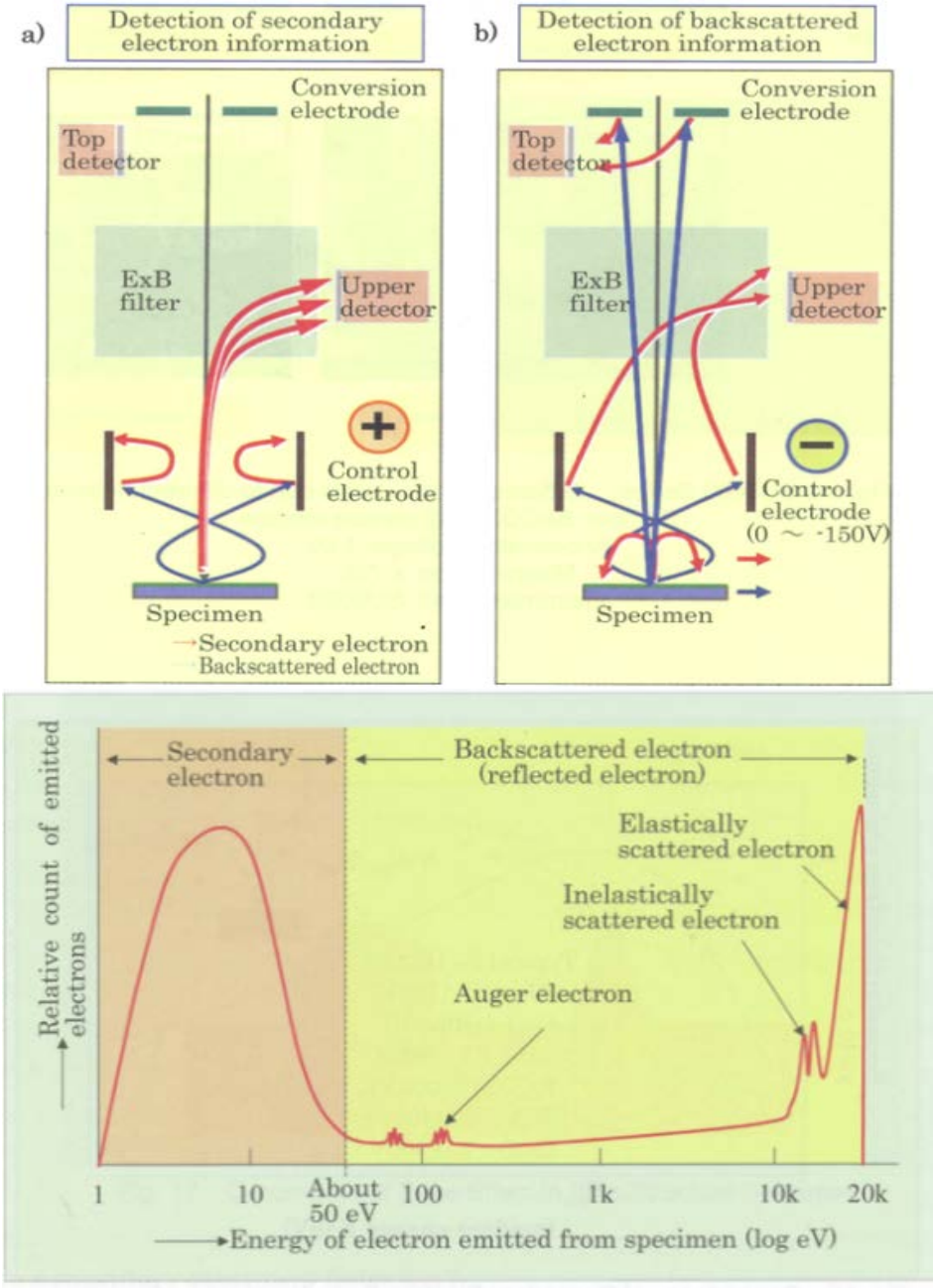


**Figure 30. a) The trajectory of secondary (red) and backscattered (blue) electrons when the control electrode is set to a positive potential. Notice that the backscattered electrons create secondary electrons when hitting the electrode. b) The trajectory of secondary (red) and backscattered (blue) electrons when the control electrode is set to a negative potential. c) The difference in energy of**

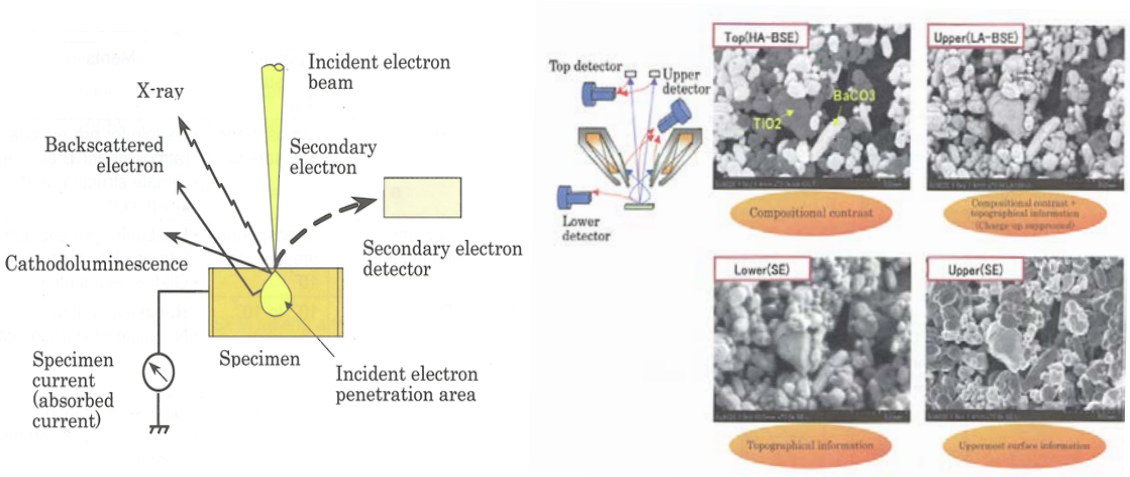


Figure 31. a) The different signals arising in the SEM. b) The detectors detecting the electron signals and the difference in the images they make. [2]

For thin samples, many of the electrons will travel straight through the sample, and there is therefore a detector below the sample for these electrons. The imaging technique is known as scanning transmission electron microscopy (STEM) which detects the electrons that have travelled through the sample. This detector quite simply detects the amount of electrons passing through the sample, giving shadows where there are particles, where thicker particles are seen as darker because they let less electrons pass through.

***Sample preparations***

SEM samples were prepared from the washed nanoparticle solutions by diluting the solution with 1:3 with more chloroform. A 3µL amount of such mixtures were drop cast and dried on continuous carbon film-deposited copper grids. The grid is then inserted into the sample chamber situated outside of the microscope chamber. The pure nanoparticles should cover some of the grid, but not be so concentrated that they form several layers. Some trial and error to find a suitable concentration was therefore necessary.

Samples containing a lot of carbon will contaminate the image by depositing a carbon layer on top of the sample. Before introducing the sample into the microscope chamber, plasma cleaning was used to remove some excess surfactant, solvent and surface carbon contamination, usually by one cycle of 1x 30 sec at 20 W. The plasma cleaner uses air as oxygen source, which reacts to ozone in the plasma. The ozone will oxidise hydrocarbons, and when vacuum is introduced the contaminants are flushed out. The sample is however not intruded directly under the beam of the plasma cleaner, as this would remove the entire carbon layer on the grids, taking the nanoparticles with them. The plasma cleaning was still effective when placed some distance away from the beam, and provided a much milder cleaning. Also, some practical reasons for the mechanical functions of the microscope made it beneficial to hold the sample some distance away from the beam. The setup of the plasma cleaner can be seen in Figure 32.

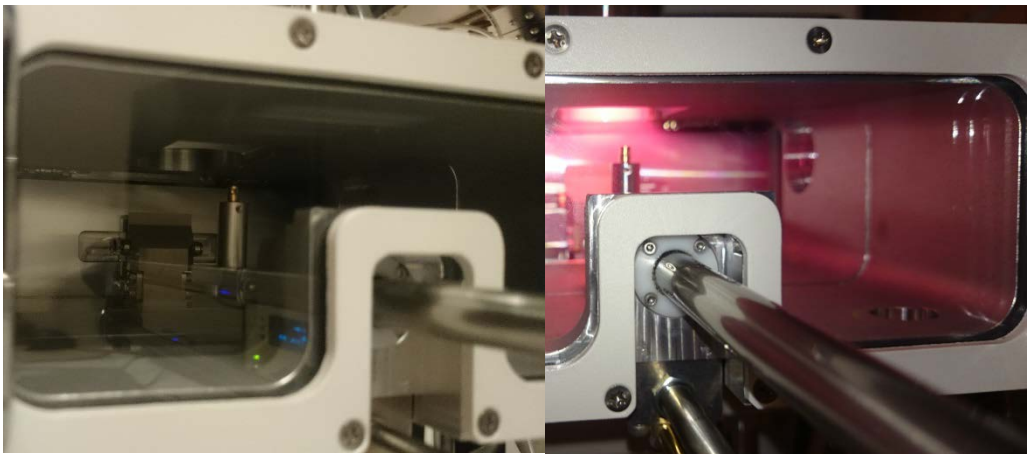

**Figure 32. Image of the plasma cleaner before cleaning (left) and during cleaning (right). Notice that sample is not placed directly under the beam but in front of the beam.**

## 2.6Single Point BET Measurements – 1. Brunauer, Emmet and Teller – Measurements

The surface area of solids can range from less than 1 m2/g to 2000-3000 m2/g, and the 1. BET-measurement is a technique used to determine surface area of porous powder materials.

The method is a simplified model of multilayer adsorption, based on a theory for monolayer adsorption known as the Langmuir theory. The measurement technique is based on gas adsorption to determine the total surface area, assuming that a monolayer adsorbent (typically $N_2$) is adsorbed by weak van der Waals forces. Amount of $N_2$ gas needed to cover the whole surface may then be measured. Some assumptions are made in the BET theory; that infinite layers of gas molecules will physically adsorb on a solid, that there is no interaction between each adsorbing layer, and that the Langmuir theory of monolayers can be applied to each layer.[65] A mulit-point BET measurement results in a BET plot which should be linear and have a finite intercept. However, a further simplification is done using the single point BET method where only one point is measured. The technique measures the equilibrium pressure and saturation pressure, and here the intercept of the BET plot is assumed to be zero, which can be done if the materials constant is much greater than 1. The volume of the gas needed to make a single monolayer is then estimated using equation XIX.

$$V_m = V_a\left(1 - \frac{P}{P_0}\right) \qquad \text{(Eq XIX)}$$

Where

$V_a$ = volume of gas adsorbed at standard temperature and pressure (STP)

$V_m$ = volume of gas adsorbed at STP to produce an apparent monolayer on the sample surface, in mL

$P$ = partial vapour pressure of adsorbate gas in equilibrium with the surface at 77.4 K (b.p. of liquid nitrogen), in Pa

$P_0$ = saturated pressure of adsorbate gas, in Pa

Before measuring, outgassing of the sample must be done to remove any physically adsorbed gasses and vapours.[66]

# 3. Experimental

In this chapter experimental details for the synthesis of free-standing $Pt_{1-x}Rh_x$ nanoparticles through the round-flask and microwave methods are presented firstly, followed by preparation of the Pt-Rh/$Al_2O_3$ and Co-Re/$Al_2O_3$ catalysts, and their characterisation.

## 3.1 Chemicals Used for the Experiments

Table 5 is an overview of all chemicals used in the experimental section presented, with general information about the chemicals. For each chemical, supplier, purity, molecular weight and chemical formula is given, as well as any short names used in the thesis. All chemicals were used as received from the supplier without any pre-treatments, and stored in a cool and dark place.

**Table 5. Overview of starting materials.**

| Chemical | Short name in thesis | Formula | Molecular weight (g/mol) | Purity | Supplier or manufacturer |
|---|---|---|---|---|---|
| **Rhodium(II) acetylacetonate** | $Rh(acac)_3$ | $C_{15}H_{21}O_6Rh$ | 400.23 | 97 % | Sigma-Aldrich |
| **Platnium(II) acetylacetonate** | $Pt(acac)_2$ | $C_{10}H_{14}O_4Pt$ | 393.29 | 97 % | Sigma-Aldrich |
| **Polyvinylpyrrolidone** | PVP | $(C_6H_9NO)$ [2] | 111.14 | not available[3] | Sigma-Aldrich |
| **Platinum(IV)Chloride** | $PtCl_4$ | $PtCl_4$ | 336.89 | ≥99.9 % | Sigma-Aldrich |
| **N,N-Dimethylformamide** | DMF | HCON(CH3)2 | 73.09 | 99.8 % | Sigma-Aldrich |
| **Oleylamine** | OAm | $C_{18}H_{37}N$ | 267.49 | 70 % | Sigma-Aldrich |
| **Acetone** | - | $C_3H_6O$ | 58.08 | HiPerSolv CHROMANORM | VWR |
| **Toluene** | - | $C_6H_5CH_3$ | 92.14 | 99.5 % | Merck |
| **Chloroform** | - | $CHCI_3$ | 11.38 | AnalaR NORMAPUR | VWR |
| **1,4-Butanediol** | Diol | $C_4H_{10}O_2$ | 90.12 | 99 % | Sigma-Aldrich |
| **Cobalt nitrate** | - | $Co(NO_3)_2 \cdot 6H_2O$ | 291.03 | 99 % | Sigma-Aldrich |
| **Perrhenic acid** | - | $HReO_4$ | 251.21 | 75-80 wt % in $H_2O$ | Sigma-Aldrich |
| **Boehmite** | - | AlO(OH) | not available | not available | SASOL Company |
| **γ-Alumina** | γ- $Al_2O_3$ | $Al_2O_3$ | not available | not available | Statoil |
| **Argon 5.0** | Ar | Ar | 39.95 | 99.999 % | AGA |
| **Hydrogen 4 %** | H2 | 4 % $H_2$ in Ar | not available | not available | AGA |
| **$H_2O$ type II** | - | $H_2O$ | not available | not available | Produced at department |

[2] Repeating unit 10.000

[3] Not available means here that the information is not reported by supplier

## 3.2The Platinum- Rhodium System

Platinum, rhodium and bimetallic platinum-rhodium nanoparticles were synthesised using the round-flask polyol method (3.2.1) and the microwave method (3.2.2). In some synthesis, the nanoparticles were deposited onto a support material. The unsupported nanoparticles were analysed using PXD and SEM, and the Rh nanoparticles were also analysed using DLS. The supported nanoparticles were analysed using PXD, TEM and 1. BET measurements. The synthesis details and preparation for analysis is elaborated in the following section.

### 3.2.1 The round-flask polyol Method

A series of different $Pt_{1-x}Rh_x$ samples were synthesized in this work. In Table 6 an overview of the exact synthesis conditions used for all samples presented. For the synthesis of nanoparticles with composition $Pt_{1-x}Rh_x$, PVP(2.0 mmol), $Rh(acac)_3$ and $Pt(acac)_2$ (a total of 0.2 mmol of the metal salts giving a 1 : 10 ratio of metal precursors : PVP) was added to a 3-neck round-flask, followed by addition of 20 mL diol. The round flask was heated to 150 °C for 15 min under stirring conditions (1500 rpm) in an argon flow (100 mL/min) before transferring the round flask to the hotter heating mantle. The synthesis batch was then allowed to react from 0.5-3 hours at the targeted reaction temperature (190-230 °C +/- 3 °C). The synthesis batch was then unwrapped from the quarts wool and aluminium foil, the heating mantle and heating plate was exchanged with a cold stirring plate, and the synthesis was left to cool in room temperature. The condenser was connected until the experiment had reached at least 50 °C.

After cooling the blackish colloidal suspension was washed by adding a 3 : 1 ratio of acetone to diol mixture, followed by separation of the nanoparticles by centrifugation. For this, a Beckman Coulter Allegra X-22R Centrifuge was used, operating at 5000 rpm for 5 minutes. The supernatant was replaced by new acetone followed by a new round of centrifugation, this was then repeated once. After the last round of centrifugation followed by disposal of the supernatant, 10 mL of chloroform was added, and the solution was transferred to a vial. The vial was sealed and shaken a bit.

Several routes for washing of the nanoparticles were tested to see if stable colloidal solutions could be made with the different conditions. Ethanol, acetone and 2-propanol were tested as flocculants, and chloroform, toluene and hexane was tested as dispersing media.

**Table 6. Overview of reaction conditions of all $Pt_{1-x}Rh_x$ syntheses carried out with the 'round flask' polyol method.**

| Composition | $Pt(acac)_2$ (mmol) | $Rh(acac)_3$ (mmol) | PVP (mmol) | Diol (mL) | Reaction temp. ($^oC$) | Reaction time (hours) |
|---|---|---|---|---|---|---|
| **Pt** | 0.2 | 0.0 | 2.0 | 20 | 190, 200, 210, 220, 230 | 2 |
| | 0.2 | 0.0 | 2.0 | 20 | 220 | 0.5, 1, 2, 3 |
| | | | | | | |
| **$Pt_{0.80}Rh_{0.20}$** | 0.16 | 0.04 | 2.0 | 20 | 220 | 2 |
| | | | | | | |
| **$Pt_{0.70}Rh_{0.30}$** | 0.14 | 0.06 | 2.0 | 20 | 220 | 2 |
| | | | | | | |
| **$Pt_{0.50}Rh_{0.50}$** | 0.1 | 0.1 | 0.1 | 20 | 190, 200, 210, 220, 230 | |
| | 0.1 | 0.1 | 2.0 | 20 | 220 | 0.5, 1, 2, 3 |
| | | | | | | |
| **$Pt_{0.20}Rh_{0.80}$** | 0.04 | 0.16 | 2.0 | 20 | 220 | 2 |
| | | | | | | |
| **Rh** | 0.0 | 0.2 | 2.0 | 20 | 190, 200, 210, 220, 230 | 2 |
| | 0.0 | 0.2 | 2.0 | 20 | 220 | 0.5, 1, 2, 3 |

### 3.2.2 The Microwave Method

The microwave synthesis progressed by mixing the following reagents in a beaker: 0.14 mmol $Rh(acac)_3$, 0.13 mmol $PtCl_4$, 0.1 mmol PVP and 2 mL DMF. The mixture was heated to 110 °C in an oil bath for 30 minutes under continuous stirring. Then 0.114 mol OAm was added during mixing and left to stir until it stopped fuming. The beaker was taken out of the oil bath and placed in the microwave for a total of 10 minutes, in 30 second intervals and stirring for 5 seconds in between. The microwave oven, a Kenwood CJW25, was operated at 900 W.

After synthesis the particles were left to cool in room temperature (> 1.5 hours) before washing. The washing was done using in 10 mL ethanol with centrifugation using a Beckman Coulter Allegra X-22R Centrifuge was operating at 5000 rpm for 5 minutes. The supernatant was replaced by new ethanol followed by a new round of centrifugation, this was then repeated once. After the last round of centrifugation followed by disposal of the supernatant the nanoparticles were redispersed in 10 mL toluene.

### 3.2.3 Preparation of 2 wt.% PtRh/Al2O3 Catalysts

In the present work, four different $Pt_{0.70}Rh_{0.30}/Al_2O_3$ catalysts were synthesized with a targeted $Pt_{0.70}Rh_{0.30}$ metal loading of 2 wt. %. In Table 7 is an overview of the four materials given together with synthesis parameters applied.

As-received boehmite was heated to 900 $°C$ for 10 hours in air with a ramp rate of $5°C/min$. After calcination the powder was stored in sealed containers for later use.

Solutions of free standing PtRh NPs were then prepared via either the round flask- or the microwave approach, see details 3.2.1 and 3.2.2, respectively, and one complete batch was divided in to where one half was deposited on 'boehmite' and the other half was deposited on γ-alumina.1 g calcinated or as-received boehmite was mixed 10 mL of the dispersive media used in the synthesis of the NP's (chloroform/toluene) by sonication for 1h. The colloidal PtRh nanoparticles were mixed with the support solution in a beaker using a stir bar, and left to stir for 2 days covered with an alumina foil. The following day the aluminium foil was removed and the solvent was evaporated. For nanoparticles dispersed in chloroform this was done at room temperature, and for the nanoparticles dispersed in toluene the evaporation was done at 40 $°C$. The remaining powder was transferred to an alumina crucible and calcinated at 900 $°C$ for 2 hours.
Samples for PXD and TEM were taken out before the addition of the alumina support and after every heating treatment. Further, calcinated Al2O3 samples were sent to SINTEF for 1. BET measurements.

**Table 7. Overview of applied conditions for preparation of the 2 wt. % $Pt_{0.70}Rh_{0.30}$/Al2O3 catalysts.**

| Short name | Applied conditions |
|---|---|
| **PtRh NP via the round flask polyol route** | |
| **Cat-PtRh-1** | NP synthesis conditions: 0.14 mmol $Pt(acac)_2$, 0.6 mmol $Rh(acac)_3$, 2.0 mmol PVP, 20 mL diol, reaction temperature 220 $^oC$, reaction time 2 hours<br>Number of parallel NP batches mixed per gram as-received boehmite: 3/2<br>Dispersing medium: Chloroform ; Deposition and evaporation time: 2 and 1 days<br>Final calcination conditions of as-synthesized catalyst: 2 hours in air |
| **Cat-PtRh-2** | NP synthesis conditions: 0.x mmol $Pt(acac)_2$, 0.x mmol $Rh(acac)_3$, 2.0 mmol PVP, 20 mL diol, reaction temperature 220 $^oC$, reaction time 2 hours<br>Number of parallel NP batches mixed per gram calcinated $Al_2O_3$: 3/2<br>Dispersing medium: Chloroform; Deposition and evaporation time: 2 and 1 days<br>Final calcination conditions of as-synthesized catalyst: 2 hours in air |
| **PtRh NPs via the microwave route** | |
| **Cat-PtRh-3** | NP synthesis conditions: 0.14 mmol $PtCl_4$, 0.13 mmol $Rh(acac)_3$, 2.0 mmol PVP, 20 mL diol,<br>Total number of microwave repetitions and MIW time; 20 rep. and 10 minutes.<br>Number of parallel NP batches mixed per gram as-received boehmite: 4/2<br>Dispersing medium: toluene; Deposition and evaporation time: 2 and 1 days<br>Final calcination conditions of as-synthesized catalyst: 2 hours in air |
| **Cat-PtRh-4** | NP synthesis conditions: 0.14 mmol $PtCl_4$, 0.13 mmol $Rh(acac)_3$, 2.0 mmol PVP, 20 mL<br>Total number of microwave repetitions and MIW time; 20 rep. and 10 minutes.<br>Number of parallel NP batches mixed per gram calcinated $Al_2O_3$: 4/2<br>Dispersing medium: toluene; Deposition and evaporation time: 2 and 1 days<br>Final calcination conditions of as-synthesized catalyst: 2 hours in air |

## 3.3Preparation of 20 wt. % CoRe/Al2O3 Catalysts

In this study 20 wt. % $Co_{1-x}Re_x/Al_2O_3$ catalysts with the following targeted cobalt – rhenium compositions Co, $Co_{0.95}Re_{0.05}$, $Co_{0.90}Re_{0.10}$, and $Co_{0.85}Re_{0.15}$ are prepared with the *incipient wetness* impregnation method. In Table 8 is an overview of the five materials given together with quantities of chemicals used.

**Table 8. Overview of applied quantity of chemicals used to synthesize 20 wt. % $Co_{1-x}Re_x/Al2O3$.**

| Formula | Short name | $Al_2O_3$ (g) | $H_2O$ (g) | $Co(NO_3)_2 \times 6H_2O$ (mmol) | $HReO_4$ (mmol) |
|---|---|---|---|---|---|
| **20 wt. % $Co/Al_2O_3$** | Cat-CoRe-0 | 5.0 | 6.66 | 1.70 | 0 |
| **20 wt. % $Co_{0.95}Re_{0.05}/Al_2O_3$** | Cat-CoRe-5 | 5.0 | 6.63 | 1.46 | 0.08 |
| **20 wt. % $Co_{0.90}Re_{0.10}/Al_2O_3$** | Cat-CoRe-10 | 5.0 | 6.62 | 1.26 | 0.14 |
| **20 wt. % $Co_{0.85}Re_{0.15}/Al_2O_3$** | Cat-CoRe-15 | 5.0 | 6.67 | 1.09 | 0.19 |

A portion of γ-alumina, slightly larger than the amount needed for synthesis, was calcinated for 10 h at 500 °C, directly before synthesis.

***Water Absorptivity Test***

The water absorptivity test gave that 13.55 g of $H_2O$ was absorbed by 10.0 g pre-dried γ-alumina.

***Synthesis of the Nanoparticles on Support***

The cobalt precursor was dissolved into the measured amount of type II water, and the liquid rhenium precursor added in the syntheses where rhenium occurred. The solution was mixed thoroughly, and added to the 5.0 g of pre-dried alumina, followed by extensive stirring. The beaker containing the mixture was inserted in an oven set to 110 °C, with air circulation. The mixture was taken out and stirred every 15 minutes the first hour, and every 30 minutes the following 2 hours. After drying, the powder was transferred to a reactor with air flow and temperature measurer, heated to 320°C with a ramp rate of 2.3 °C/min) and calcinated for 16 hours.

The powder was later calcinated at 392 °C (ramp rate 1.0 $°C$/min) for 16 hours under 4 % hydrogen flow. The reactor was sealed in the $H_2$ containing atmosphere and transferred to a glove box, where the powder was taken out and stored.

## 3.4 Characterisation

The characterisation techniques with instrument specifications and sample preparations used in the thesis are presented in this chapter.

### 3.4.1 Powder X-ray Diffraction

Powder X-ray diffraction patterns were recorded for all free standing nanoparticles and the PtRh metal-on-support catalysts using a Bruker D8 Discover diffractometer with Bragg-Brentano geometry and Cu K$\alpha_1$ X-ray radiation ($\lambda$ = 1.5406 Å), a single crystal (Ge(111)) monochromator, and a LynxEye detektor. The diffraction pattern covered a 2$\theta$ range of 35-100°, with a step length of 0.016°for the Si-NIST scan and 0.1°for the NP scan.

For the CoRe-catalysts, a Bruker D8 A25 instrument with a flipstick (no rotation of the sample) geometry and Mo $K_{\alpha1,2}$ X-ray radiation ($\lambda_{Ka1}$ = 0.7093 Å and $\lambda_{Ka2}$ = 0.7136 Å). The instrument uses focussing mirror optics and a LynxEye detector.

Three ways of preparing samples were used:

- For colloidal nanoparticles: A sample was taken out and left to evaporate the chloroform for a while to concentrate the solution. The samples were prepared for PXD by dripping the liquid sample of colloidal nanoparticles onto the sample holder, and mixing in a small amount of the silicon NIST.
- For powder samples (e.g. PtRh catalysts): The powders were crushed lightly, before adding some silicon NIST and ethanol and dripping the mixture onto the sample holder.
- For the reduced CoRe samples: The sample was prepared inside a glove box onto a UFO sample holder (sample holders with a lid to keep the atmosphere inert inside the holder). The procedure was otherwise as for other powder samples.

The diffraction patterns obtained were analysed using the software DIFFRAC$^{plus}$ EVA to determine phases present with comparison to the PDF (powder diffraction files) database, to determine the peak position and the FWHM of the peaks.

### 3.4.2 Scanning Electron Microscopy

The instrument used for all imaging and measurements was a HITACHI SU8230 Ultra High Resolution Cold FE-SEM. For most sample imaging, the scanning transmission electron microscopy (STEM) detector was used. SEM samples were prepared from the washed nanoparticle solutions by diluting the solution with chloroform. The amount of excess chloroform needed to obtain only one layer of nanoparticles on the grid varied with the sample, and the optimal dilution was determined through trial and error. A 3µL amount of the sample to be investigated was drop cast onto the carbon layer side of the grid, and left to dry on a lint free cloth. Carbon-coated cupper grids from Electron Microscopy Sciences were used for all samples.

### 3.4.3 Transmission Electron Microscopy

Transmission electron microscopy (TEM) images were acquired from a JEOL JEM-2100F microscope operating at 200 kV, equipped with a Gatan Orius SC 200D 2, 14-bit, 11-megapixel CCD and a spherical aberration corrector in the objective lens, to ensure a point resolution of 1.2 Å. An Oxford Inca energy-dispersive silicon-drift X-ray spectrometer (EDS), X-Max$^N$ 80 T, is provided for compositional analysis. TEM samples were prepared from the washed nanoparticle solutions, typically by taking out 1 mL sample and diluting it with 1:3 with more solvent. For the powder catalysts, a small amount was taken out and crushed lightly, before adding 1 mL of ethanol. A 3μL amount of the mixture was drop cast onto the carbon layer side of the grid, and left to dry on a lint free cloth. Carbon-coated copper grids from Electron Microscopy Sciences were used for all samples.

### 3.4.4 Dynamic Light Scattering

DLS measurements were performed on a Malvern Instruments Zetasizer-Nano ZS instrument with a 4nW He-Ne laser operating at a wavelength of 633 nm, and with avalanche photodiode (APD) detector recording at an angle of 173 °.

Rhodium nanoparticles (refractive index (n) = 2.14 in chloroform (n = 1.45 and), were analyzed at 20 °C in a quartz cuvette (PCS1115) and data were recorded from 6 data sets. The samples were filtrated by passing the sample trough 1.0 μm filters (Life Sciences, PTFE membrane) prior to the measurements. The filters were wetted before use by passing 2-3 mL of chloroform through the filter.

### 3.4.5 1.BET

Approximately 1 g sample of each of the calcinated PtRh/Al2O3 catalysts was sent to Sintef for 1. BET analysis. The samples were measured on the single point BET instrument Quantachrom´s Monosorb, using $N_2$ (g) as the adsorbing gas. The amount of adsorbed nitrogen was measured using a thermal detector. Before the measurement the sample was outgassed by heating to 150 °C for 1.5-2 hours with nitrogen flowing through the sample.

# 4. Results

In this chapter the experimental results obtained in this work will be presented and described. The experimental work is built up around two main parts:

i) Synthesis and characterization of free standing $Pt_{1-x}Rh_x$ nanoparticles
ii) Synthesis and characterization of 2 wt. % $Pt_{0.70}Rh_{0.30}/Al_2O_3$ and 20 wt. % $Co_{1-x}Re_x/Al_2O_3$ (x = 0, 5, 10 and 15).

Each of the two sub activities will be carefully described in the following chapters.

## 4.1 Synthesis and Characterization of Free Standing $Pt_{1-x}Rh_x$ Nanoparticles synthesized through the 'Round-flask' polyol method

The overall aim of this activity was to establish the 'polyol-route' as a method in the NAFUMA group with the purpose to synthesize well defined free standing nanoparticles. Included to this effort was the construction of a synthesis apparatus for the 'round flask' approach, which is described in section 2.1.1. Further, by means of the 'round flask' method, the purpose was to explore how average particle diameter and chemical composition of the particles are depending on the reaction time and reaction temperature.

In this section, the characterization of free standing nanoparticles using the 'round flask' polyol method is presented. All syntheses were carried out in an apparatus specially build for this activity, and results of the obtained particles are presented in form of unit cell dimensions (PXD), average particle size and particle size distribution (SEM, PXD), particle shapes (SEM) as well as stability of obtained solutions (DLS) .

### 4.1.1 Stability of Dispersed Nanoparticles

The last steps in the preparation of free standing nanoparticles are to wash the particles and to obtain a stable suspension of the particles, preferably a colloidal solution. Kinetically stable dispersions of the as-synthesized nanoparticles in non-polar solvents are desirable when producing well-dispersed metal-on-support catalysts. Our recipe for preparing the NPs is based on Park *et al*. [25] In this procedure is the particles washed and re-dispersed in acetone and chloroform, respectively. In this work we decided to evaluate different combinations of washing media - solvent for re-dispersion for selected $Pt_{1-x}Rh_x$ compositions (x = 0.25, 0.50, 0.75, 1.00). Table 9 is an overview of tested combinations of washing medium – solvent for re-dispersion listed together with a rating of how well the particles re-disperse after washing. In the work done by Park *et al*. [25] the nanoparticles were reported to be dispersed in the chloroform, but the stability of this solution is not commented.

For the nanoparticles of $Pt_{1-x}Rh_x$ where x = 0.75 and x = 1.00, the standard washing procedure with washing of the nanoparticles with acetone and re-dispersing them in chloroform encountered no problems. For Pt1-xRhx where x = 0.00, x = 0.25 and x = 0.50, re-dispersion

of the nanoparticles was often difficult, because the nanoparticles agglomerated and sedimented at the bottom. Several different solvents were therefore investigated for the separation (washing) and re-dispersion of the nanoparticles of $Pt_{1-x}Rh_x$ where x = 0.25 and x = 0.50, and a list of the solvents used is presented in Table 9. Acetone proved to be most effective in separating the particles, and chloroform re-dispersed the particles more than the solvents investigated. Acetone for washing followed by chloroform for re-dispersion was then used as a standard for the following experiments.

**Table 9. The different solvents used for washing and re-dispersion of nanoparticles with composition Pt1-xRhx where x= 0.0, x = 0.25 x = 0.5, x=0.80 and x=1.0**

| **Pt1-xRhx x** | **Solvent used for washing** | **Solvent used for re-dipersion** | **Degree of stable suspension** |
|---|---|---|---|
| 0.0 | Acetone | Chloroform | [1]Unacceptable |
| | Acetone | Ethanol | Unacceptable |
| 0.25 | Acetone | Chloroform | Unacceptable |
| | Ethanol | Particles did not flocculate | - |
| | 2-propanol | Particles did not flocculate | - |
| 0.50 | Acetone | Chloroform | Unacceptable |
| | Acetone | Hexane | Unacceptable |
| | acetone | Toluen | Unacceptable |
| | 2-propanol | Chloroform | Unacceptable |
| | 2-propanol | Hexane | Unacceptable |
| | 2-propanol | Toluen | Unacceptable |
| | ethanol | Particles did not flocculate | |
| 0.80 | Acetone | Chloroform | [2]Acceptable |
| 1.00 | Acetone | Chloroform | Acceptable |

[1]All particles were completely sedimented after a short time

[2]The solution remained black for long periods of time, with some immediate sedimentation. The sediments did not go into solution when shaking the container. See appendix A for illustrating image.

Visual inspection of the as-prepared rhodium nanoparticles dispersions in chloroform (x = 0.00) indicated an acceptable stability for all different reaction times and temperatures. The dispersion of rhodium nanoparticles synthesis with reaction time of 2h and reaction temperature of 220 °C in chloroform had the least amount of initial sedimentation. This sample was therefore chosen to be investigated further by means of dynamic light scattering (DLS) to extract information on the stability of this dispersion as well as the hydrodynamic radius of the as-prepared nanoparticles.

Three different concentrations of Rh NP dispersions were measured: (a) the as-prepared dispersion with an estimated concentration of 8.8 mg/mL, (b) a diluted dispersion with as-prepared sample - to - chloroform ratio of 1 : 1 (estimated concentration 4.4 mg/mL) and (c) an even more diluted dispersion with as-prepared sample – to - chloroform ratio of 1 : 2 (estimated concentration 2.9 mg/mL).

Before starting the DLS measurements, initial testing of the stability of the count rates were performed for approximately 5 min. The count rate displays the number of photons detected per second and provides a useful and fast evaluation of sample quality. During the 5 min that

the count rate profiles were monitored, it was observed a normal count rate display, indicating good quality samples for DLS measurements. No sharp spikes or wild fluctuation of the count rates were observed, indicating that dust is not present in the samples and that they were thermally equilibrated (respectively). In addition, the count rates were not found to increase or decrease with time, e.g no aggregation or sedimentation was taking place during the measuring time of 5 min.

Figure 33 presents the obtained correlation functions of the samples investigated, with concentration of (a) 8.8 mg/mL (as-prepared), (b) 4.4 mg/mL and (c) 2.9 mg/mL, from six (6) replicate measurements per sample. The amplitude of the G1 correlation function(s) at time 0 is found to be close to 0.9 for all samples, indicating good quality signals for analysis. In addition the decay of the correlation function(s) was found to be relatively slow for all three sample concentrations. The decay is related to the particle size, indicating larger (than expected) particles being measured. From initial inspection of the correlation data there seems to be a consistency throughout the measurements for the 6 replicate measurements.

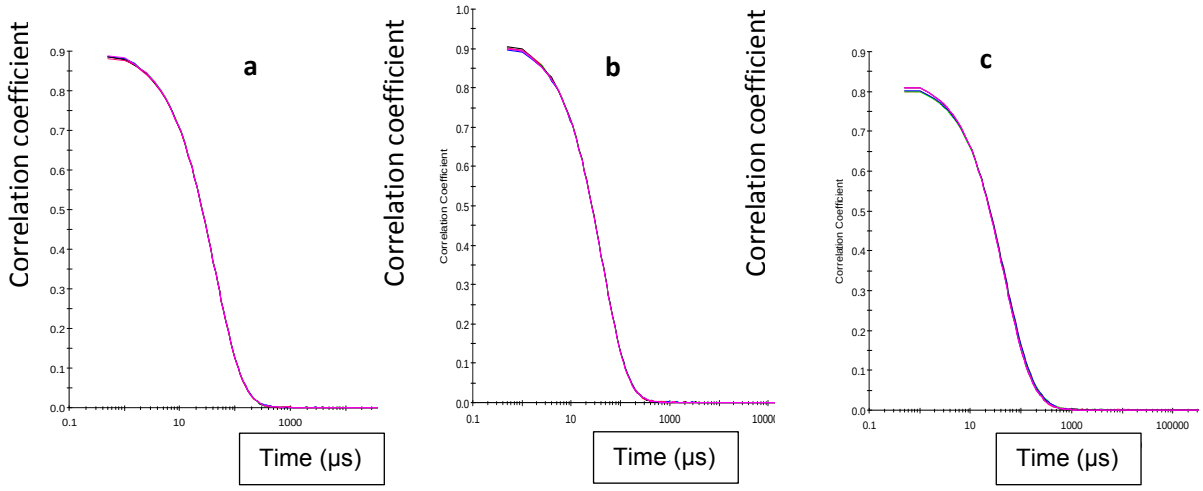


**Figure 33. Correlation functions of the samples under investigation with concentration of (a) 8.8 mg/mL (as-prepared), (b) 4.4 mg/mL and (c) 2.9 mg/mL, from six (6) replicate measurements per sample.**

The correlation functions were then used to calculate the size distributions of the samples under investigation. Figure 34 presents the size distributions by intensity of the samples with concentrations (a) 8.8 mg/mL (as-prepared), (b) 4.4 mg/mL and (c) 2.9 mg/mL, as produced by the Zetasizer software, wherein a general purpose analysis model algorithm has been applied to extract the decay rates for a number of size classes.

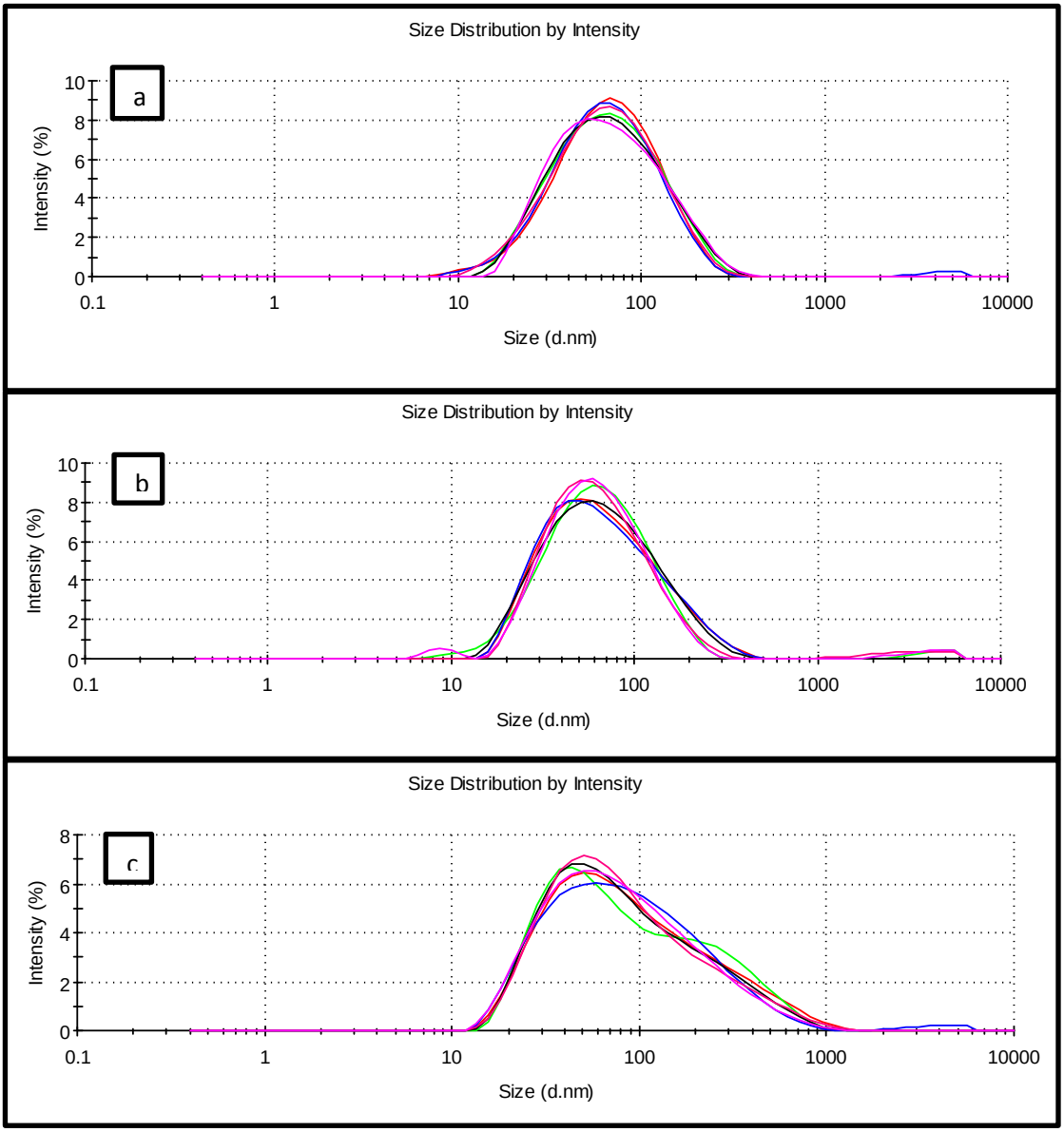


**Figure 34. Size distributions by intensity of the samples under investigation with concentration of (a) 8.8 mg/mL (as-prepared), (b) 4.4 mg/mL and (c) 2.9mg/mL, from six (6) replicate measurements per sample.**

By inspecting the obtained size distribution plots by intensity in Figure 34, a broad distribution is observed for all three suspensions. Such a broad feature could be either attributed to the presence of a rather polydisperse sample or to agglomerated nanoparticles. For such broad size distributions, neither the cumulant fit analysis (Z-average), nor the polydispersity index (PDI) values are of any use.

In Table 10 the mean hydrodynamic diameters and their standard deviations are given, as obtained from the intensity size distribution reports.

**Table 10. Mean hydrodynamic diameter and the standard deviation obtained from the intensity size distribution reports, for samples with concentration 8.8 mg/mL, 4.4 mg/mL and 2.9 mg/mL**

| Sample Concentration (mg/mL) | Mean size (nm) | Standard deviation (nm) | RCI % |
|---|---|---|---|
| 8.8 | 77 | 2 | 3 |
| 4.4 | 76 | 4 | 6 |
| 2.9 | 125 | 8 | 6 |

The as reported mean hydrodynamic diameter of the sample under investigation is found to be an order of magnitude bigger that the reported mean diameter from STEM analysis (8 ± 3 nm). Such difference could only be caused by the presence of agglomerates of nanoparticles in the dispersions under investigation.

The mean hydrodynamic diameter is found to be invariant for the sample with concentration 8.8 mg/mL and for the sample with concentration 4.4 mg/mL. However, for the sample with concentration 2.9 mg/mL, a significant increase of the hydrodynamic diameter is observed, an indication that further agglomeration takes place.

In Figure 34 (a) and (b), a tail in the small diameter region is observed, indicating the presence of smaller free-standing nanoparticles with an approximate hydrodynamic diameter of 10 nm. of The masking in the intensity plots of the free-standing nanoparticles is due to the much stronger scattering from the large agglomerates than the smaller particles. The implication of this observation is that it can be concluded that both free-standing and agglomerated particles are present in the solution.

These finding showed that the suspensions under investigation are not very stable; therefore no further testing with DLS was performed.

### 4.1.2 Effect of Reaction Time on Nanoparticle Size

For $Pt_{1-x}Rh_x$, the effect of reaction time (0.5 h, 1 h, 2 h and 3 h) on the nanoparticle size was investigated for the three compositions x = 0.00, x = 0.50 and x = 1.00. Other synthesis parameters as reaction temperature (220 °C), metal salt precursor: surfactant ratio (1:10) and concentrations (20 mL solvent) were kept constant. In Figure 35[4] (x = 0.00), 42 (x = 0.50) and 49 (x = 1.00) are the obtained powder X-ray diffractograms (PXD) of the synthesized particles presented. The PXD patterns show that all samples are phase pure, and the reflections can be indexed on a fcc type structure. The first reflection, (111) assigned to the $Pt_{1-x}Rh_x$ nanoparticles, in each diffractogram has the highest intensity and does not overlap with the Si-standard peak. For this reason the (111) peak was chosen to estimate crystallite size for each sample, with basis in the Scherrer equation. This peak was also used to determine the d-spacing and, through Eq XIV, the lattice parameters. The estimated lattice parameters are reported in Figure 36 (x = 0.00), Figure 43 (x = 0.50) and Figure 50 (x = 1.00), and the estimated particle sizes are reported in Figure 37 (x = 0.00), Figure 44 (x = 0.50) and Figure 51( (x = 1.00). Correspondingly, for each of the three compositions, produced at each of the indicated reaction times, SEM images were collected in BFSTM mode and the average particle size and particle size distribution was estimated from 200 nanoparticles. The SEM images and the corresponding histograms of the particle size distributions are reported in Figure 38-41, (x = 0.00), Figure 45-48 (x = 0.50) and Figure 52-55 (1.00).

In the following, the effect of reaction time for the three compositions Pt, $Pt_{0.50}Rh_{0.50}$ and Rh are described in more detail.

***Platinum (Pt) Nanoparticles:***

For Pt1-xRhx, x = 0.00, the PXD patterns for the reaction times 0.5 h, 1 h, 2 h and 3h are reported in Figure 35. The different reflections are marked with the corresponding (hkl) values of the fcc structure of Pt, and the reflections belonging to the Si-reference is marked with '*'. In the inset is an enlargement of the (111) peak. With basis in the (111) peak for each of the four samples, the a-axis was extracted as outline in section 2.3. In Figure 36 is the a-axis for each of the four samples plotted. Within the uncertainty of the method, the a-axis is concluded to be similar for the four syntheses. Further, the obtained a-axes are in line with reported values for bulk Pt, but slightly smaller than what is reported for Pt NP, see Table 3 and Table 2 in section 1.3.

By inspecting the powder X-ray patterns in Figure 1 more carefully; it can also be notices that the two syntheses with the shorter reaction time (0.5 h and 1 h) have slightly broader peaks than the peaks of the longer reaction time (2 h and 3 h). The sizes estimated from the (111) peak in the PXD pattern of the platinum nanoparticles for the different reaction times are found in Figure 37. The sizes were found to increase with increasing reaction time, with D = ~11-15 nm.

[4] The numberings in the figures refers to the detailed description of the Pt, $Pt_{0.5}Rh_{0.5}$ and Rh particles in separate sections.

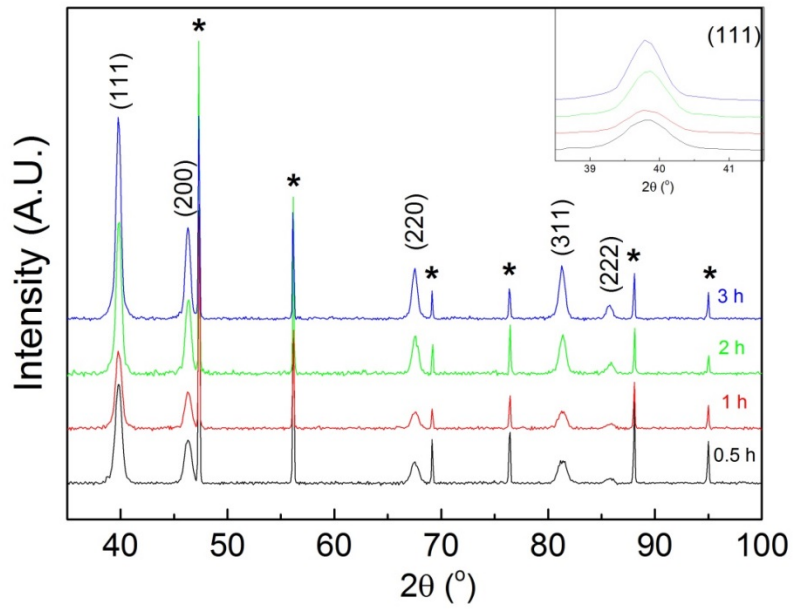


**Figure 35. PXD patterns of platinum nanoparticles synthesized with different reaction time, 0.5 h, 1 h, 2 h and 3 h.**

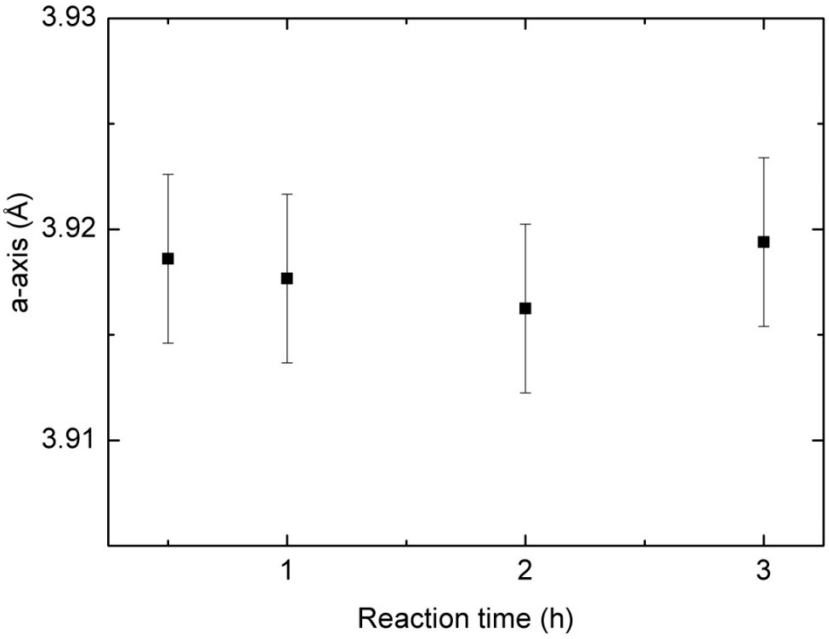


**Figure 36. The effect of reaction time (h) on the a-axis (Å) of the Pt NP's.**

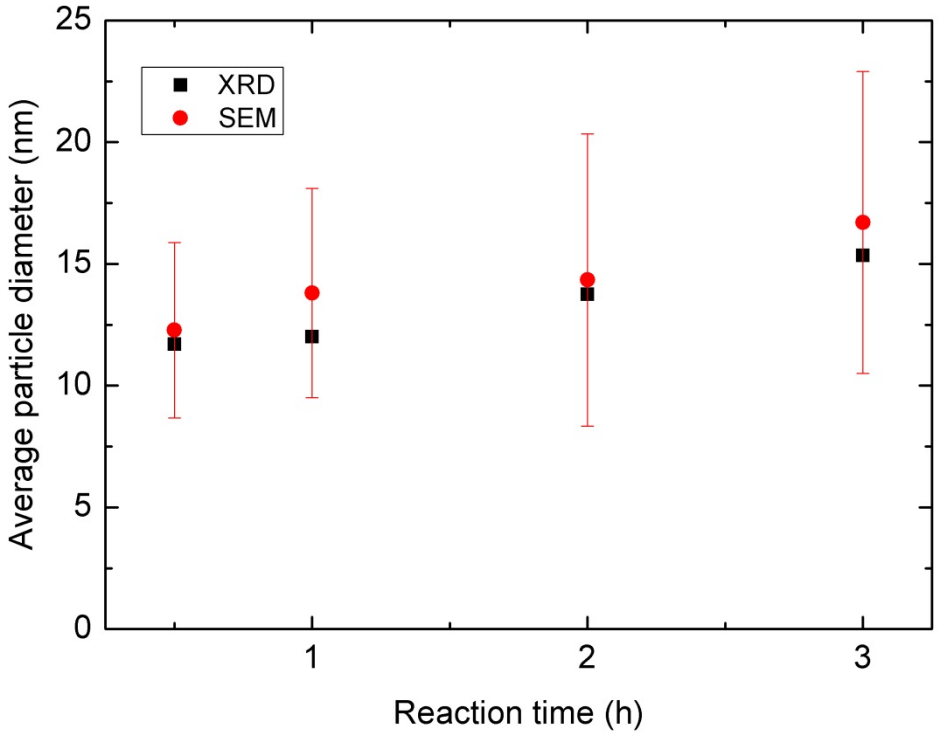


**Figure 37. Comparison of the average particle size estimate given by PXD (based on FWHM of the (111) peak) and SEM imaging for the different reaction times of Pt.**

The sizes of the nanoparticles found through SEM measurements of the platinum nanoparticles is presented in the histograms in Figures 38-41 (left) for reaction temperature 0.5h-3h. The histograms show a double size distribution. A corresponding SEM image from the same synthesis is also demonstrated in the figures (right), showing nanoparticles of different shapes and sizes in small agglomerates.

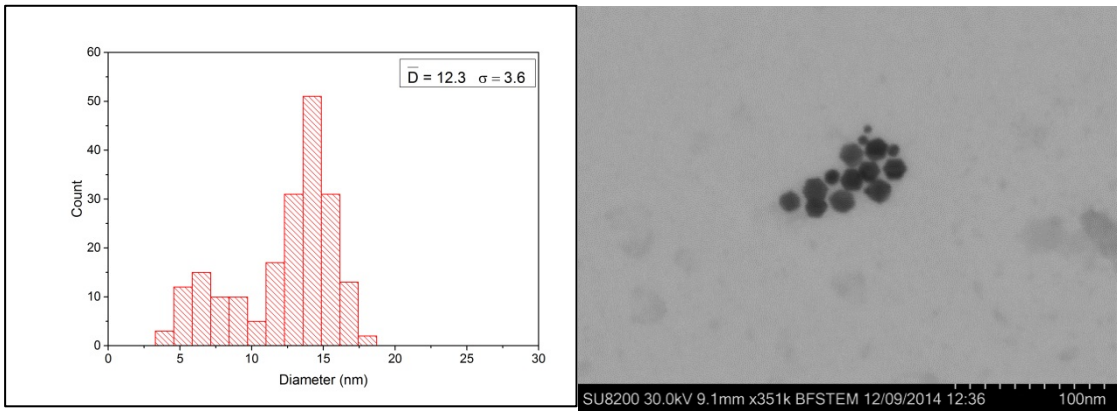


**Figure 38. The 0.5 h synthesis of Pt (x = 0.00) NP's. Left; Histogram showing size distribution of 200 measured nanoparticles, where a double size distribution is visible. Average size ($\overline{D}$) and standard deviation (σ) is stated. Right; SEM image in BFSTM mode, showing large, medium and small particles.**

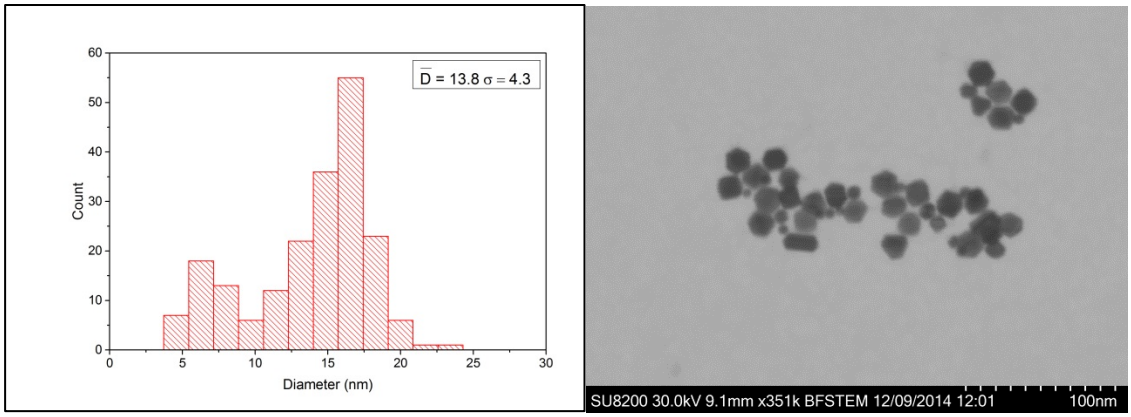


**Figure 39. The 1 h synthesis of Pt NP's. Left; Histogram showing size distribution of 200 measured nanoparticles, where a double size distribution is visible. Average size ($\overline{D}$) and standard deviation (σ) is stated. Right; SEM image in BFSTM mode, showing large, medium and small particles.**

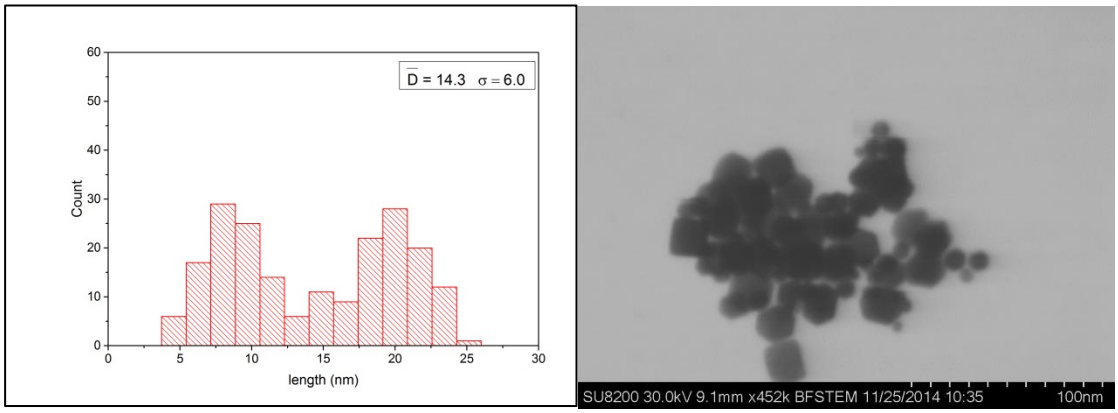


**Figure 40. The 2 h synthesis of Pt NP's. Left; Histogram showing size distribution of 200 measured nanoparticles, with a double size distribution. Average size ($\overline{D}$) and standard deviation (σ) is stated. Right; SEM image in BFSTM mode, showing large, medium and small particles.**

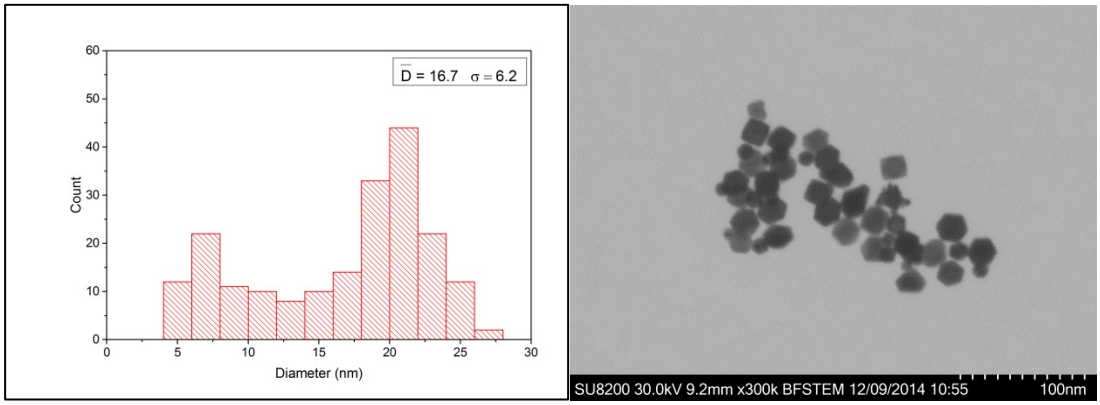


**Figure 41. The 3 hour synthesis of Pt NP's. Left; Histogram showing size distribution of 200 measured nanoparticles, with a double size distribution visible. Average size ($\overline{D}$) and standard deviation (σ) is stated. Right; SEM image in BFSTM mode, showing large, medium and small particles.**

The average particle size ($\bar{D}$), extracted from the SEM images was found to increase with increasing reaction time, and the average particle size and it's corresponding standard deviation ($\sigma$) is presented graphically in Figure 37. The broad size distribution is the reason for the large standard deviation given in Figure 37.

***Platinum-Rhodium ($Pt_{0.50}Rh_{0.50}$) Bimetallic Nanoparticles***

For Pt1-xRhx, x = 0.50, the PXD patterns for the reaction times 0.5 h, 1 h, 2 h and 3 h are presented in Figure 42. The different reflections belonging to the Pt-Rh nanoparticles are marked with the Miller indexes according to a fcc type structure, and the reflections belonging to the Si-reference phase is marked with '*'. No extra diffraction peaks were observed in the diffractograms, indicating that the synthesized $Pt_{0.50}Rh_{0.50}$ samples are phase pure. In the inset an enlargement of the (111) peak of the Pt-Rh phase included. With basis in the (111) peak, the a-axis of the four samples are extracted and the obtained values are reported in Figure 43. From Figure 43, it can be observed that the a-axis is increasing linearly from a = 3.832Å (0.5 h) to a = 3.846 Å (2 h) before it is flattening out at 3 h giving a = 3.847 Å. The reported unit cell dimensions must be concluded to be different, as an observed expansion of 0.015 Å is beyond the uncertainty of the applied method. Presently no exact explanation for the observation can be reported. In the Discussion section some thoughts around this observation will be given. The value is lower than reported in literature (see Table 2)

The average particle sizes of the four $Pt_{0.50}Rh_{0.50}$ samples were estimated with basis in the FWHM of the (111) diffraction peaks presented in Figure 43. The obtained results are reported in Figure 44. The results show minor variations, with D = ~5 nm at 0.5 hour reaction time and 6 nm at ~3 h reaction time.

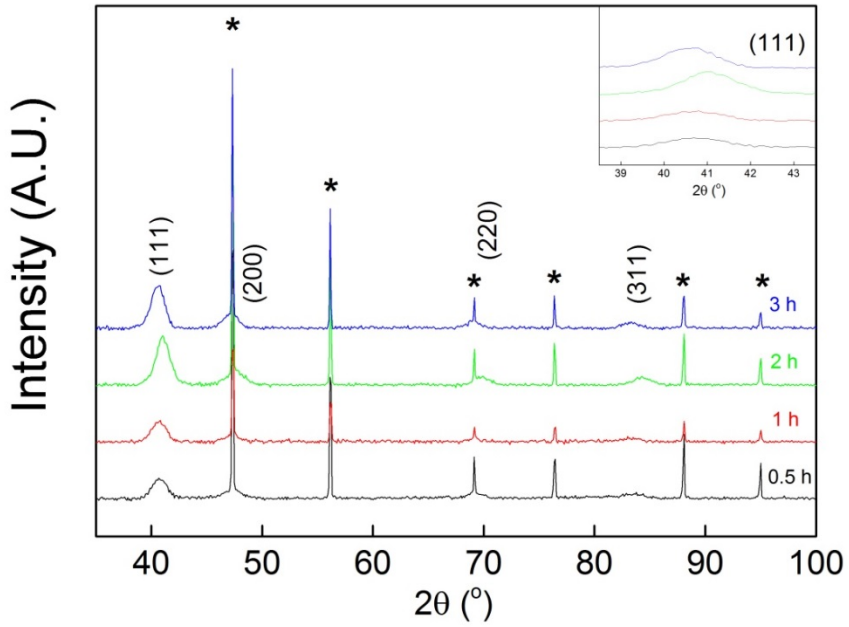


**Figure 42. PXD patterns of $Pt_{0.50}Rh_{0.50}$, synthesized with reaction times of 0.5 h, 1 h, 2 h and 3h.**

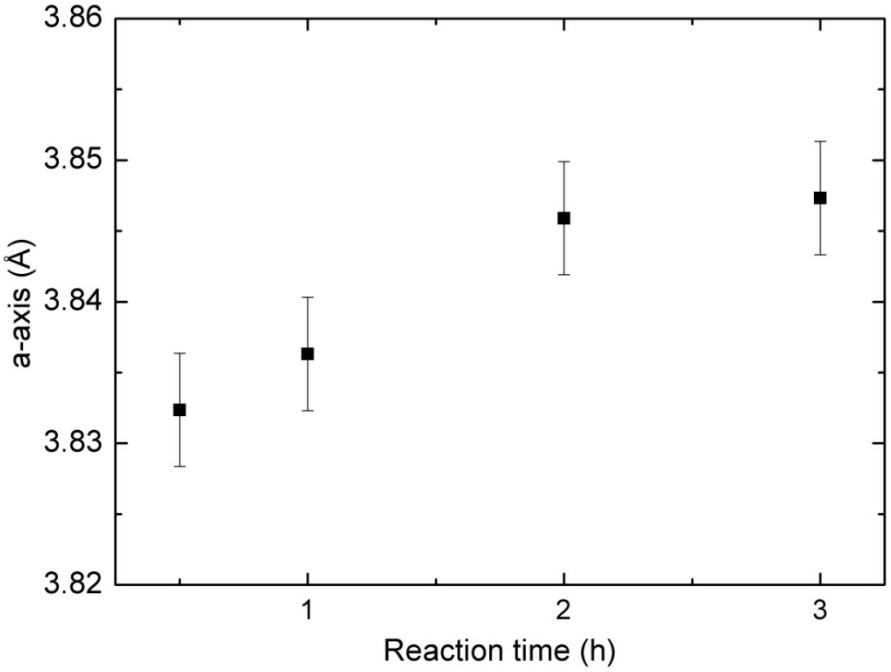


**Figure 43. The effect of reaction time (h) on the a-axis (Å) of the $Pt_{0.5}Rh_{0.5}$ NP's**

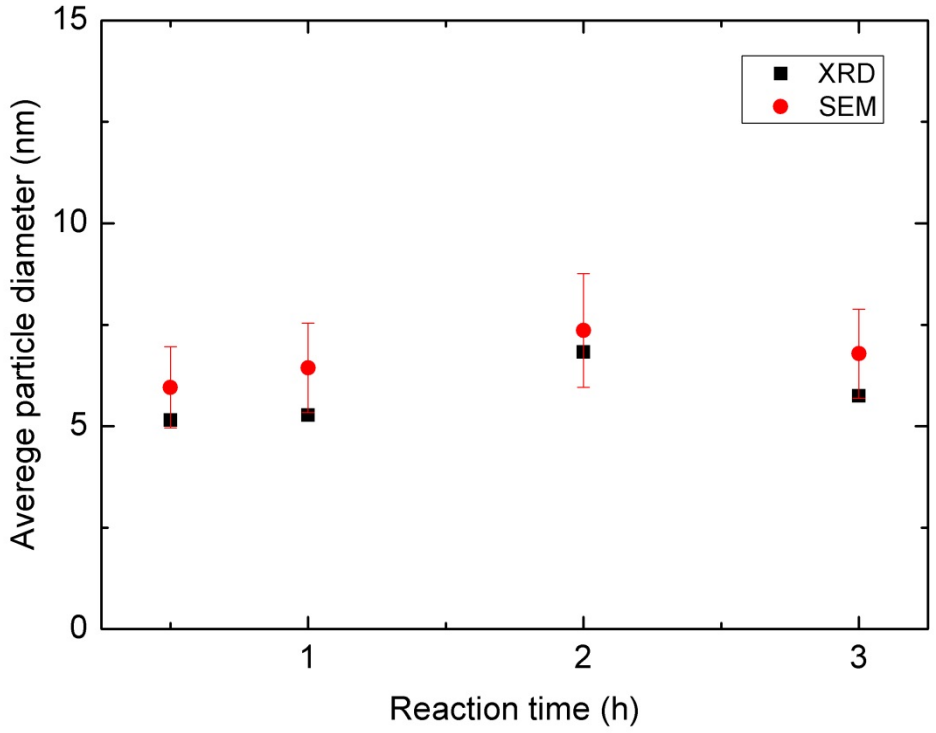


**Figure 44. A comparison of the average particle sizes given by PXD and SEM imaging for $Pt_{0.50}Rh_{0.50}$ with increasing reaction time).**

In Figures 45-48 are SEM images showing the morphology and particle size of the $Pt_{0.50}Rh_{0.50}$ particles synthesized with the different reaction times presented together with the corresponding histograms that are visualizing the particle size distribution. The histograms show a broad Gaussian like distribution. The corresponding SEM images show the different shapes and sizes of the nanoparticles. The images show the presence of agglomerates in all the syntheses.

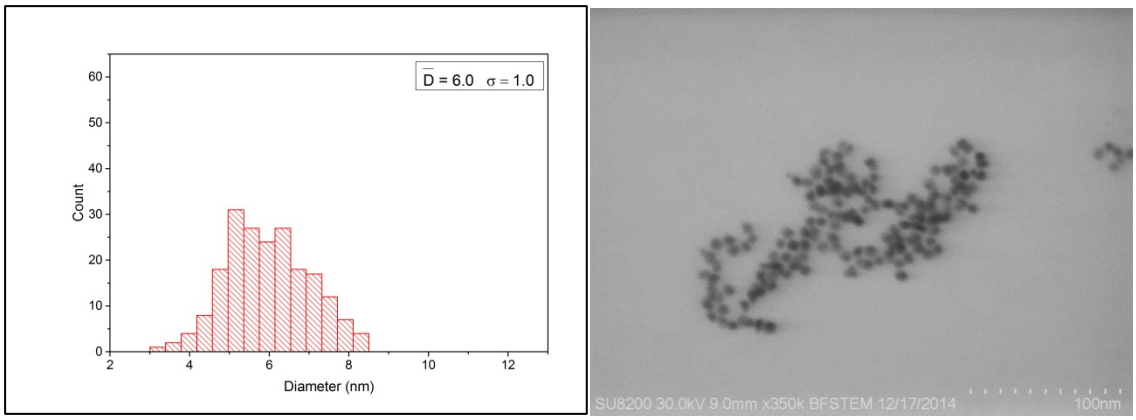


**Figure 45. The 0.5 synthesis of $Pt_{0.50}Rh_{0.50}$. Left; Histogram showing particle size distribution of 200 measured nanoparticles, with a Gaussian distribution. Average size ($\overline{D}$) and standard deviation (σ) is stated in the inset. Right; SEM image using the BFSTM detector showing a representative fraction of the particles obtained in the synthesis.**

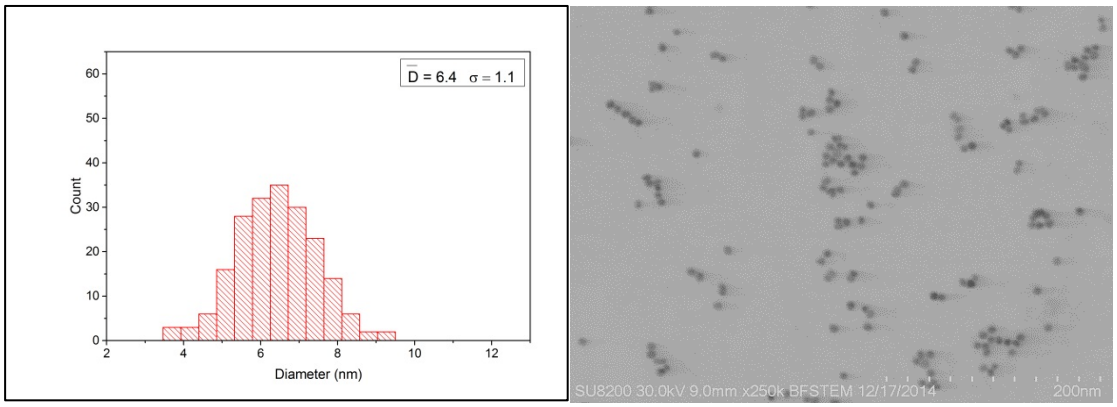


**Figure 46. The 1 h synthesis of $Pt_{0.50}Rh_{0.50}$. Left; Histogram showing particle size distribution of 200 measured nanoparticles, with a Gaussian distribution. Average size ($\overline{D}$) and standard deviation (σ) is stated in the inset. Right; SEM image using the BFSTM detector showing a representative fraction of the particles obtained in the synthesis.**

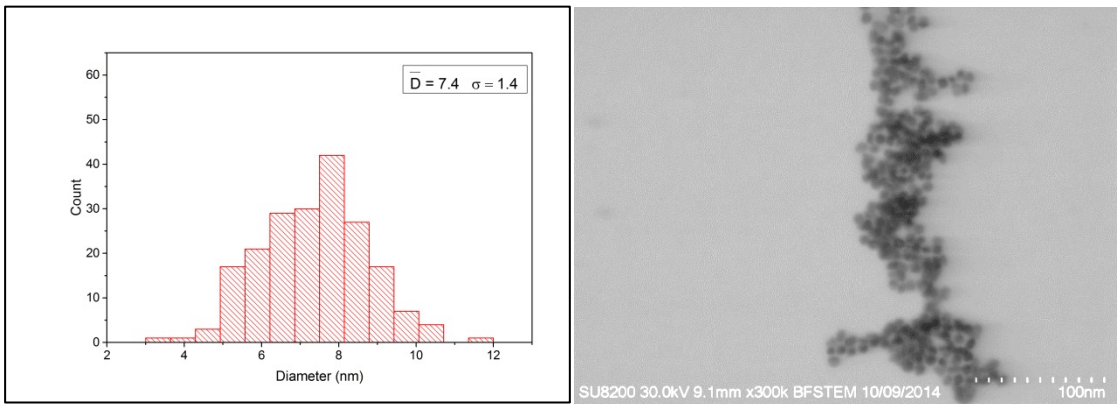


**Figure 47. The 2 h synthesis of $Pt_{0.50}Rh_{0.50}$. Left; Histogram showing particle size distribution of 200 measured nanoparticles, with a Gaussian distribution. Average size ($\overline{D}$) and standard deviation (σ) is stated. Right; SEM image using the BFSTM detector showing a representative fraction of the particles obtained in the synthesis.**

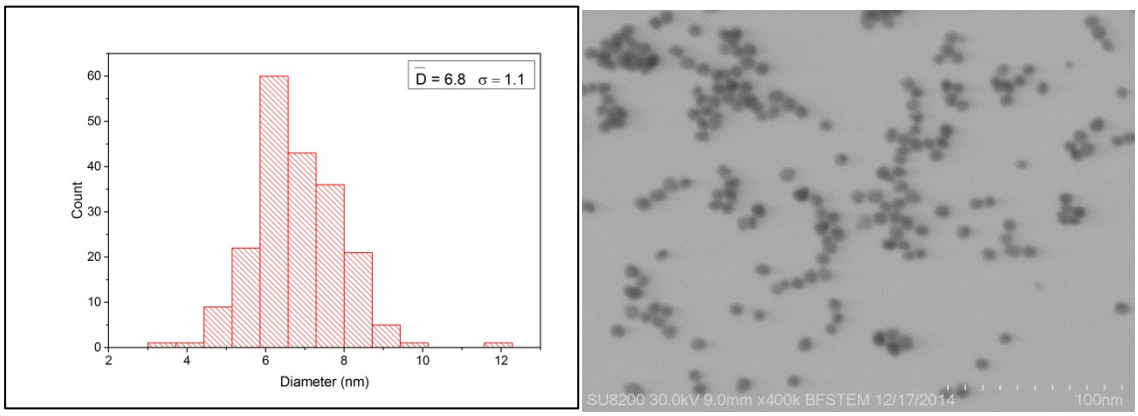


**Figure 48. The 3 h synthesis of $Pt_{0.50}Rh_{0.50}$. Left; Histogram showing particle size distribution of 200 measured nanoparticles, with a Gaussian distribution. Average size ($\overline{D}$) and standard deviation (σ) is stated in the inset. Right; SEM image using the BFSTM detector showing a representative fraction of the particles obtained in the synthesis.**

The obtained average particles size ($\overline{D}$) found form SEM measurements are reported in Figure 44, which shows that the particle size is quite constant, maybe increasing slightly. The trend reported with basis in SEM data corresponds to the average particle size estimated by the PXD. The broad size distribution in the SEM measurements is the reason for the relatively large standard deviation (σ) given in Figure 44.

***Rhodium (Rh) Nanoparticles***

For Pt1-xRhx, x = 1.00, the PXD patterns for the reaction time 0.5 h, 1 h, 2 h and 3 is presented in Figure 49. The reflections belonging to the Si-reference are marked with *, and the different reflections belonging to Rh (crystallizing in a fcc type structure) are marked with their respective (hkl) values. No extra diffraction peaks were observed, i.e. the samples are considered to be phase pure. For all the different reaction times, the (200) peak of Rh is completely overlapping with the Si-reference peak. In the inset is an enlargement of the Rh (111) peak, showing that the peak of the 2h synthesis is shifted to the right with respect to the three other syntheses. The a-axes obtained from the (111) reflections of the syntheses are reported in Figure 50. Within the estimated uncertainty of the unit cell determination method, the a-axis for Rh is the same for all samples except the particles produced with a 2 hour reaction time, which has a smaller a-axis with relative to the three other syntheses. The smaller a-axis of the 2h synthesis corresponds to the shifted peak in Figure 49. The reason for the derivation for the 2 h reaction time sample is not understood, and will be elaborated further in the Discussion. The a-axis of the 2 h reaction corresponds well with literature, the others are slightly higher.

The average particle sizes of the rhodium nanoparticles obtained from the (111) peaks in Figure 49 were plotted with respect to the different reaction times, and is presented in Figure 51. Within the uncertainty used for the method the sizes are the same, with D = ~5 nm.

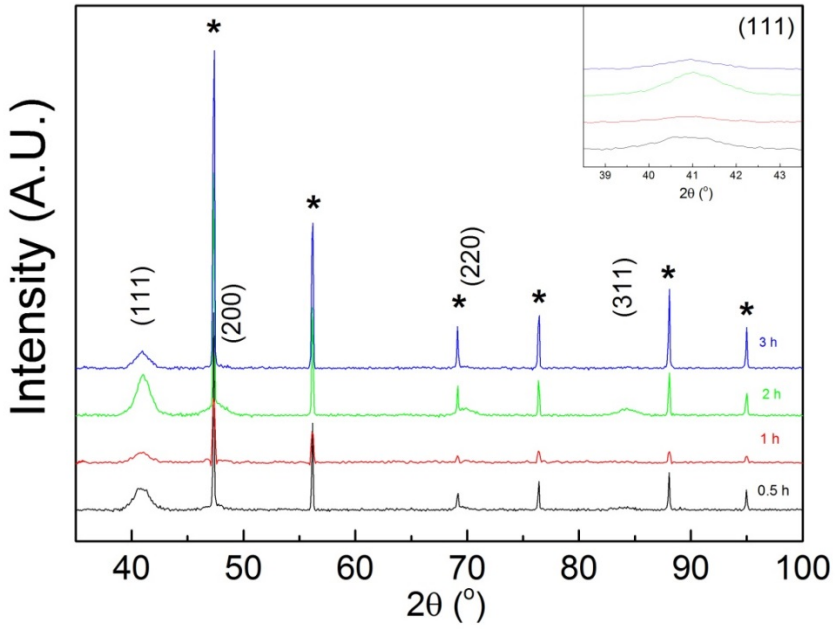


**Figure 49. PXD patterns of rhodium nanoparticles synthesized with reaction times of 0.5 h, 1 h, 2 h and 3 h**

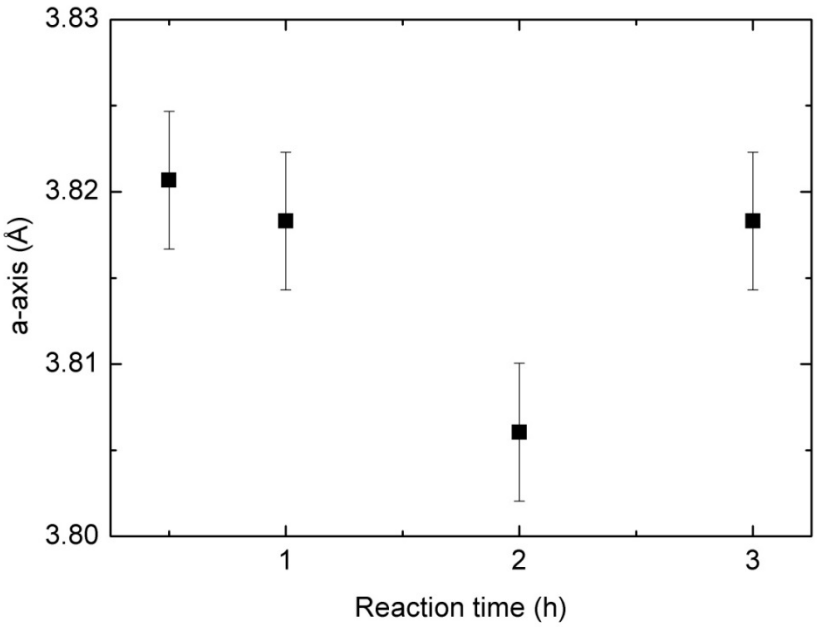


**Figure 50. The effect of reaction time (h) on the a-axis (Å) of the Rh NP's.**

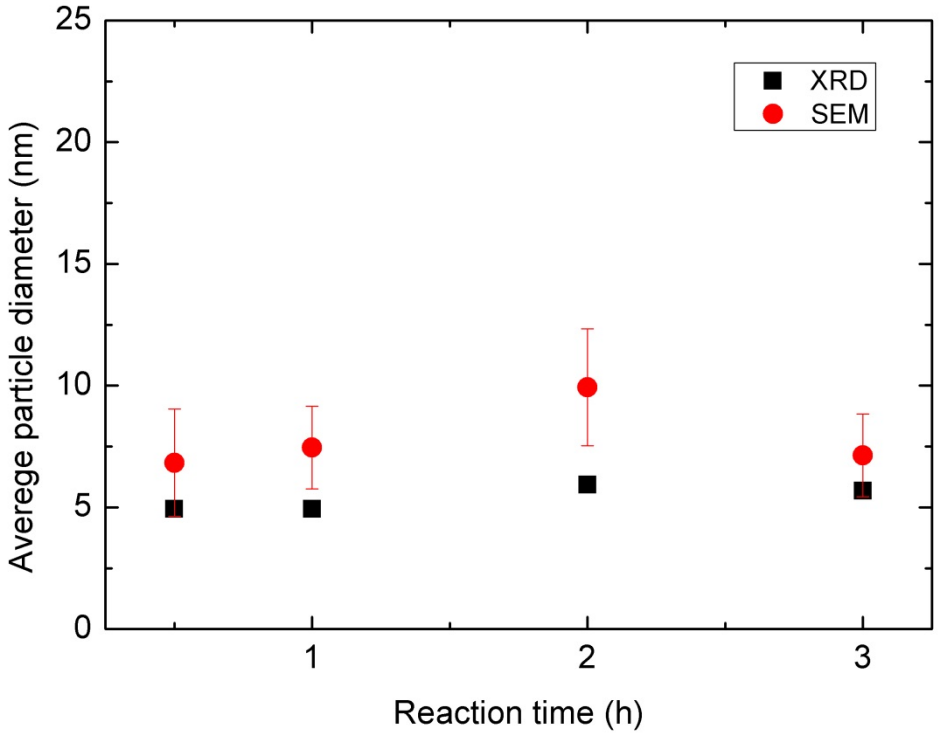


**Figure 51. Comparison of the average particle size estimate given by PXD (based on FWHM of the (111) peak) and SEM imaging (with the standard deviation) for the different reaction times of Rh.**

The size distribution given by the SEM measurements of nanoparticles of the different time variations, and a corresponding SEM image from the same synthesis is presented in Figures 52-55. The histograms show a broad distribution. The corresponding SEM images show the different shapes and sizes of the nanoparticles.

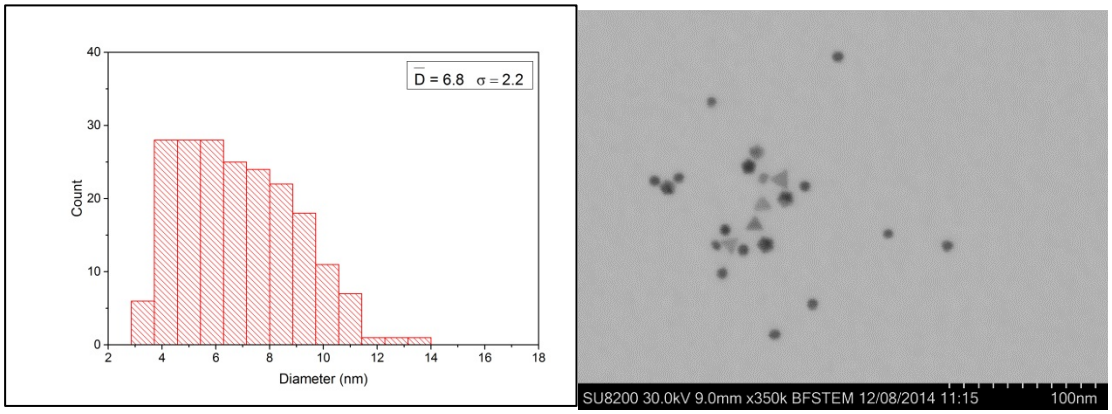


**Figure 52. The 0.5 h Rh synthesis. Left; Histogram showing size distribution of 200 measured nanoparticles, where a broad size distribution is found. Average size ($\overline{D}$) and standard deviation (σ) is stated in the inset. Right; BFSTEM image of a representative part of the particles produced in the synthesis.**

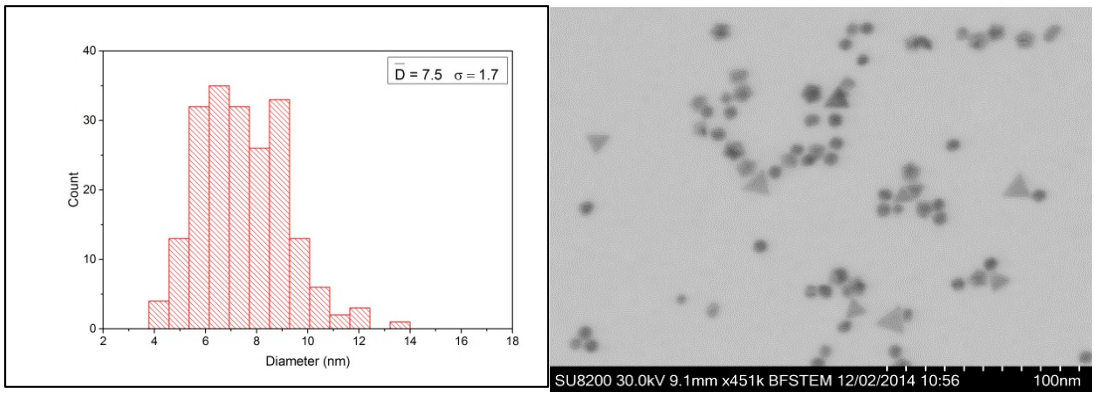


**Figure 53. The 1 h synthesis. Left; Histogram showing size distribution of 200 measured nanoparticles, where a Gaussian distribution can be indicated. Average size ($\overline{D}$) and standard deviation (σ) is stated in the inset. Right; BFSTEM image of a representative part of the particles produced in the synthesis.**

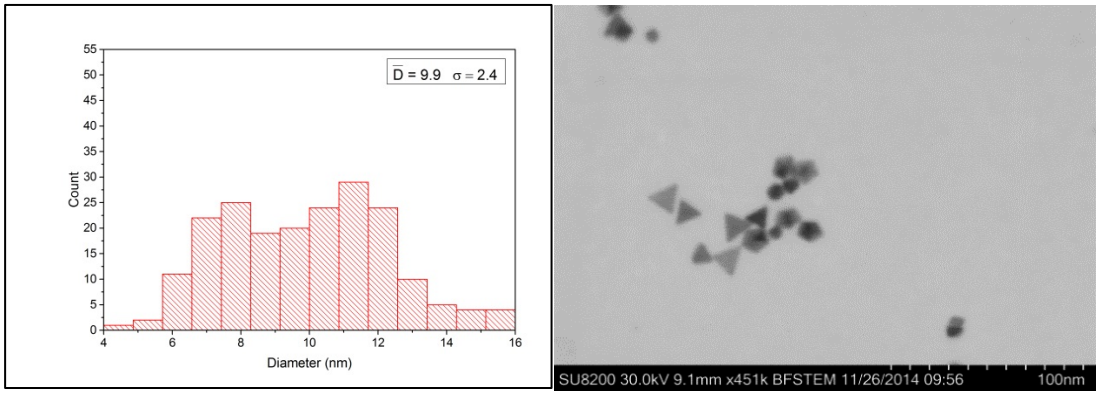


**Figure 54. The 2 h synthesis. Left; Histogram showing size distribution of 200 measured nanoparticles, with an indication of a Gaussian distribution. Average size ($\overline{D}$) and standard deviation (σ) is stated in the inset. Right; BFSTEM image of a representative part of the particles produced in the synthesis.**

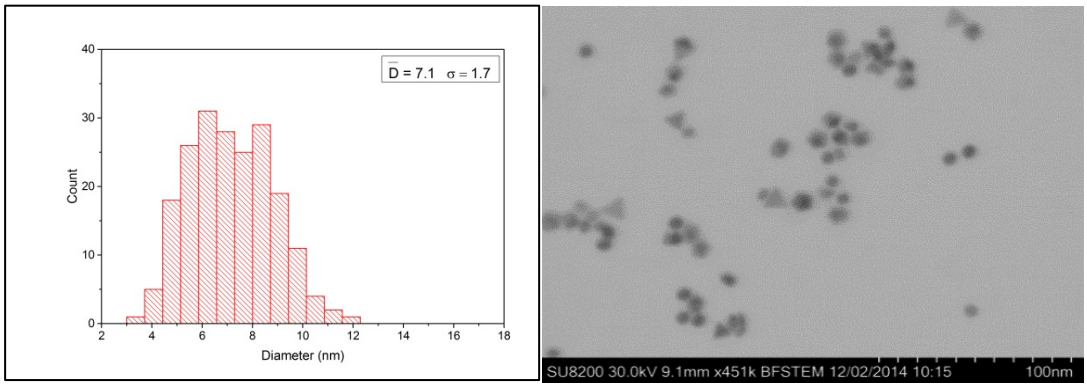


**Figure 55. The 3 h synthesis. Left; Histogram showing size distribution of 200 measured nanoparticles, with an indication of a Gaussian distribution. Average size ($\overline{D}$) and standard deviation (σ) is stated in the inset. Right; BFSTEM image of a representative part of the particles produced in the synthesis**

From the evaluation of the nanoparticle diameters (histograms),it can be observed that the average diameter of the nanoparticles are almost constant for the four investigated reaction times, see Figure 51. The trend corresponds to the average particle distribution estimated by the PXD patterns. The broad size distribution in the SEM measurements is the reason for the relatively large standard deviation (σ) in the sizes reported from the SEM investigations.

### 4.1.3 Effect of reaction temperature on nanoparticle size

For Pt1-xRhx, the effect of reaction temperature (190 °C, 200 °C, 210 °C, 220 °C and 230 °C) on the nanoparticle size, particle size distribution as well as unit cell dimensions was investigated for the three compositions x = 0.00, x = 0.50 and x = 1.00. For the listed reaction temperatures, the reaction time was kept constant at 2 h, metal precursor: surfactant (PVP) ratio was 1 : 10 and concentrations were constant (20 mL solvent). In Figures 56, 63 and 70 are the obtained powder X-ray diffractograms PXD patterns of the synthesized particles presented. The PXD patterns show that all samples are phase pure, and the reflections belonging to the Pt1-xRhx phase can be indexed as a fcc type structure. Further, reflections assigned to the added silicon reference is denoted with '*'. The first reflection from $Pt_{1-x}Rh_x$ in each X-ray pattern, the (111) peak, has the highest intensity and does not overlap with any of the Si-standard peaks, and was therefore chosen to estimate both the unit cell dimensions as well as the crystallite size for each sample. The estimated unit cell dimensions for the three compositions are given in Figures 57, 64 and 71, and the particle sizes via the Scherrer approach are reported in Figures 58, 65 and 72. Correspondingly, for each of the samples, SEM images were collected and the particle size and particle size distribution was estimated from 200 nanoparticles. The SEM images and the corresponding histograms of the particle sizes are reported in Figures 59-62, 66-69 and 72-76.

In the following a more detailed evaluation obtained Pt, $Pt_{50}Rh_{50}$ and Rh particles synthesized at the different temperatures with respect to particle size, particle size distribution and unit cell dimensions will be reported.

***Platinum (Pt) nanoparticles***

In Figure 56 are the PXD patterns for $Pt_{1-x}Rh_x$ samples, x = 0.00, synthesized at the reaction temperatures 190 °C, 200 °C, 210 °C, 220 °C and 230 °C presented. Careful inspection of the diffractograms indicates that all samples are phase pure. All reflections can either be assigned to Pt (labeled with its Miller indexes) or to the added Si-reference phase (reflections labelled '*'). In the inset is an enlargement of the Pt (111) peak. Inspecting the FWHM of the (111) reflection of Pt, show that the peak width is reducing when the reaction temperature is increasing.

Calculated a-axis values, with basis in the (111) peak for the different Pt samples, are plotted versus synthesis temperature in Figure 57. The reported unit cell dimensions must be considered to be equal, within the uncertainty of the method. The obtained a-axis is in line

with earlier reported values obtained for Pt bulk samples, but slightly shorter than what obtained for Pt NPs, see Table 2Table 3

Using the Scherrer formula, the crystallite size for the different Pt samples are calculated form the FWHM of the (111) peaks in Figure 56, and the obtained average particle sizes are reported in Figure 58. It is found that the particle size is slightly increasing with the increasing reaction temperature, as indicated in the decreased broadening of the peaks in Figure 56.

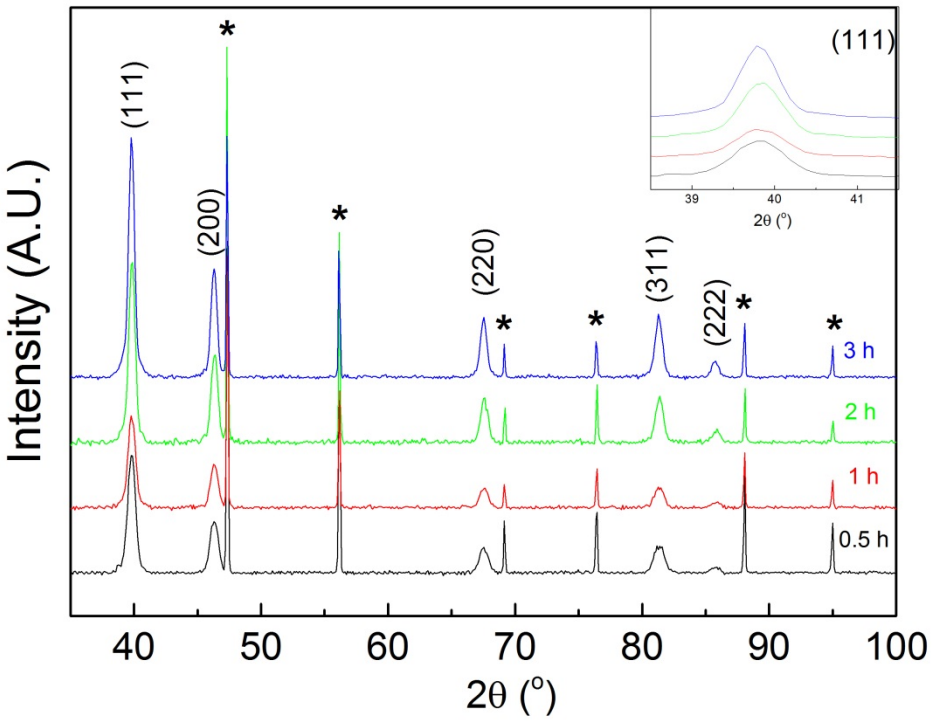


**Figure 56. PXD patterns of obtained Pt particles synthesized at selected temperatures in the interval from 190 °C to 230 °C**

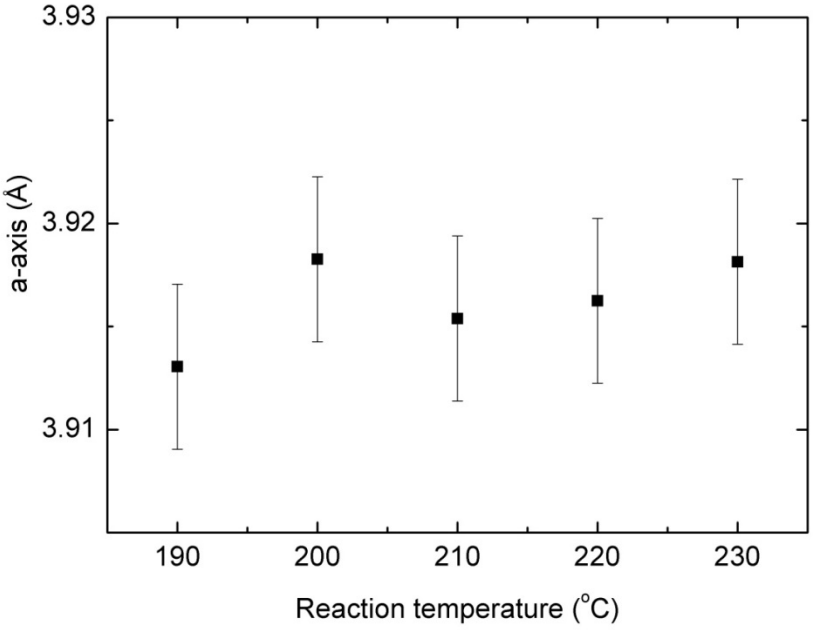


**Figure 57. The a-axes of the platinum nanoparticles synthesised at selected temperature from 190 °C to 230 °C.**

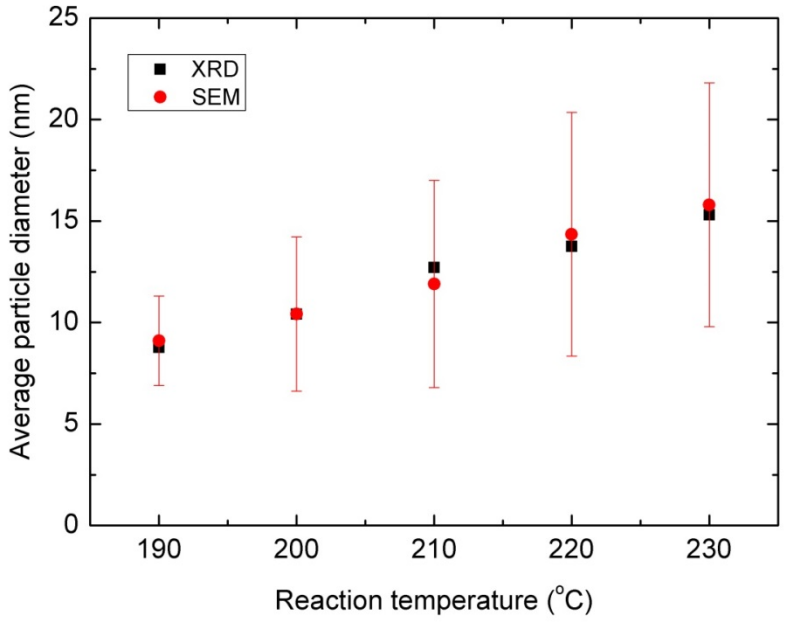


**Figure 58. Comparison of the estimated particle size of Pt NP's synthesized at 190°C, 200°C, 210°C, 220°C and 230°C, as given by PXD and SEM imaging. The standard deviation given by the SEM measurements is also given, and shows a large standard deviation.**

SEM investigations of the Pt samples synthesized at the different reaction temperatures were carried out with focus on extracting the average particle size and the particle size distribution. Representative images of the particles produced in the different experiments as well as the obtained histograms for evaluation the diameter of 200 nanoparticles for the 190 °C, 200°C, 210 °C and 230°C syntheses are reported in Figures 59-62. The 220 °C synthesis is the same as the 2 hour synthesis and can be found in Figure 40. The histograms show a clear double size distribution. The SEM images further show that the nanoparticles have different sizes and shapes, and the presence of agglomerates.

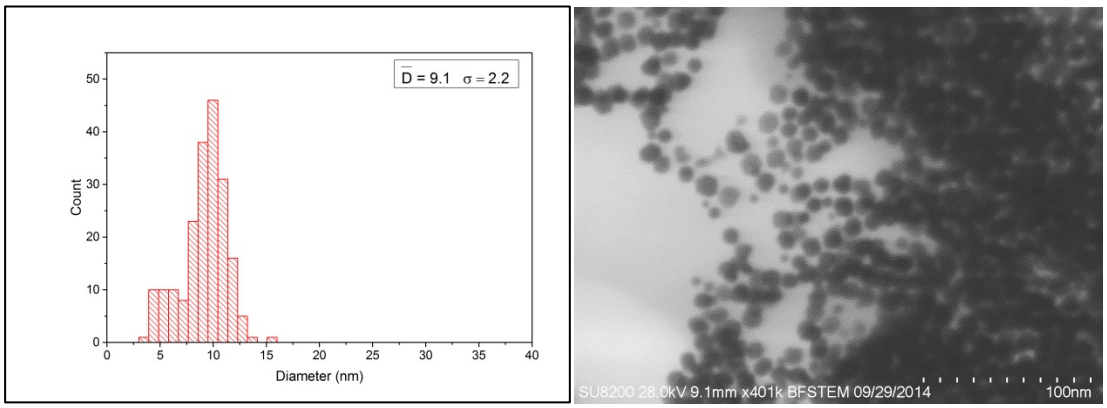


**Figure 59. The 190 °C Pt synthesis. Left; Histogram showing size distribution of 200 measured nanoparticles, with a double distribution. Average size ($\overline{D}$) and standard deviation (σ) is stated in the inset. Right; BFSTEM image of a representative batch of the synthesized particles, showing large and small particles of different shapes.**

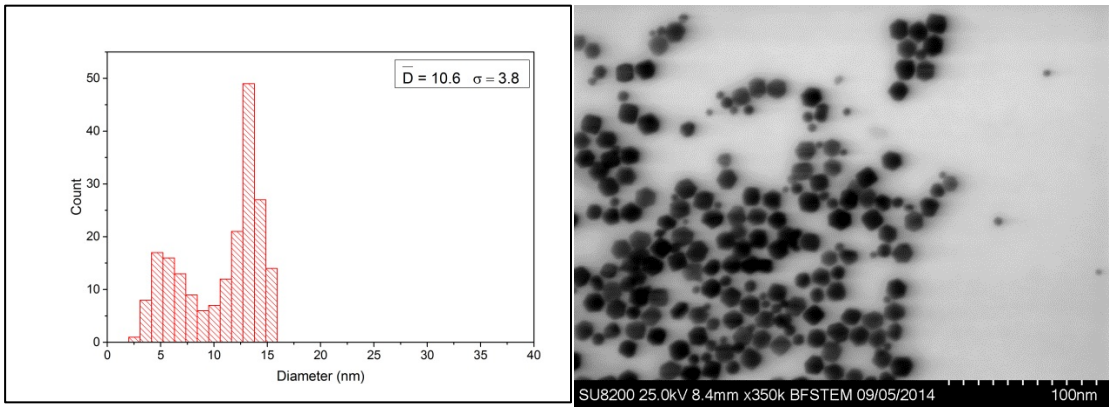


**Figure 60. The 200 °Csynthesis. Left; Histogram showing size distribution of 200 measured nanoparticles, with a double distribution. Average size ($\overline{D}$) and standard deviation (σ) is stated in the inset. Right; BFSTEM image of the synthesis, showing large and small particles with different shapes**

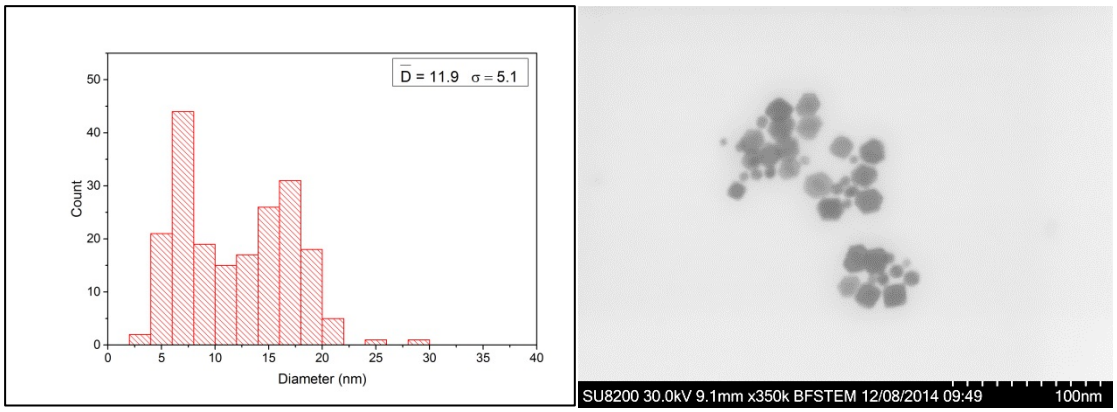


**Figure 61. The 210 °C synthesis. Left; Histogram showing size distribution of 200 measured nanoparticles, with a double distribution. Average size ($\overline{D}$) and standard deviation (σ) is stated in the inset. Right; BFSTEM image of the synthesis, showing large and small particles with different shapes**

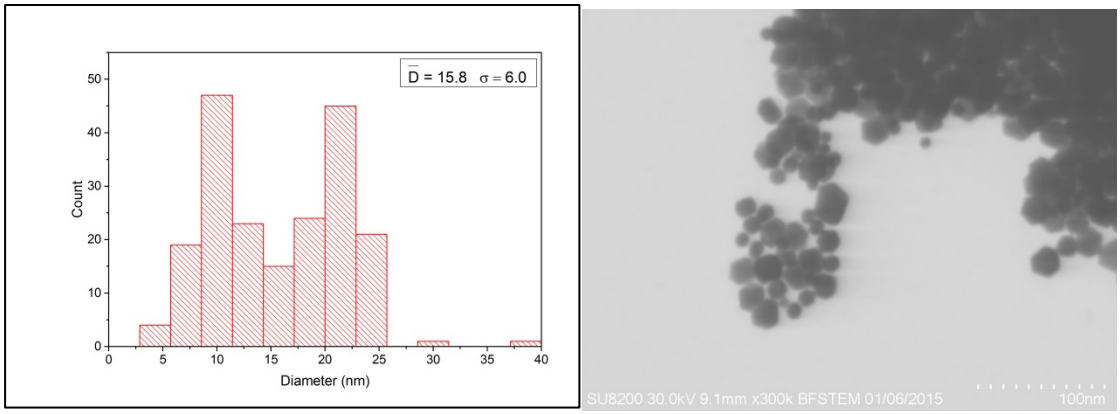


**Figure 62. The 230 °Csynthesis. Left; Histogram showing size distribution of 200 measured nanoparticles, with a double distribution. Average size ($\overline{D}$) and standard deviation (σ) is stated in the inset. Right; BFSTEM image of the synthesis, showing large and small particles with different shapes**

The obtained average particle sizes ($\overline{D}$) versus reaction temperature, found by SEM, are included to Figure 58. It is clear that the particle size is increasing slightly with increasing reaction temperature. The trend obtained by SEM corresponds to the average particle distribution estimated by the PXD patterns. The broad size distribution in the SEM measurements is the reason for the relatively large standard deviation (σ) given in Figure 58.

### *Platinum-rhodium ($Pt_{0.50}Rh_{0.50}$) bimetallic nanoparticles*

For $Pt_{1-x}Rh_x$, x = 0.5, the PXD patterns for the reaction temperature (190 °C, 200 °C, 210 °C, 220 °C and 230 °C) is presented in Figure 63. The different reflections belonging to the nanoparticles are with Miller indexes, and the reflections belonging to the Si-reference is marked with *. In the inset is an enlargement of the 111 peak, and close inspection shows that the peaks are slightly shifted with respect to each other. The peak of the 220 °C is shifted to higher 2θ compared to the lower reaction temperatures, and the peak of the 230 °C is shifted to lower 2θ with respect to the lower reaction temperatures.

The estimated a-axis as a function of reaction temperature was found form the (111) peaks in Figure 63 are reported in Figure 64. They are in general lower than the ones reported in Table 2. It can be observed that the a-axis increase with increasing synthesis duration from a = 3.833Å (190 °C) to a = 3.851 Å (230 °C), and shows a close to linear relationship with exception to the 210 °C (a= 3.836Å) synthesis which has a smaller a-axis than the linear trend. The reported unit cell dimensions must be concluded to be different, as an observed expansion of 0.018 Å is beyond the uncertainty of the applied method. Presently no exact explanation for the observation can be reported. This does not correspond to the shift of the PXD patterns in Figure 63. The reason for this is not understood, and will be elaborated in the discussion.

The average particle sizes of the four $Pt_{0.50}Rh_{0.50}$ samples were estimated with basis in the FWHM of the (111) diffraction peaks presented in Figure 63, and the obtained results are reported in Figure 65. The results show minor variations, with D = ~5-7 nm.

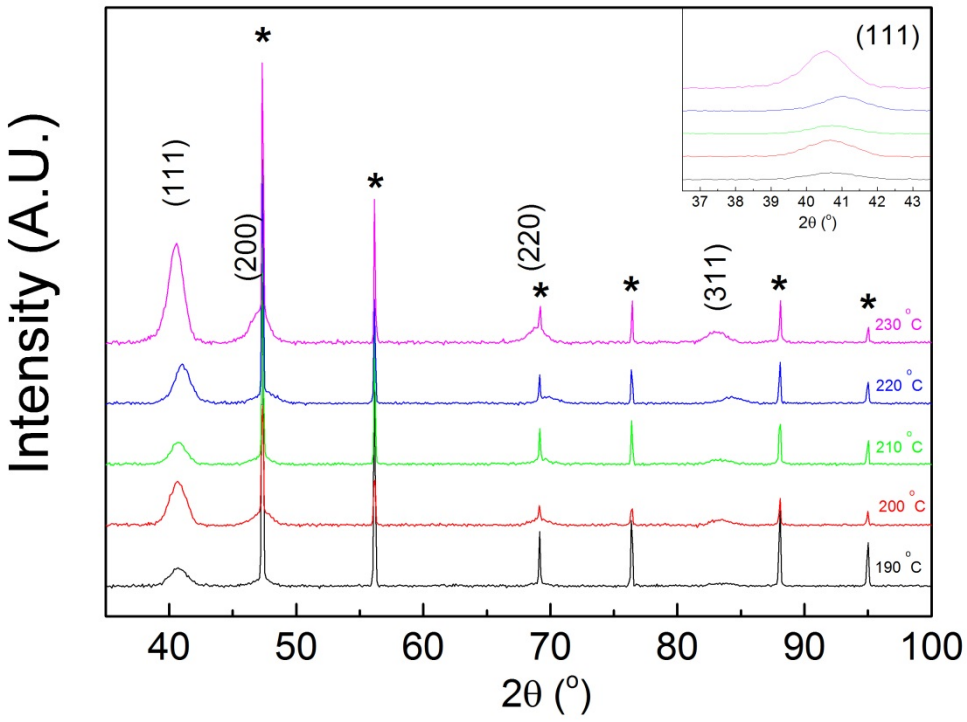


**Figure 63. Obtained PXD patterns of $Pt_{0.5}Rh_{0.5}$ nanoparticles synthesized at selected temperatures in the interval from 190 °C to 230 °C.**

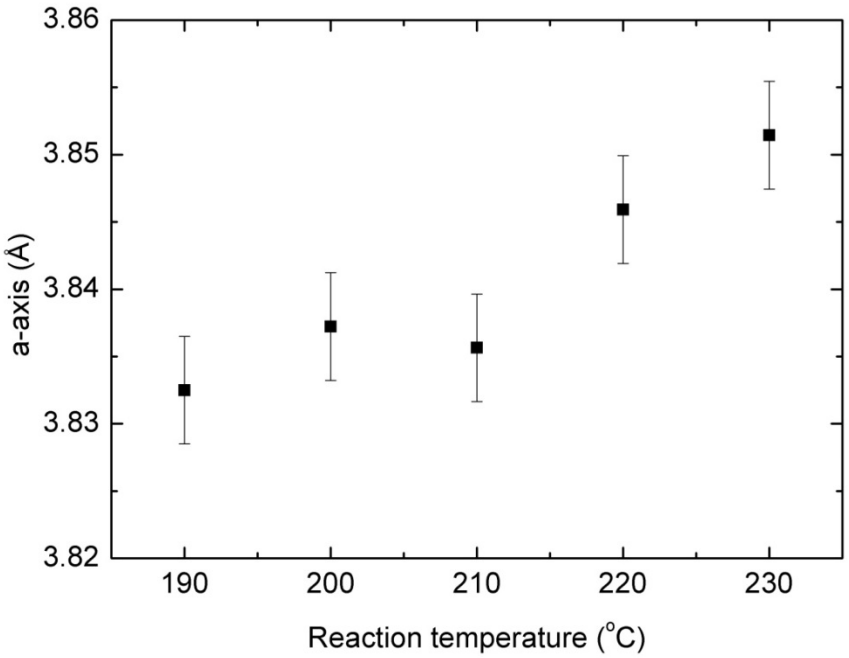


**Figure 64. The effect of the reaction temperature on the a-axis of the $Pt_{0.5}Rh_{0.5}$ syntheses.**

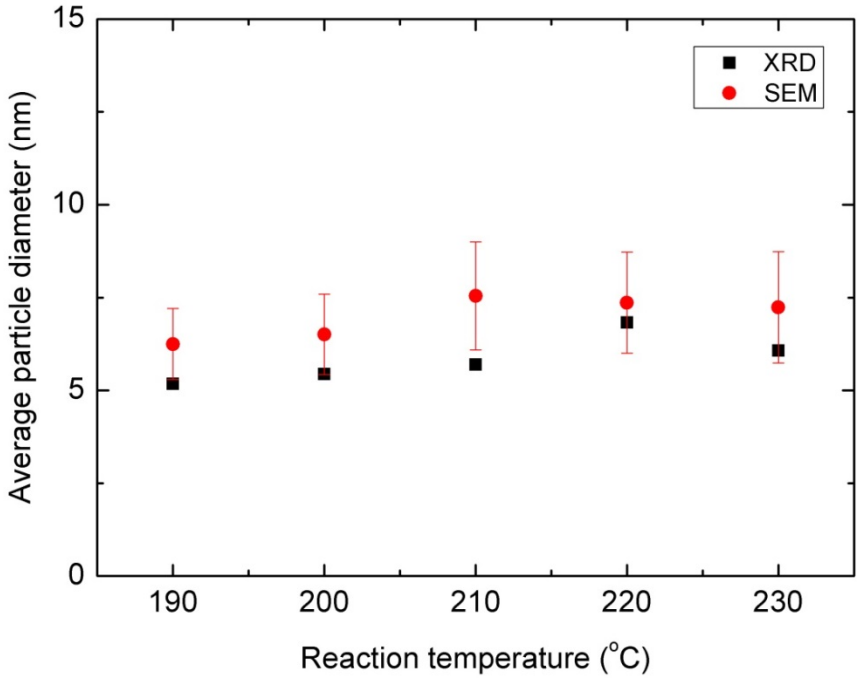


**Figure 65. Comparison of the estimated particle size of $Pt_{0.5}Rh_{0.5}$ NP's synthesized at 190°C, 200°C, 210°C, 220°C and 230°C, as given by PXD and SEM imaging. The standard deviation given by the SEM measurements is also given, and shows a large standard deviation**

SEM investigations of the $Pt_{0.5}Rh_{0.5}$ samples synthesized at the different reaction temperatures were carried out with focus on extracting the average particle size and the particle size distribution. Representative images of the particles produced in the different experiments as well as the obtained histograms for evaluation the diameter of 200 nanoparticles for the 190 °C, 200°C, 210 °C and 230°C syntheses are reported in Figures 66-70. The 220 °C synthesis is the same as the 2 hour synthesis and can be found in Figure 47. The histograms show a broad, Gaussian-like distribution. The SEM images further show that the nanoparticles have different sizes and shapes, and the presence of agglomerates.

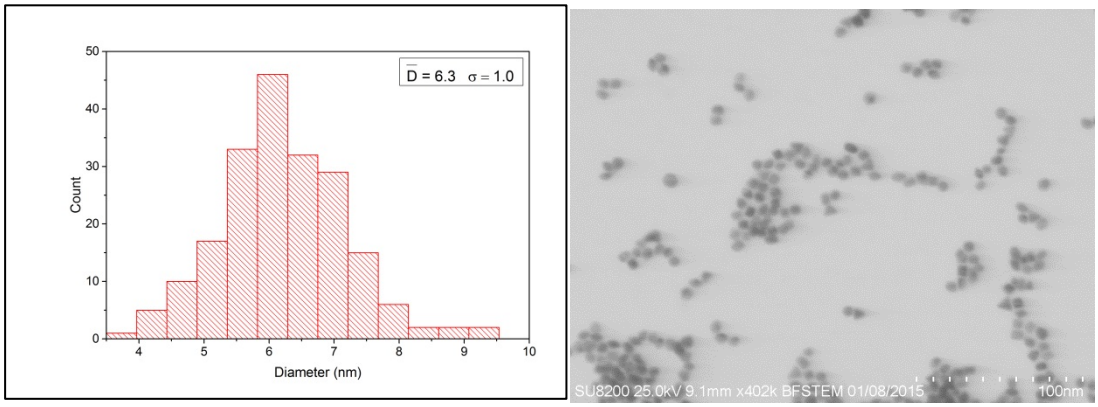


**Figure 66. The 190 °C $Pt_{0.5}Rh_{0.5}$ synthesis. Left; Histogram showing size distribution of 200 measured nanoparticles, with a double distribution. Average size ($\overline{D}$) and standard deviation (σ) is stated in the inset. Right; BFSTEM image of a representative batch of the synthesized particles, showing large and small particles of different shapes.**

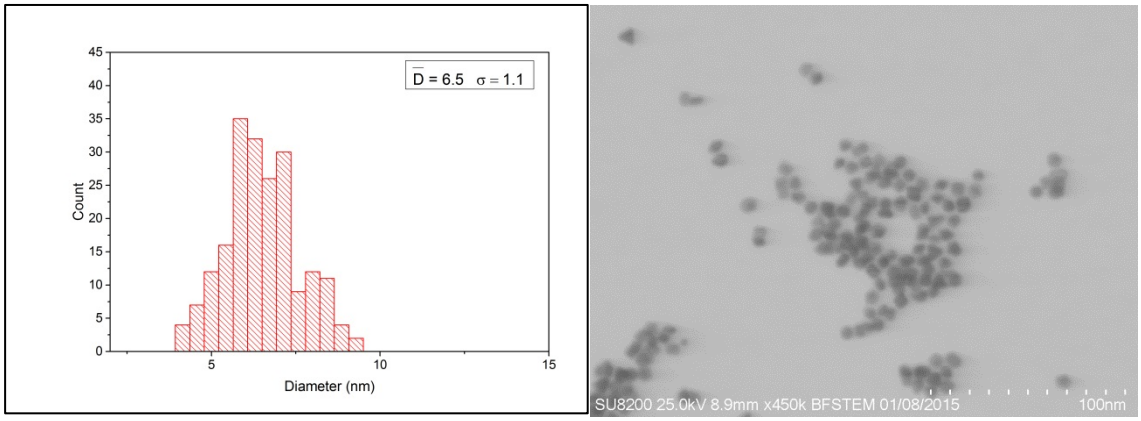


**Figure 67. The 200 °C $Pt_{0.5}Rh_{0.5}$ synthesis. Left; Histogram showing size distribution of 200 measured nanoparticles, with a double distribution. Average size ($\overline{D}$) and standard deviation (σ) is stated in the inset. Right; BFSTEM image of a representative batch of the synthesized particles, showing agglomerates of large and small particles of different shapes.**

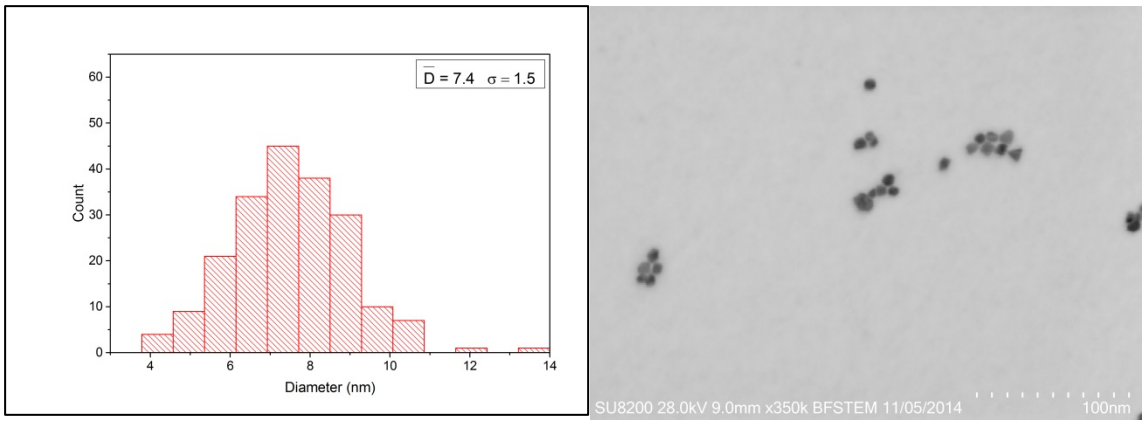


**Figure 68. The 210 °C $Pt_{0.5}Rh_{0.5}$ synthesis. Left; Histogram showing size distribution of 200 measured nanoparticles, with a double distribution. Average size ($\overline{D}$) and standard deviation (σ) is stated in the inset. Right; BFSTEM image of a representative batch of the synthesized particles, showing agglomerates of large and small particles of different shapes.**

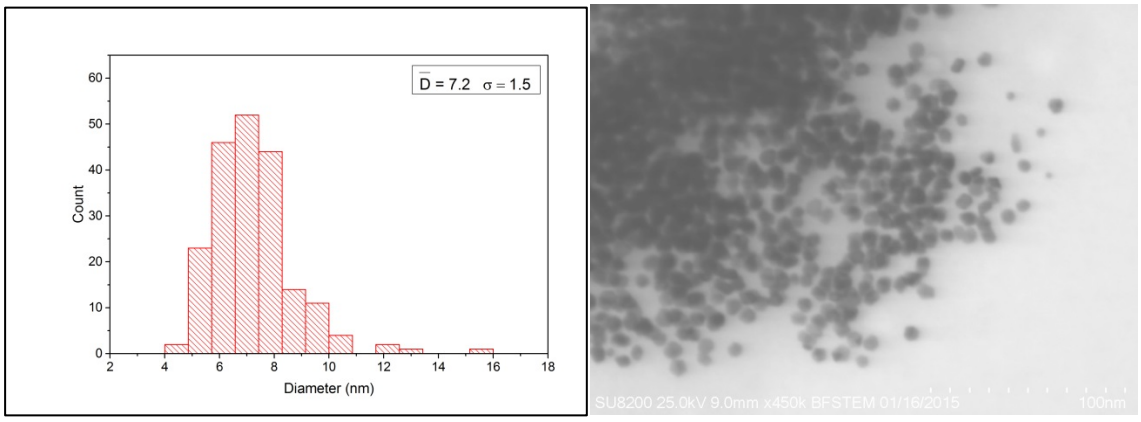


**Figure 69. The 230 °C $Pt_{0.5}Rh_{0.5}$ synthesis. Left; Histogram showing size distribution of 200 measured nanoparticles, with a double distribution. Average size ($\overline{D}$) and standard deviation (σ) is stated in the inset. Right; BFSTEM image of a representative batch of the synthesized particles, showing agglomerates of large and small particles of different shapes.**

The obtained average particles size ($\overline{D}$) found form SEM measurements are reported in Figure 65. which shows that the particle size is quite constant. The trend reported with basis in SEM data corresponds to the average particle size estimated by the PXD. The broad size distribution in the SEM measurements is the reason for the relatively large standard deviation (σ) given in Figure 65

***Rhodium (Rh) nanoparticles***

For Pt1-xRhx, x = 1.00, the PXD patterns for the reaction temperature (190 °C, 200 °C, 210 °C, 220 °C and 230 °C) are presented in Figure 70. The different reflections are marked with the corresponding (hkl) value, and the reflections belonging to the Si-reference is marked with *. In the inset is an enlargement of the 111 peaks, and close inspection shows that the peak positions are similar.

The estimated a-axis as a function of reaction temperature was found form the (111) peaks in Figure 70 are reported in Figure 71. Within the uncertainty of the method, the reported unit cell dimensions must be considered to be equal.

The average particle sizes of the rhodium samples were estimated with basis in the FWHM of the (111) diffraction peaks presented in Figure 70 and the obtained results are reported in Figure 72. The results show minor variations, with D = ~5-6 nm.

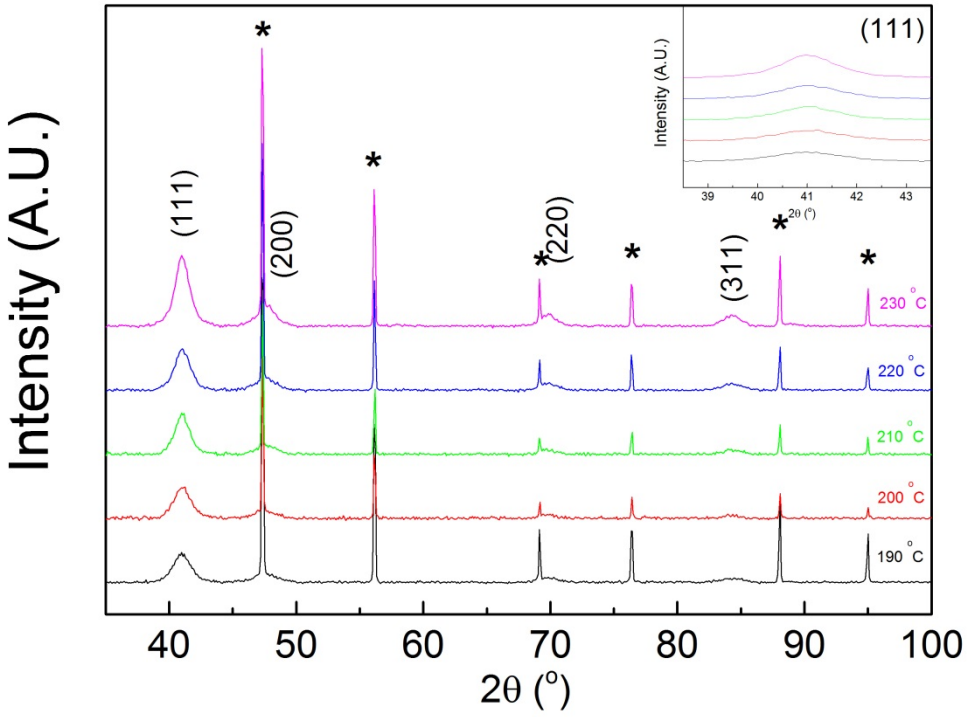


**Figure 70. For Pt1-xRhx, x = 1.00, the PXD patterns for the reaction temperature (190 °C, 200 °C, 210 °C, 220 °C and 230 °C) are presented**

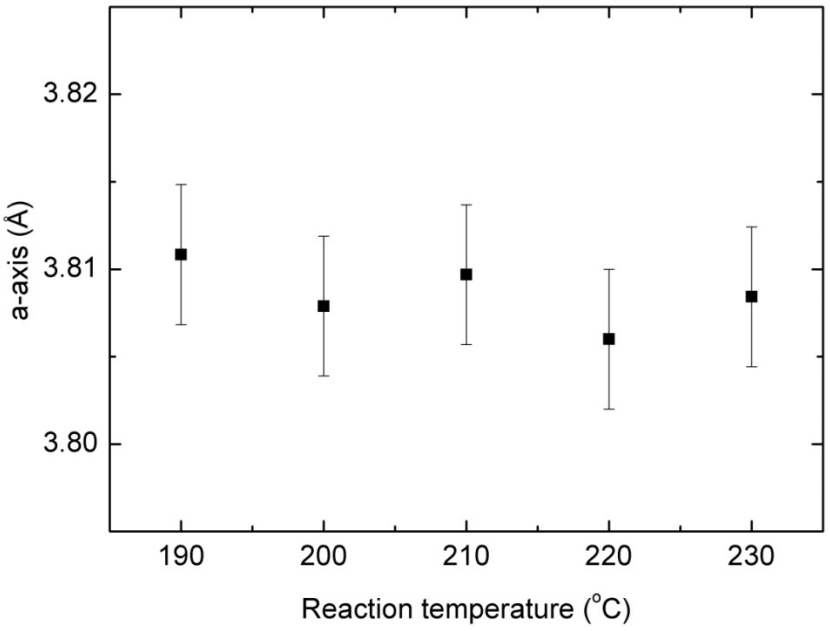


**Figure 71. The effect of the reaction temperature on the a-axis of the Rh syntheses.**

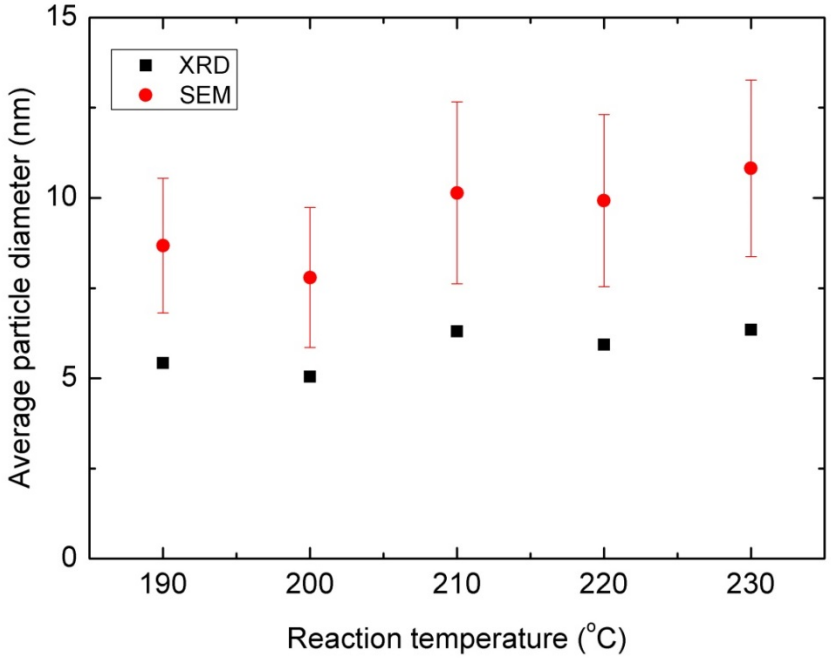


**Figure 72. Comparison of the average particle size estimate given by PXD (based on FWHM of the (111) peak) and SEM imaging (with the standard deviation) for the different reaction temperatures of Rh.**

The size distribution found by SEM investigations of the rhodium nanoparticles synthesized at the different reaction temperatures, and a corresponding SEM image from the same synthesis is demonstrated in the figure 71-74. The obtained histograms from evaluation the diameter of 200 nanoparticles for the 190 °C, 200°C, 210 °C and 230°C syntheses have a broad size distribution.

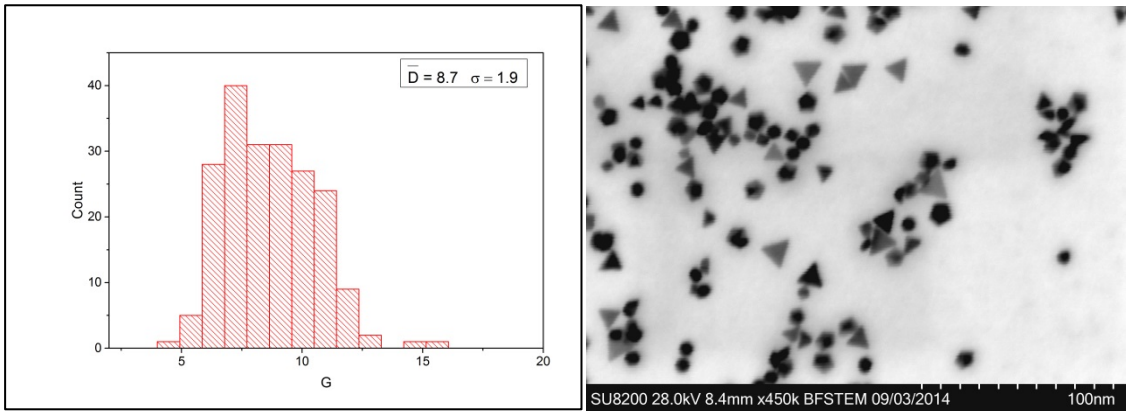


**Figure 73. The 190 °C Rh synthesis. Left; Histogram showing size distribution of 200 measured nanoparticles, with a double distribution. Average size ($\overline{D}$) and standard deviation (σ) is stated in the inset. Right; BFSTEM image of a representative batch of the synthesized particles, showing large and small particles of different shapes.**

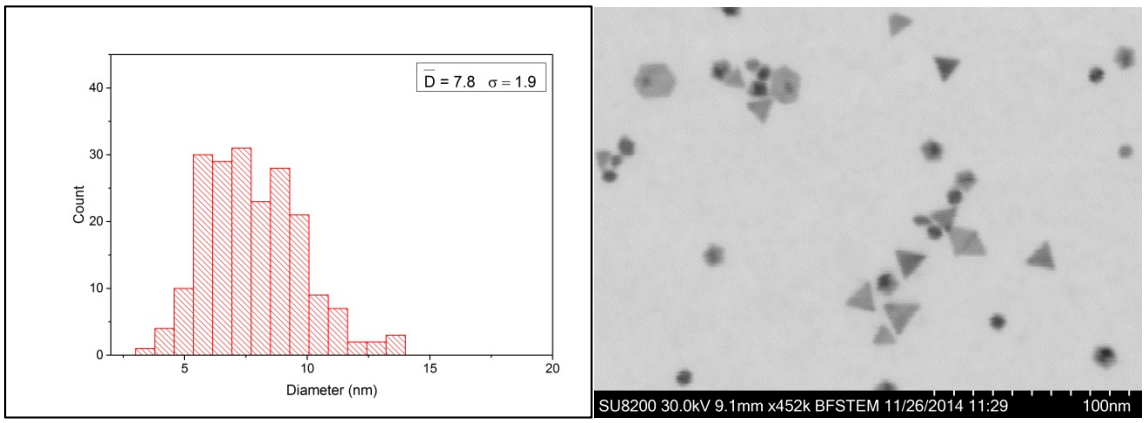


**Figure 74. The 200 °C Rh synthesis. Left; Histogram showing size distribution of 200 measured nanoparticles, with a double distribution. Average size ($\overline{D}$) and standard deviation (σ) is stated in the inset. Right; BFSTEM image of a representative batch of the synthesized particles, showing large and small particles of different shapes.**

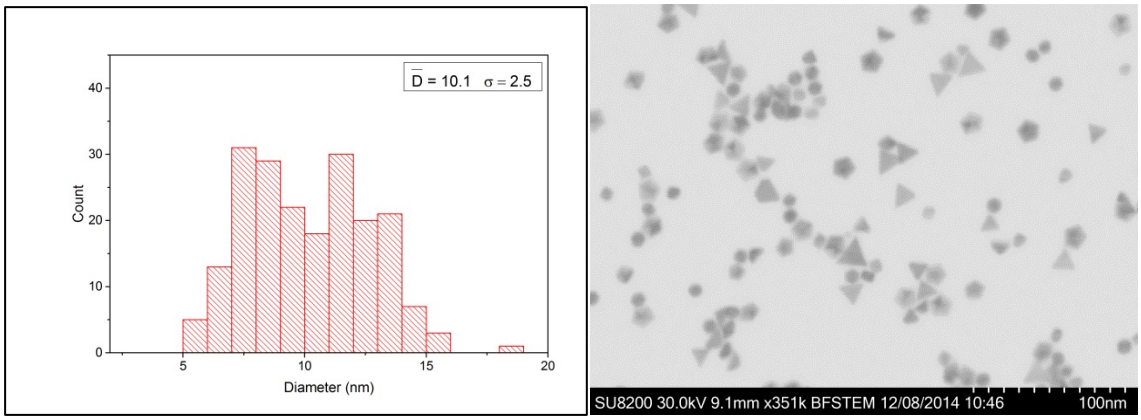


**Figure 75. The 210 °C Rh synthesis. Left; Histogram showing size distribution of 200 measured nanoparticles, with a double distribution. Average size ($\overline{D}$) and standard deviation (σ) is stated in the inset. Right; BFSTEM image of a representative batch of the synthesized particles, showing large and small particles of different shapes.**

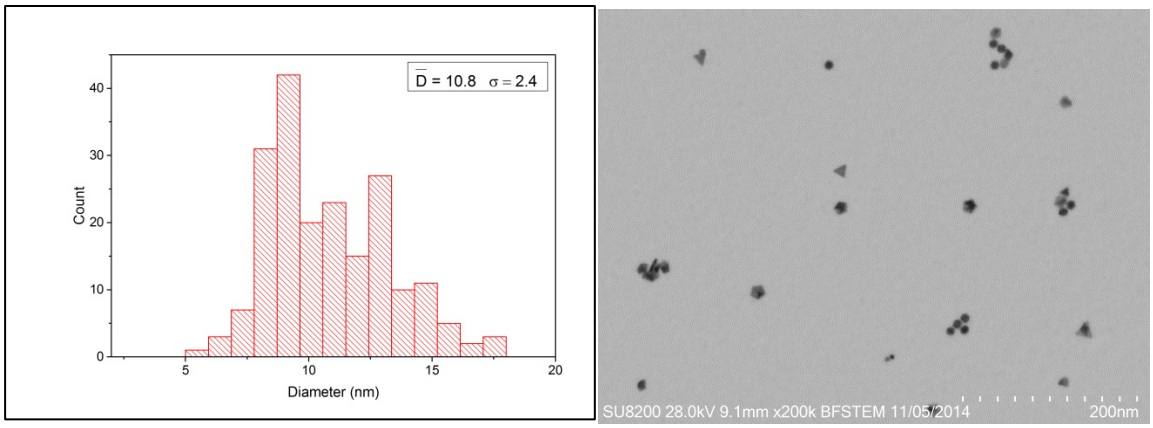


**Figure 76. The 230 °C Rh synthesis. Left; Histogram showing size distribution of 200 measured nanoparticles, with a double distribution. Average size ($\overline{D}$) and standard deviation (σ) is stated in the inset. Right; BFSTEM image of a representative batch of the synthesized particles, showing large and small particles of different shapes.**

The obtained average particles size ($\overline{D}$) found form SEM measurements are reported in Figure 72, which shows that the particle size is quite constant, maybe increasing slightly. The trend reported with basis in SEM data corresponds to the average particle size estimated by the P, however, the average particles size ($\overline{D}$) found form SEM measurements are several (2-4) nanometers bigger. The broad size distribution in the SEM measurements is the reason for the relatively large standard deviation (σ) given in Figure 72.

### 4.1.4 Effect of substitution grade on nanoparticle size and a-axis

For Pt1-xRhx, the effect of substitution grade on crystallite diameter and unit cell dimensions were investigated, for x = 0.00, 0.20, 0.50, 0.80 and 1.00. In addition the unit cell dimensions were investigated for x= 0.70All other synthesis parameters (reaction temperature, reaction time) were kept constant. In Figure 77 the obtained powder X-ray diffractograms (PXD) of the synthesized particles is presented. The PXD patterns show that all samples are phase pure, and the reflections can be indexed on a fcc type structure. The first reflection in each

diffractogram, the (111) peak, has the highest intensity and does not overlap with the Si-standard peak, and was therefore chosen to estimate crystallite size for each sample, with basis in the Scherrer equation. Correspondingly, for each of the samples, SEM images were collected and the particle size and particle size distribution was estimated from 200 nanoparticles. The SEM images and the corresponding histograms of the particle sizes are reported in 40 (x=0.00), 79(x=0.20), 47(x=0.50), 80 (x= 0.80) and 54(x=1.00),

***Platinum-rhodium (Pt1-xRhx) bimetallic nanoparticles***

For Pt1-xRhx, the PXD patterns for the substitution grades x = 0.00, 0.20, 0.50, 0.80 and 1.00 is presented in Figure 77. The reflections of metal nanoparticles are marked with the corresponding (hkl) value, and the reflections belonging to the Si-reference is marked with *. In the inset is an enlargement of the 111 peak, and the peaks are clearly shifted with respect to each other, first gradually to higher 2θ ($^0$) for x = 0.00, 0.20, 0.50, then to slightly lower 2θ ($^0$) for 0.8, and then to higher 2θ for x = 1. The lattice parameters obtained from the position of the (111) increase linearly with increasing rhodium content, and does not correspond to the shift in peak position for x = 0.80 and x=1.00. The reason for this is not understood, will be elaborated in the discussion.

The crystallite size calculated from the powder X-ray diffraction data is presented in Figure 79, and shows that the average particle size for the different substitution grades of rhodium into platinum. The average size is invariant with respect to Pt content, with exception to the 100 % Pt synthesis which has a much higher crystallite size.

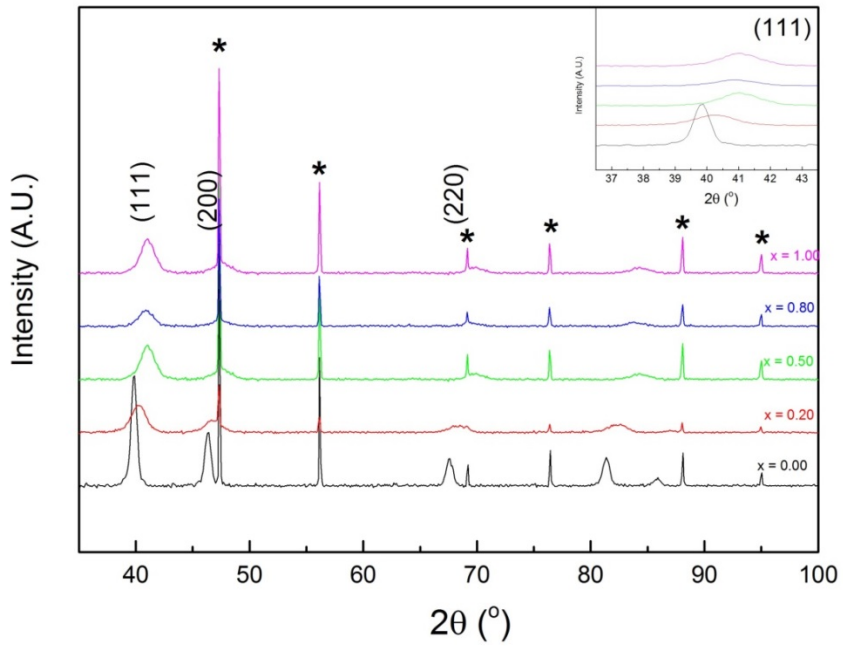


**Figure 77. PXD patterns For Pt1-xRhx, for the substitution grades x = 0.00 0.20, 0.50, 0.80 and 1.00**

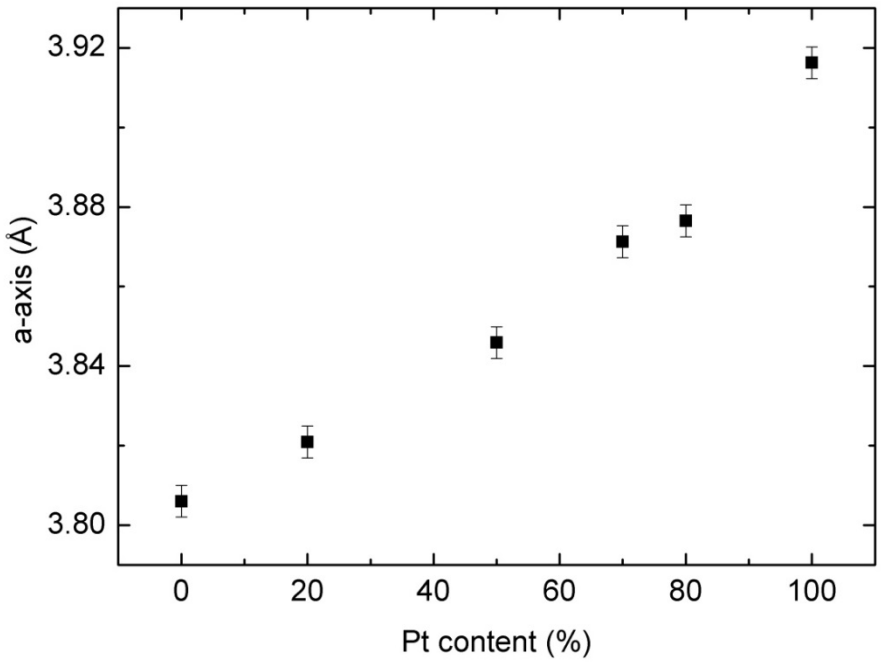


**Figure 78. The a-axis as a function of composition of Pt1-xRhx, for the substitution grades x = 0.00 0.20, 0.50, 0.70, 0.80 and 1.00**

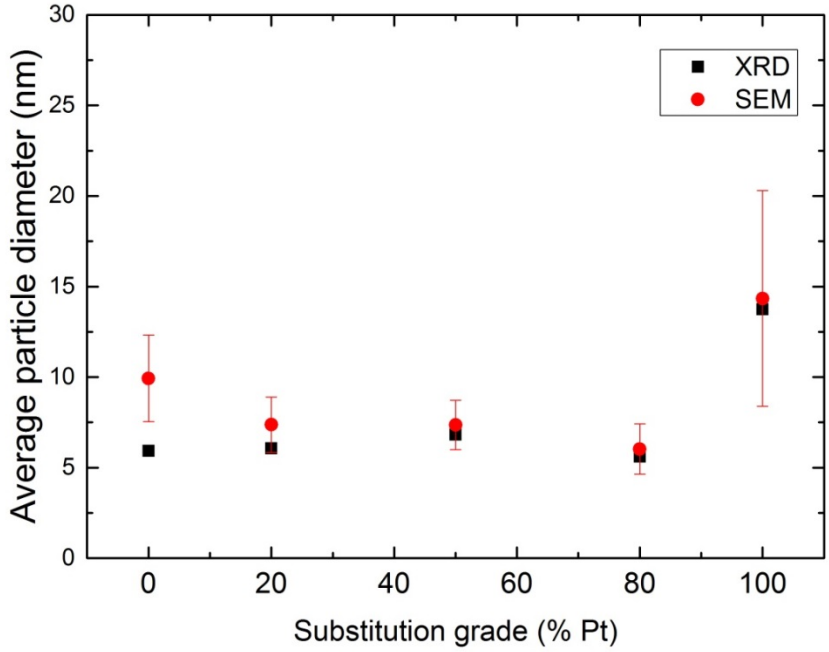


Figure 79. Average particle **Pt1-xRhx, for the substitution grades x = 0.00 0.20, 0.50, 0.80 and 1.00**

SEM images of nanoparticles of the nanoparticles with For Pt1-xRhx, x= 0.80 and x = 0.20 and the corresponding size distribution given by the SEM measurements are found in Figure 80 and 81. The histograms show a broad Gaussian distribution, and the corresponding SEM image shows the different shapes and sizes of the nanoparticles, and agglomerates of different sizes. The corresponding findings for x=0.00, x=0.50 and x=1.00 are found in Figures 40, 47 and 54, respectively.

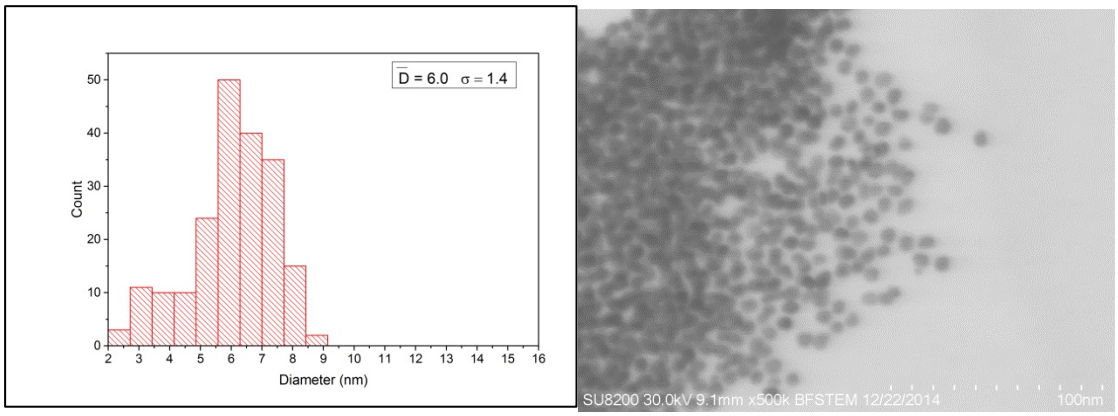


**Figure 80. The $Pt_{0.8}Rh_{0.2}$ synthesis. Left; Histogram showing size distribution of 200 measured nanoparticles, with indications of a double distribution. Average size and the standard deviation are stated in the inset. Right; BFSTEM image of the synthesis, showing large and small particles of different shapes.**

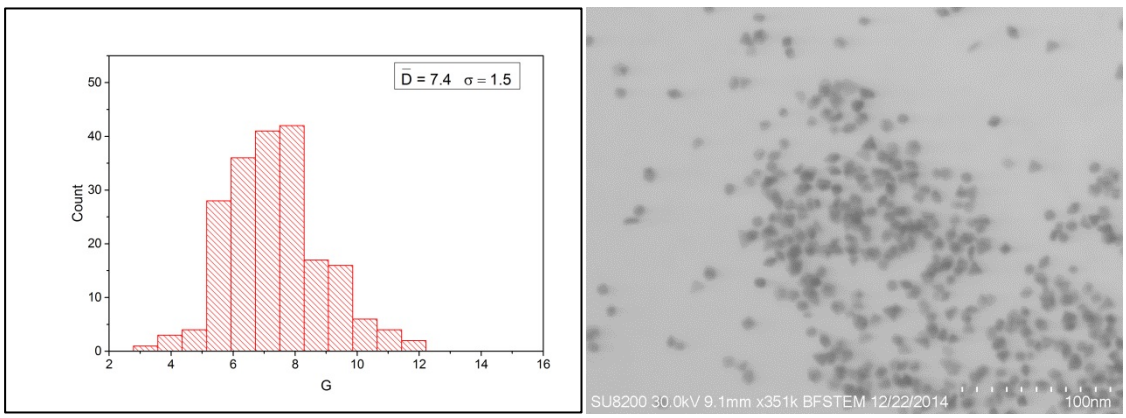


**Figure 81. The $Pt_{0.2}Rh_{0.8}$ synthesis. Left; Histogram showing size distribution of 200 measured nanoparticles, with indications of a double distribution. Average size and the standard deviation are stated in the inset. Right; BFSTEM image of the synthesis, showing large and small particles of different shapes.**

### 4.1.5 Shape analysis

The nanoparticles with composition $Pt_{1-x}Rh_x$ with x= 0.00, x=0.50 and x=1.00 were analyzed in the BFSTEM – mode, with focus on extracting the shapes found for the different compositions. Using the BFSTEM technique 3D particles are projected onto a two dimensional plane (2D); i.e. information about the third dimension may give rise to discussion. A summary of the shapes observed for Pt, $Pt_{1-x}Rh_x$ and Rh are presented in Figure 82-84. In the images, the contrast is maximized to see the contour of the particles.

**Different shapes found for the Pt nanoparticles**

In Figures 38-41 and 59-62 are the platinum nanoparticles for different reaction times and – temperatures, respectively. In these images, several shapes are observed for the Pt nanoparticles; 2D squares, hexagons and spheres where the most frequent shapes. Some nanoparticles were undefinable, and in all synthesis, some very few rods were seen. A summary of the observed shapes is given in Figure 81. The nanoparticles were usually agglomerated, and a few were seen alone on the grid. Further analysis as well as comparison with literature will be elaborated in the discussion.

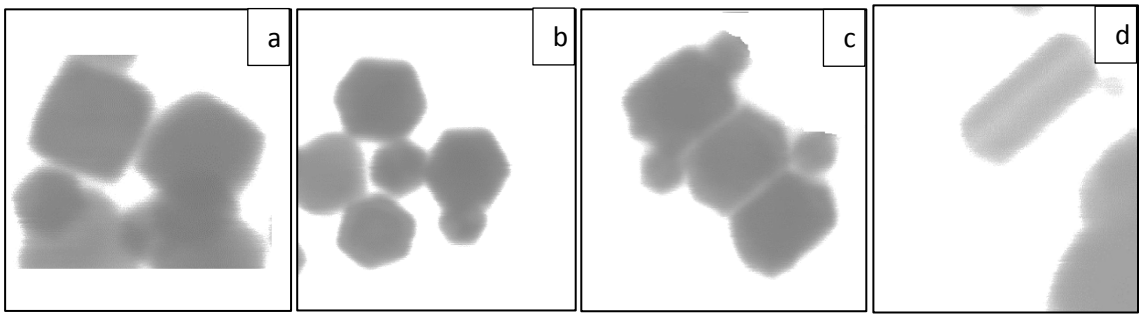


**Figure 82. BFSTM images showing different shapes found for the synthesised Pt particles; a) square particles; b) hexagonal particles; c) elongated hexagonal particles; c) rod-shaped particle.**

**Different shapes found for the Rh nanoparticles**

In Figures 52-55 and 73-76 are the rhodium nanoparticles for different reaction times and – temperatures, respectively. In these images, several shapes are observed for the Rh nanoparticles; 2D pentagons and triangles where the most frequent shapes. The different shapes found are summarized in Figure 82. Several nanoparticles were undefinable, and several seemed to have a spherical shape. However, some different shapes were also found;

in the 200 C synthesis, a very few hexagonally shaped particles were found, in the 210 C synthesis, some very few rods were seen, as well as one truncated triangle. These shapes were not representative for the Rh nanoparticles and the general shape of all nanoparticles were triangles, pentagons, spheres or undefined. The triangles had different grey-scales, indicating a thickness difference, where the darker grey particles where thicker. Some of the nanoparticles were clustered, but most particles were seen alone on the grid. In the discussion the possible 3D shapes of the Rh nanoparticles will be elaborated and compared to findings in literature.

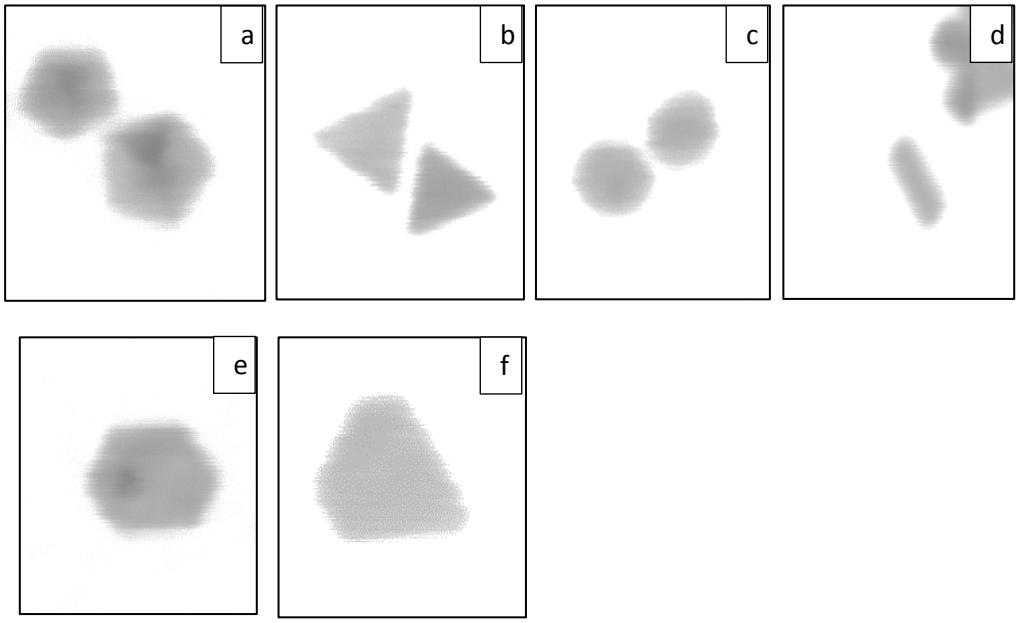


**Figure 83. BFSTM images showing different shapes found for the synthesised Rh particles; a) pentagonal particles; b) triangular particles; c) round particles; c) rod-shaped particle; e) hexagonal particle; f) truncated triangular particle**

## Different shapes found for the $Pt_{1-x}Rh_x$ bimetallic nanoparticles

BFSTEM images of the $Pt_{1-x}Rh_x$ nanoparticles are the rhodium nanoparticles for different reaction times and –temperatures are given in In Figures 45-48 and 66-69 respectively. In these images most nanoparticles were observed to have undefinable or spherical shapes. However, the shapes characteristic for the pure Rh and pure Pt were found; triangles and squares were seen inn all synthetizes. The nanoparticles were usually agglomerated, and a few were seen alone on the grid. The implication of these findings is elaborated in the discussion.

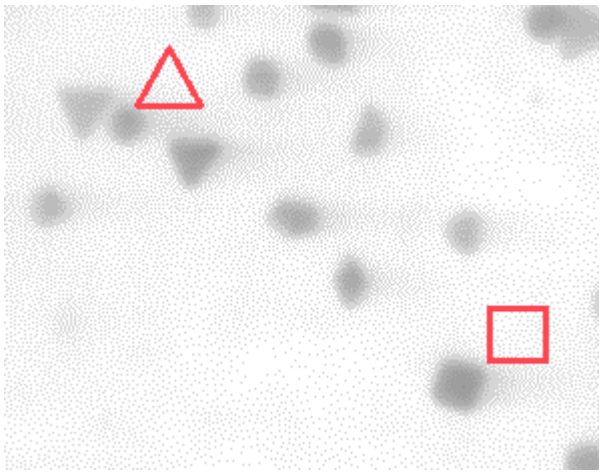

**Figure 84. . BFSTM images showing different shapes found for the synthesised $Pt_{1-x}Rh_x$ nanoparticles, showing undefinable particles together with triangular and square particles.**

## 4.2 Synthesis and characterization of 2 wt. % Pt0.70Rh0.30/Al2O3 catalysts

Nanoparticles with nominal composition $Pt_{0.70}Rh_{0.30}$ were synthesized using the 'round flask' method and the 'microwave' method, and then deposited onto two different support materials; 'boehmite' and boehmite calcinated at 900 $^{o}$C. In total four catalysts are produced, and they are given the short names Cat-PtRh-1, Cat-PtRh-2, Cat-PtRh-3 and Cat-PtRh-4, all with targeted composition 2 wt. % $Pt_{0.70}Rh_{0.30}/Al_2O_3$, see

Table 11. Flow diagrams of the individual steps for the preparation of the catalysts are reported in Figure 18 a) in section 2.2. The 2 wt. % $Pt_{0.70}Rh_{0.30}/Al_2O_3$ catalysts are a delivery into an ongoing external project, and their performance as Ostwald catalysts (step 1, see Eq. I in the Introduction) will be explored at a later stage.

**Table 11. Summary of findings for the 2 wt. % $Pt_{0.70}Rh_{0.30}/Al_2O_3$ catalysts**

| Short name | Targeted composition | Support NPs are deposited on | Free standing nanoparticles TEM and EDS | | Finished catalyst after calcination at 900 $^oC$ | | | |
|---|---|---|---|---|---|---|---|---|
| | | | | | TEM and EDS | | ICP-MS | |
| | | | Particle size (nm) | Chemical comp. | Particle size | Chemical comp. | Metal loading (wt. %) | Chemical comp. |
| The 'round flask' polyol method | | | | | | | | |
| Cat-PtRh-1 | 2 wt. % $Pt_{0.70}Rh_{0.30}/Al_2O_3$ | 'Bohemite' | 7.7 ± 1.0 | $Pt_{0.60}Rh_{0.40}$ | | [1]$Pt_{0.80}Rh_{0.20}$<br>[1]$Pt_{0.29}Rh_{0.71}$ | $Pt_{0.74}Rh_{0.26}$ | 2.5 |
| Cat-PtRh-2 | 2 wt. % $Pt_{0.70}Rh_{0.30}/Al_2O_3$ | $\gamma$-$Al_2O_3$ | 7.7 ± 1.0 | [2]$Pt_{0.60}Rh_{0.40}$ | | [1]$Pt_{0.43}Rh_{0.57}$ | $Pt_{0.74}Rh_{0.26}$ | 2.4 |
| The 'microwave' method | | | | | | | | |
| Cat-PtRh-3 | 2 wt. % $Pt_{0.70}Rh_{0.30}/Al_2O_3$ | 'Bohemite' | 12.3 ± 2.2 | $Pt_{0.75}Rh_{0.25}$ | [2]Medium<br>[2]Large<br>[2]Small | [1]$Pt_{0.73}Rh_{0.27}$<br>[1]$Pt_{0.85}Rh_{0.15}$<br>[1]$Pt_{0.68}Rh_{0.32}$ | $Pt_{0.67}Rh_{0.23}$ | 3.1 |
| Cat-PtRh-4 | 2 wt. % $Pt_{0.70}Rh_{0.30}/Al_2O_3$ | $\lambda$+$\delta$-$Al_2O_3$ | 12.3 ± 2.2 | [3]$Pt_{0.75}Rh_{0.25}$ | [2]Medium<br>[2]Large | [1]$Pt_{0.70}Rh_{0.30}$<br>[1]$Pt_{0.90}Rh_{0.10}$ | $Pt_{0.67}Rh_{0.23}$ | 2.3 |

[1]Measurement based on an individual nanoparticle. [2]Reletive sizes only.

### 4.2.1 Pre- treatment and characterization of the support material

Boehmite bought from SASOL was used as support material 'as such' or it was calcinated at 900 $^{o}$C for 10 hours prior to metal nanoparticle deposition. The purpose of using the 'boehmite' supplied by SASOL 'as such' and in a calcinated variant was to explore if the free standing nanoparticles would attach differently to the support if the support was given a heat treatment or not (removal of hydroxyl groups).

In Figure 85 are PXD patterns of the 'boehmite' bought from SASOL before and after heat treatment reported. From the powder X-ray diffractograms it was found that the as received boehmite ('boehmite') also contain some δ-$Al_2O_3$ as well as AlO(OH). After calcination for 10 hours at 900 $^{o}$C, the 'boehmite' is converted to $Al_2O_3$, with γ-$Al_2O_3$ as the main phase, and a minor fraction of δ-$Al_2O_3$. The supports are referred to as 'boehmite' or γ-alumina. A sample calcinated at 900 $^{o}$C for 24 hours was sent to SINTEF to measure its calcinated surface area by means of 1. BET measurements. It was found that the calcinated powder had a specific surface area of 63 $m^2$/g, which is acceptable with respect to acting as a support material for a metal-on-support catalyst.

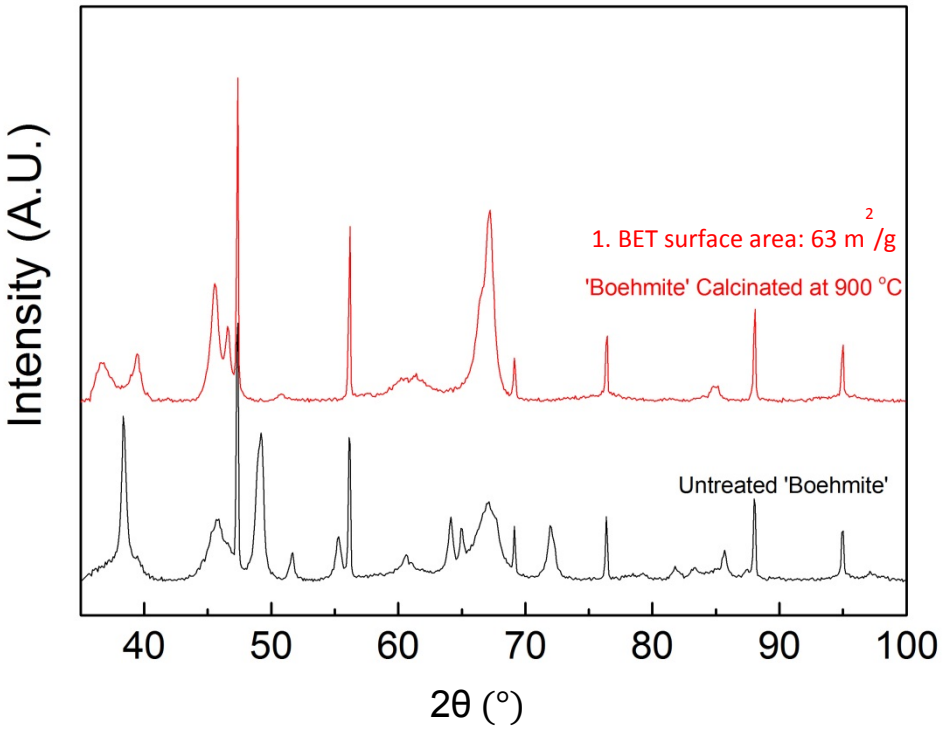


**Figure 85 Comparison of PXD patterns of the 'boehmite' before and after heat treatment.**

### 4.2.1 The ‘round flask’ polyol method – preparation of Cat-PtRh-1 and Cat-PtRh-2

In this section, the characterization of free standing nanoparticles with the nominal composition $Pt_{0.70}Rh_{0.30}$ produced through the ‘round flask’ polyol method and the different steps of the deposition of the particles onto the support materials, ‘boehmite’ and γ-alumina, is presented. The $Pt_{0.70}Rh_{0.30}$ nanoparticles were synthesized as described in details in the experimental section using 220 $^{o}$C as reaction temperature, 2 h as reaction time and quantities of Pt- and Rh metal precursors, PVP and 1,4 butanediol as listed in Table 7. Results of the obtained free standing nanoparticles and the supported particles are in the following presented in form phase content analysis (PXD), chemical composition of the metallic nanoparticles (ICP-MS, EDS), average particle size with its corresponding standard derivation (TEM). ICP-MS is performed externally.

## *Description of Cat-PtRh-1*

Figure 86 present the PXD patterns of the support material ‘boehmite’, the free-standing $Pt_{0.70}Rh_{0.30}$ nanoparticles, the nanoparticles and the support after mixing in a solution of chloroform for 2 days, and the mixture after calcination at 900 °C for 2 hours. In the powder X-ray diffractograms the different reflections originating from the nanoparticles are marked with their (hkl) values of the fcc structure and a dotted red line. The reflections belonging to the Si-reference are marked with ‘*’, and all of the remaining diffraction peaks belongs to the ‘boehmite’ or the calcinated Al2O3 variant. No other phases were detected. The diffraction peaks of the free-standing nanoparticles overlap completely or partially with the peaks of ‘boehmite’ and the calcinated variant, and due to the low loading the nanoparticles are only seen as a very small shoulder on the alumina-peaks in the diffractograms obtained after mixing and after calcination.

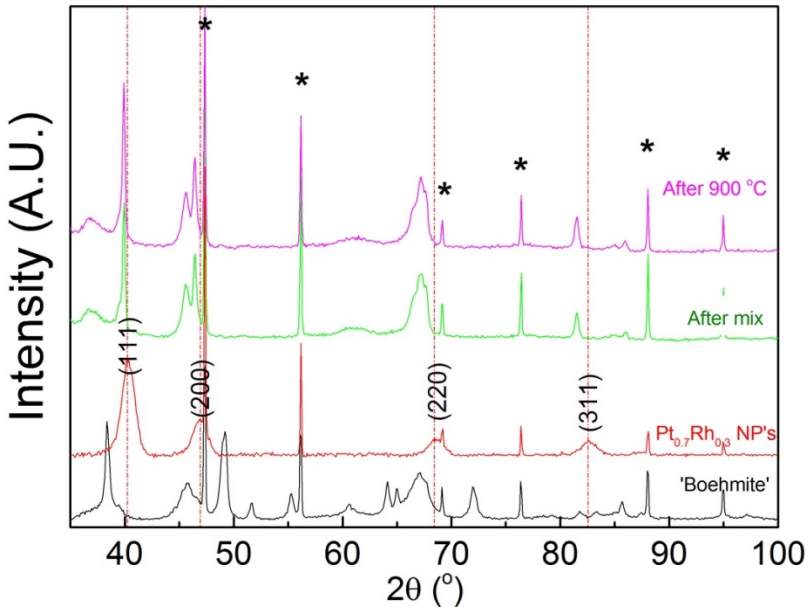


**Figure 86. PXD patterns of; (see Figure 85 for more details; i.e. mixture of boehmite with small quantities of δ-Al2O3); $Pt_{0.70}Rh_{0.30}$ nanoparticles synthesized through the 'round-flask' polyol method; the mixture of the boehmite and the $Pt_{0.70}Rh_{0.30}$ nanoparticles; the dried powder after the calcination at 900 °C for 2 h.**

In Figure 87 is a representative TEM image of the free-standing nanoparticles used for Cat-PtRh-1 and Cat-PtRh-2 reported. The average particle diameter ($\bar{D}$) was found to be 7.7 ± 1.0 nm. EDS analysis indicate that the composition is $Pt_{0.60}Rh_{0.40}$. These findings are included to

Table 11.

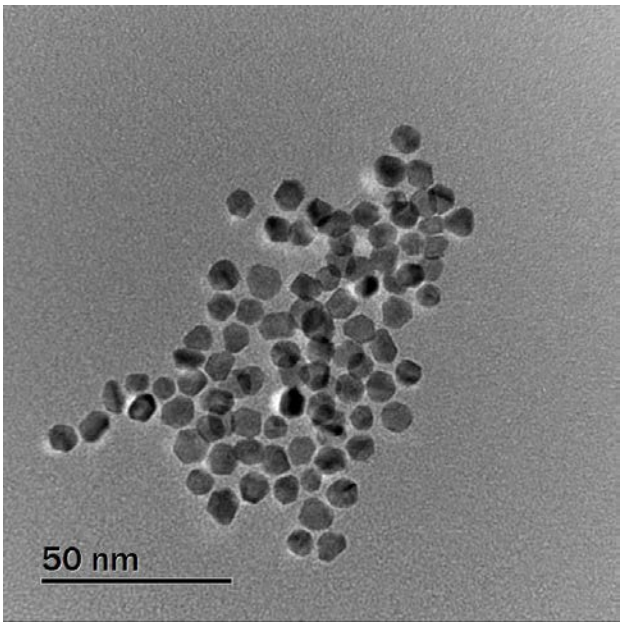


**Figure 87. TEM image of freestanding nanoparticles with target composition $Pt_{0.70}Rh_{0.30}$, synthesized using the 'round flask' polyol method. The nanoparticles have an average size of 7.7 nm ± 1nm, and EDS gives a composition of $Pt_{0.60}Rh_{0.40}$.**

In Figure 88 is a TEM image of the $Pt_{0.70}Rh_{0.30}$ nanoparticles mixed with the 'boehmite' support before the slow evaporation of the chloroform and the subsequent calcination at 900°C presented. The individual nanoparticles are visible in the center of the image, and they are clearly agglomerated. This agglomeration is a general feature of the sample and no nanoparticles were observed off the support. No attempts were done to extract the size of the deposited nanoparticles on the support.

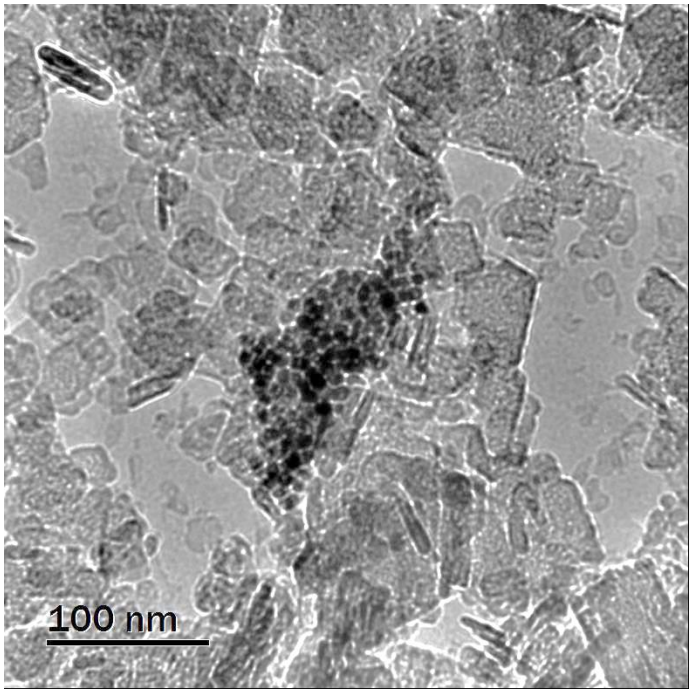


**Figure 88. TEM image of a cluster of nanoparticles on the 'boehmite' support, after mixing of the NP suspension with the suspension of boehmite.**

Also after the calcination at 900 $^{o}$C for 2 hours, the material was inspected by TEM. From the TEM investigations it becomes clear that the more or less monodisperse PtRh particles obtained it in the first step had converted into a larger size distribution, also containing 'small' and 'big' particles. Figure 4 presents TEM images of two differently sized PtRh particles on support after calcination at 900 °C. The clusters of nanoparticles have sintered and formed a larger particle. No nanoparticles were observed off the support. The composition of the large sized particle (left) found by EDS was $Pt_{0.80}Rh_{0.20}$, and the smaller sized particle (right) had a composition of $Pt_{0.29}Rh_{0.71}$. This observation, i.e. that the larger particles are enriched in Pt and the smaller in Rh after calcination at elevated temperatures is also observed by Cao et al. [67] for this type of material.

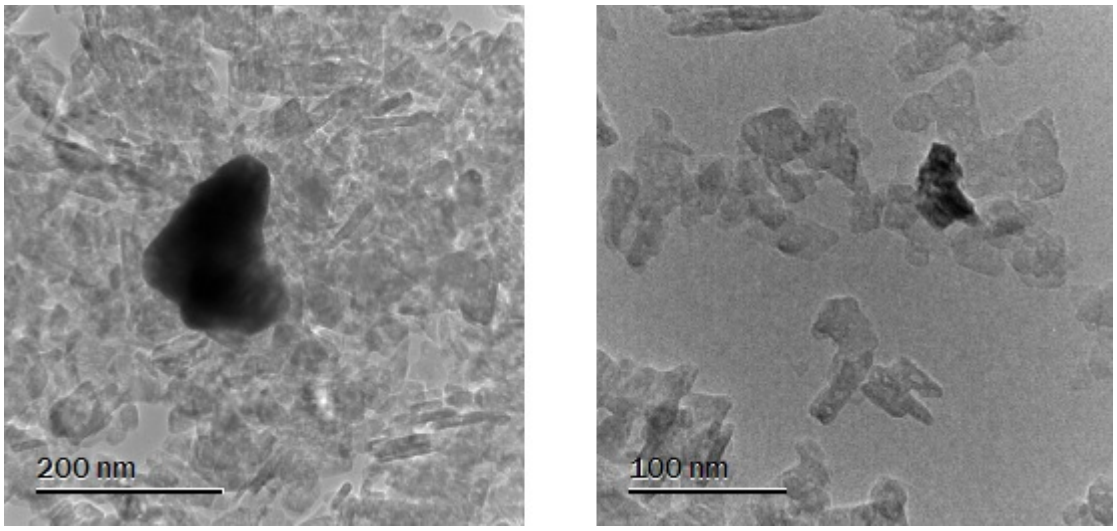


**Figure 89. The catalyst calcinated at 900 °C for 2 h, where the agglomerated nanoparticles have sintered. Left, a larger particle with composition $Pt_{0.80}Rh_{0.20}$. Right, a smaller particle with composition of $Pt_{0.29}Rh_{0.71}$.**

Further, ICP-MS of Cat-PtRh-1 gave the average metal composition of the metallic nanoparticles to be $Pt_{0.74}Rh_{0.26}$, and the metal loading is reported to be 2.5 wt. %. Main findings from the TEM investigations and ICP-MS are included in the overview table,

Table 11.

## *Description of Cat-PtRh-2*

Figure 90 presents the PXD patterns of the calcinated support material $\gamma$-alumina, the free-standing $Pt_{0.70}Rh_{0.30}$ nanoparticles, the nanoparticles and the support after mixing for 2 days in chloroform, and the mixture after calcination at 900 °C for 2 hours. The different reflections of the nanoparticles are marked with the corresponding (hkl) values of the fcc structure and a dotted red line, the reflections belonging to the Si-reference are marked with '*', and all of the remaining diffraction peaks are identified belonging to the support, which is composed primarily of γ-Al2O3 with some additional δ-Al2O3. The diffraction peaks of the free-standing nanoparticles overlap completely or partially with the peaks of the support, and due to the low targeted loading the nanoparticles (2 wt. %), are the diffraction peaks only seen as a very small shoulder on the alumina-peaks in the diffractograms obtained after mixture and after calcination.

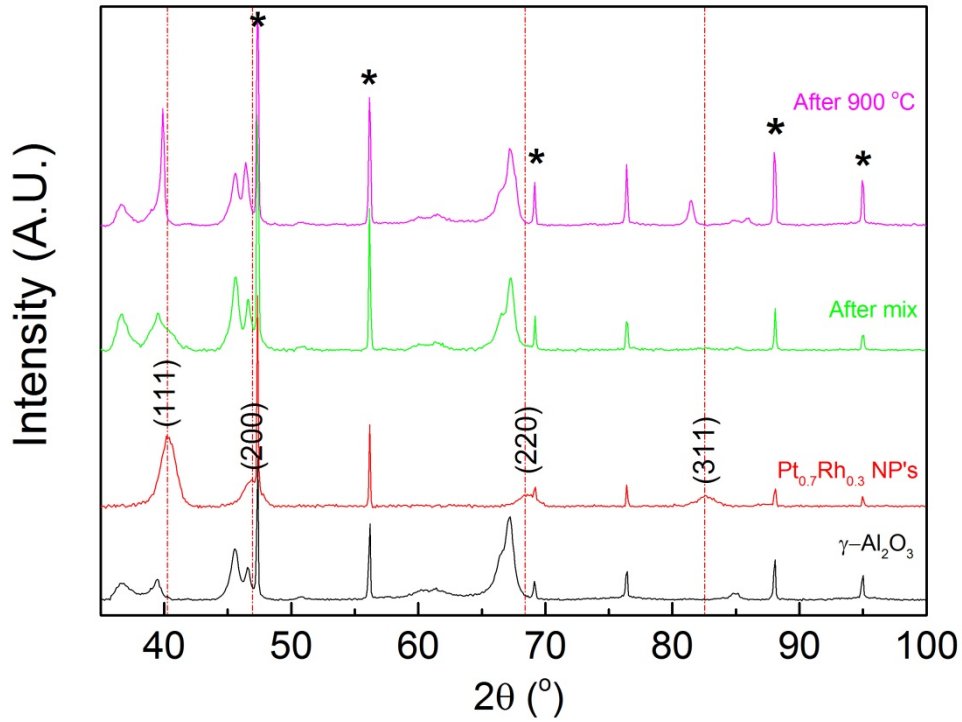


**Figure 90. XRD patterns of; 'boehmite' calcinated at 900 °C for 10 h (with the formation of γ- and δ-$Al_2O_3$; see more details in Figure 85 Comparison of PXD patterns of the 'boehmite' before and after heat treatment. ); $Pt_{0.70}Rh_{0.30}$ nanoparticles synthesized through the round flask polyol method; the mixture of the $\gamma$-alumina and the $Pt_{0.70}Rh_{0.30}$ nanoparticles; the dried powder after the calcination at 900 °C for 2 h.**

In Figure 91 is a representative TEM image of the nanoparticles after being deposited on to the alumina-support but before calcination at 900 °C presented. The individual nanoparticles are not visible because they are covered with a thick layer of alumina. All the nanoparticles in the image are found together indicating that they are agglomerated. No nanoparticles were found elsewhere than onto the alumina.

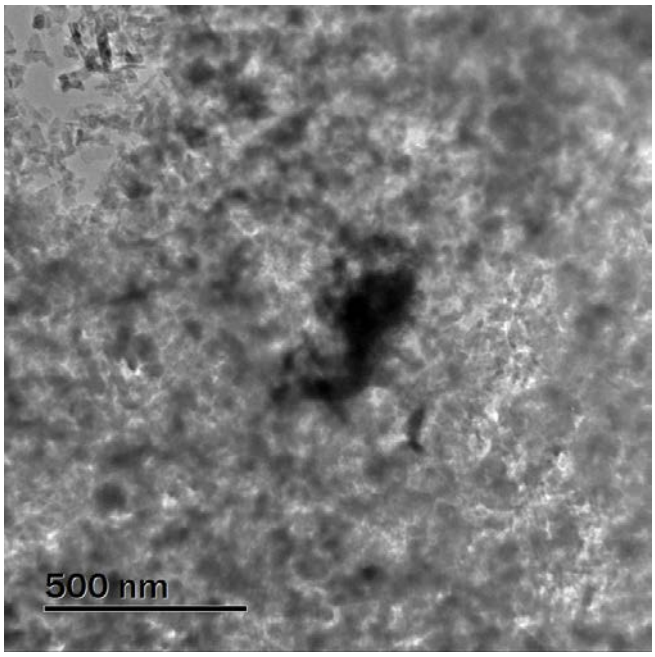


**Figure 91. TEM image of the nanoparticles on γ-alumina-support, after mixing of the NP suspension with the suspension of γ-alumina.**

In Figure 6 is a TEM image of the nanoparticles on the alumina-support after calcination at 900 °C given. From the image it is clear that the clusters of nanoparticles have sintered and formed one or more larger particles. This finding is representative for the sample after the calcination, with nanoparticle found only on the support. The composition of the sintered big particles was found by EDS to be $Pt_{0.43}Rh_{0.57}$.

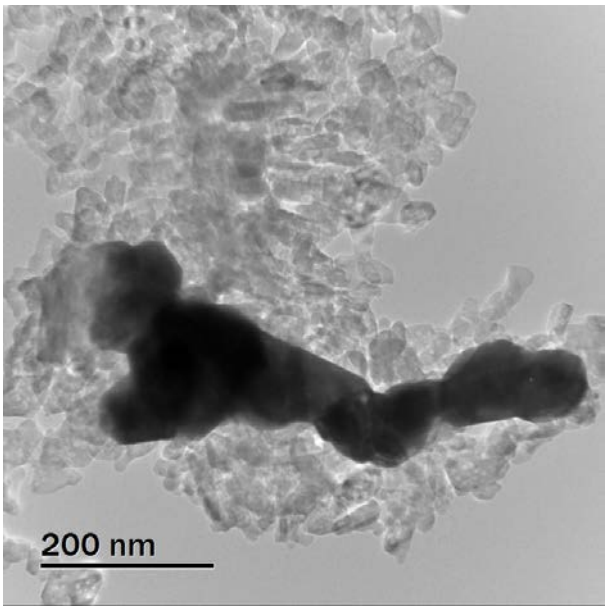


**Figure 92. The Cat-PtRh-2 catalyst calcinated at 900 °C for 2 h, where the agglomerated nanoparticles have sintered into several big particles.**

According to ICP-MS of Cat-PtRh-2, the average metal composition of the metallic nanoparticles are $Pt_{0.74}Rh_{0.26}$, and the metal loading is 2.4 wt. %. Findings from TEM and ICP-MS are included in the overview table, Table 11.

### 4.2.2 The 'microwave' method - – preparation of Cat-PtRh-3 and Cat-PtRh-4

In this section, the characterization of free standing nanoparticles of with targeted composition $Pt_{0.70}Rh_{0.30}$ using the 'microwave' method, as described in the experimental section 3.2.1, reported. In addition, the materials obtained in some of the intermediates steps required to produce the 2 wt. % $Pt_{0.70}Rh_{0.30}/Al_2O_3$ catalysts presented. Both as-received 'boehmite' and 'boehmite' calcinated for 10 h was used as support, giving rise to two catalysts denoted Cat-PtRh-3 and Cat-PtRh-4, respectively. The results of the obtained free standing nanoparticles and the supported particles are presented in form of phase content analysis, chemical composition to the metallic nanoparticles (EDS, ICP-MS) and average particle size with its corresponding standard derivation.

## *Description of Cat-PtRh-3*

In Figure 93 are the PXD patterns of the support material 'boehmite', the synthesized free-standing $Pt_{0.70}Rh_{0.30}$ nanoparticles, the nanoparticles and the support after mixing for 2 days in toluene, and the mixture after calcination at 900 °C for 2 hours. The powder X-ray reflections originating from the nanoparticles are labeled with its corresponding (hkl) values of the fcc structure and a dotted red line, the reflections belonging to the Si-reference are marked with '*', and all of the remaining diffraction peaks to belong to the 'boehmite'. By inspecting the diffractograms in Figure 8, it can be observed that the peaks of the free-standing nanoparticles

overlap completely or partially with the peaks of 'boehmite'. Due to the low targeted metal loading (2 wt. %), the nanoparticles are only seen as a very small shoulder on the alumina-peaks in the diffractograms obtained after mixture and after calcination.

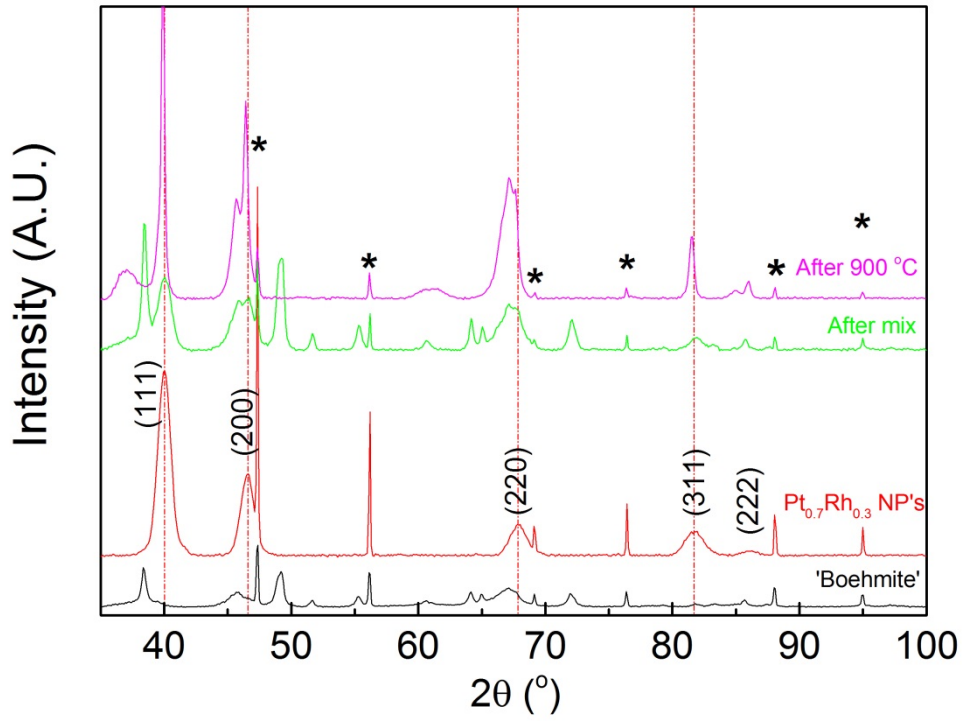


**Figure 93. XRD patterns of; (see Figure 85 Comparison of PXD patterns of the 'boehmite' before and after heat treatment. for more details; i.e. mixture of boehmite with small quantities of δ-Al2O3); $Pt_{0.70}Rh_{0.30}$ nanoparticles synthesized through the 'microwave' method; the mixture of the 'boehmite' and the $Pt_{0.70}Rh_{0.30}$ nanoparticles; the dried powder after the calcination at 900 °C for 2 h.**

A representative TEM image of the PtRh nanoparticles synthesized for the production of Cat-PtRh-3 and Cat-PtRh-4 is reported in Figure 10. The average particle size ($\bar{D}$) was found to be 12.3 ± 2.2 nm, and the chemical composition was according to EDS $Pt_{0.75}Rh_{0.25}$. The particles were found to have a stable suspension.

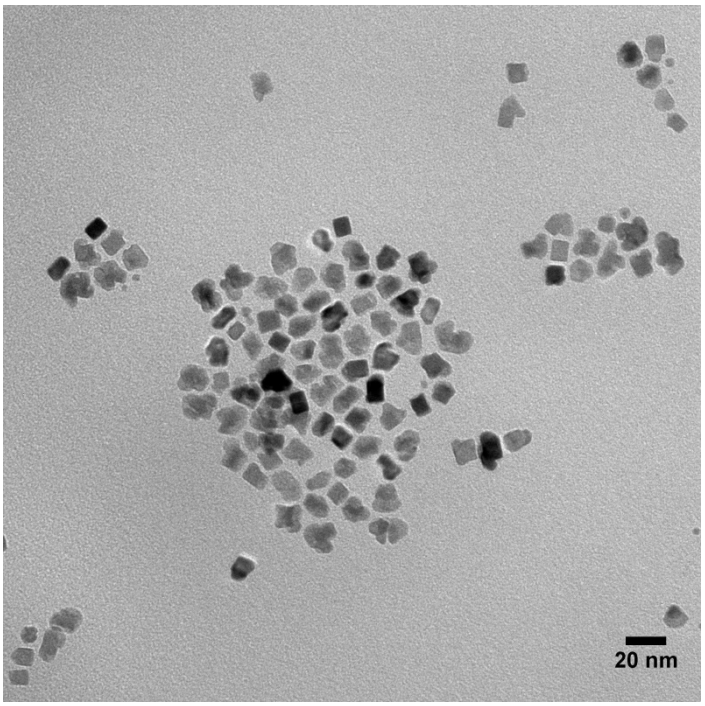


**Figure 94. TEM image of free standing nanoparticles with targeted composition $Pt_{0.70}Rh_{0.30}$ synthesized using the 'microwave' method. The nanoparticles have an average size of 12.3 nm $\pm$ 2. 2 nm, and EDS gives a composition of $Pt_{0.75}Rh_{0.25}$.**

In Figure 95 are TEM representative images of the nanoparticles deposited onto the 'boehmite' support, after mixing the suspension of the support with the suspension of the nanoparticle for 2 days. The nanoparticles are well dispersed onto the support, and no nanoparticles were observed of the support.

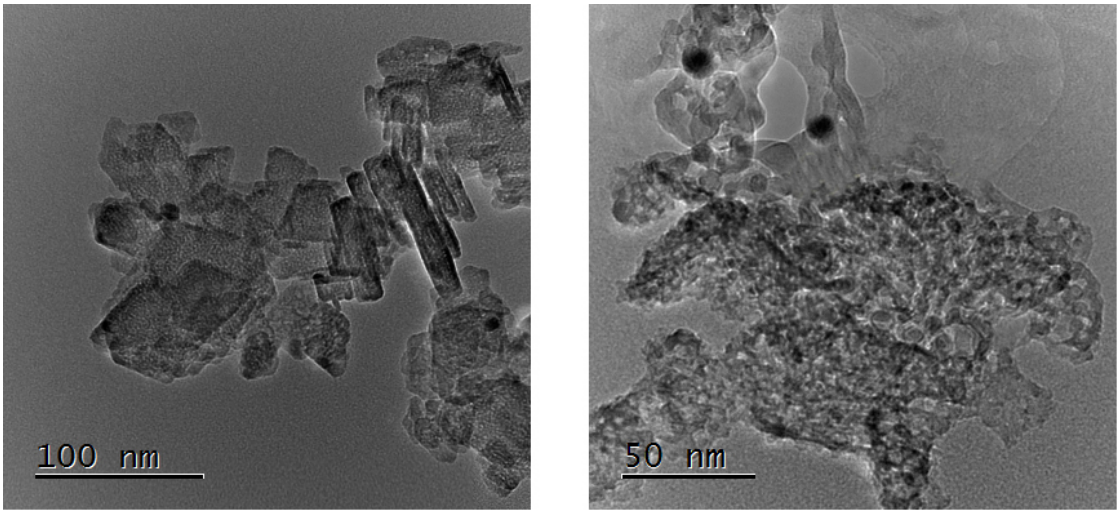


**Figure 95. The catalyst after deposition onto boehmite (before calcination), with free standing particles. The particles are well dispersed onto the support.**

After calcination of the deposited nanoparticles on the alumina at 900 oC for 2 hours it can by TEM be observed that the metallic nanoparticle size distribution is becoming very broad, with some particles being approximately 100 nm, see Figure 96. The composition of the medium sized particle in the left image has a composition $Pt_{0.73}Rh_{0.27}$. The large particle in the right

image has a composition of $Pt_{0.85}Rh_{0.15,}$ and the very small particles have composition $Pt_{0.68}Rh_{0.32.}$ These findings with larger particles having a higher composition than the smaller after heat treatment is consistent the findings in Cat-PtRh-1 as well as with literature, and will be elaborated in the Discussion.

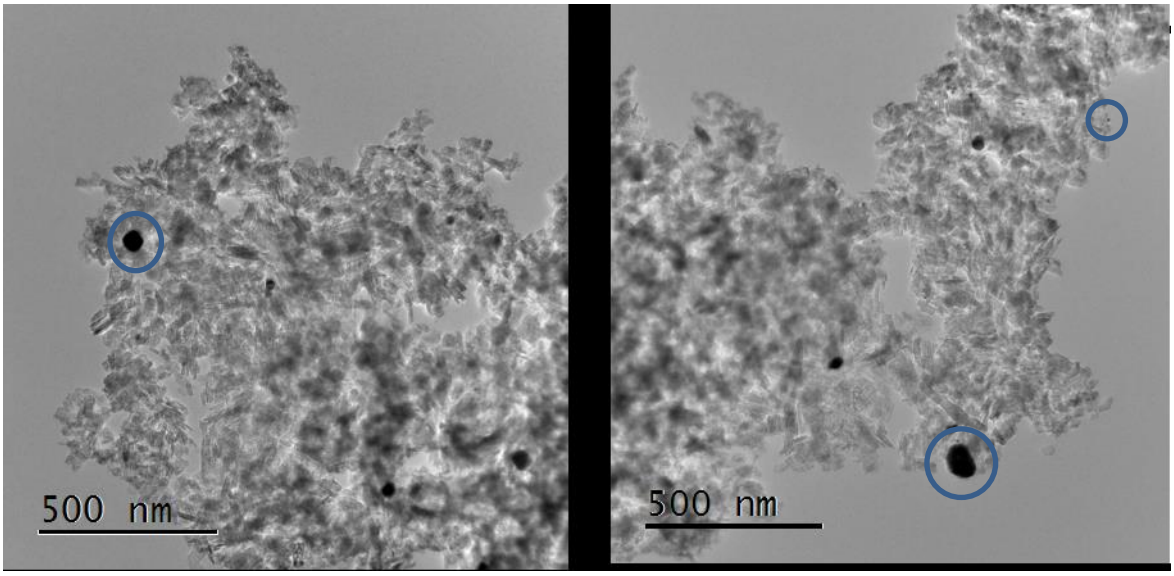


**Figure 96. The catalyst after calcination at 900 °C for 2h, with free standing particles. Left, a medium sized particle with composition $Pt_{0.73}Rh_{0.27}$. Right, a larger particle with composition of $Pt_{0.85}Rh_{0.15}$ and small particles with composition $Pt_{0.68}Rh_{0.32.}$**

ICP-MS of Cat-PtRh-3 gave that the noble metal loading is 3.1 wt. % and that the average composition of the deposited metallic nanoparticles is $Pt_{0.67}Rh_{0.23}$. Some derivation is observed with respect to targeted metal loading, but the average composition of the particles is very close to the expected value. Findings with respect to chemical composition and metal loading for this catalyst are included to the overview Table 11.

## *Description of Cat-PtRh-4*

Figure 12 presents the PXD pattern of the support material alumina, the free-standing $Pt_{0.7}Rh_{0.3}$ nanoparticles, the nanoparticles and the support after mixing for 2 days, and the mixture after calcination at 900 °C for 2 hours. The different reflections of the nanoparticles are marked with the corresponding (hkl) values of the fcc structure and a dotted red line, the reflections belonging to the Si-reference are marked with '*', and all of the remaining diffraction peaks to belong to the boehmite. The peaks of the free-standing nanoparticles overlap completely or partially with the peaks of boehmite, and due to the low loading the nanoparticles are only seen as a very small shoulder on the alumina-peaks in the diffractograms obtained after mixture and after calcination.

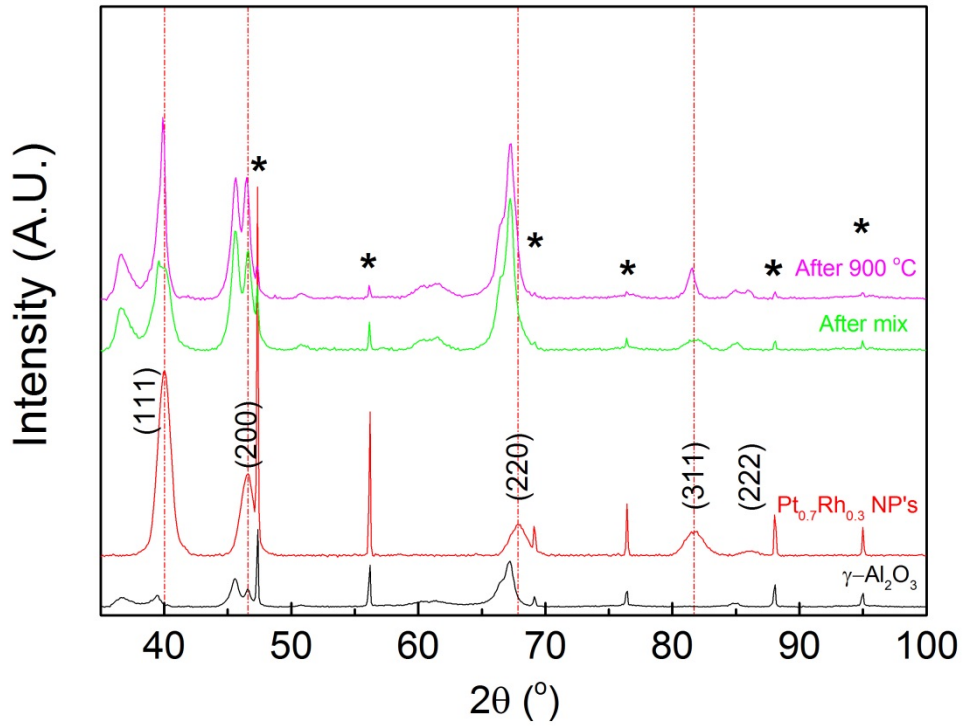


**Figure 97.**

After mixing the free standing NPs with the calcinated support in toluene for 2 days, a small sample was taken from the batch for inspection in the TEM. In Figure 98 are representative TEM images from the batch presented. The nanoparticles were not observed off the support, and they are well dispersed onto the support.

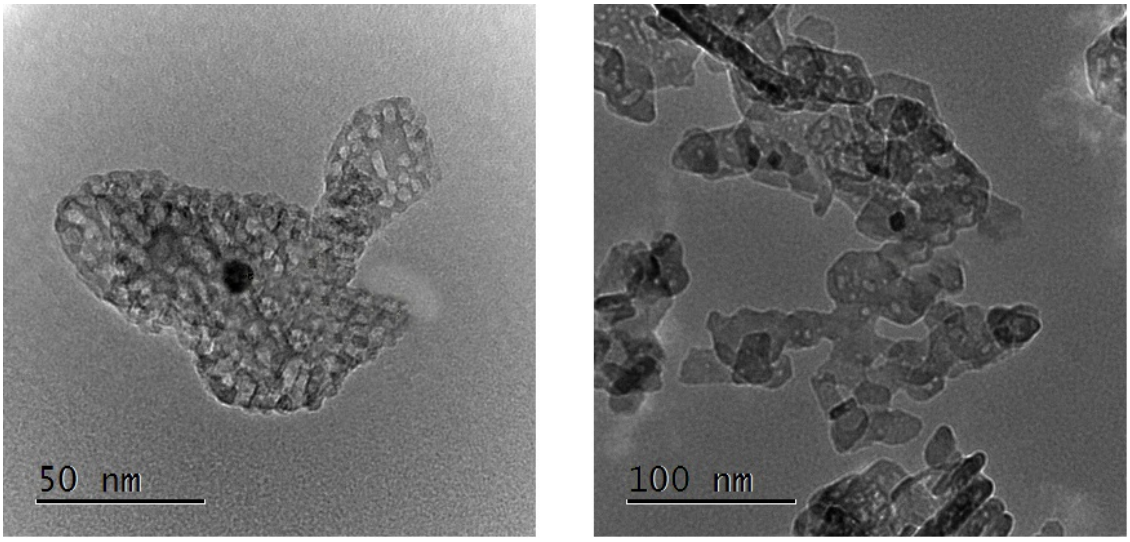


**Figure 98. The catalyst after deposition onto the alumina (before calcination), with free standing particles. The particle are well dispersed onto the support.**

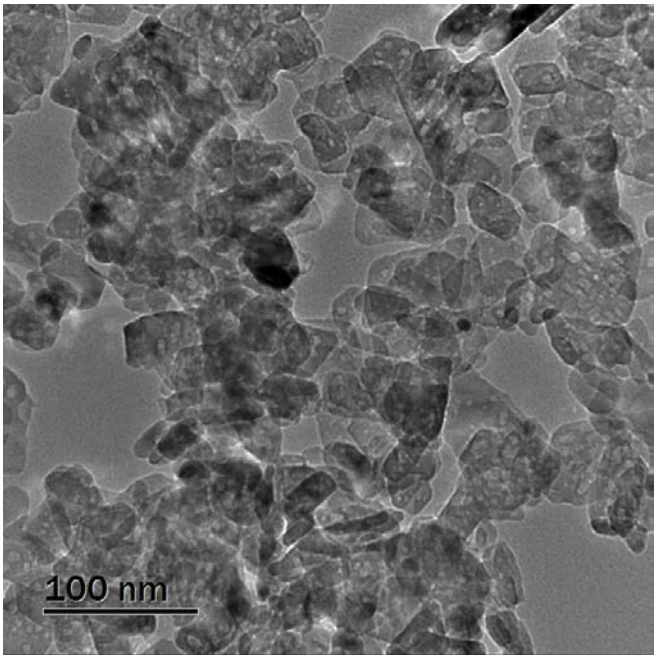


**Figure 99. Cat-PtRh-4 - the obtained catalyst after calcinated at 900 °C for 2 h. A larger particle is visible in the middle of the image, and has a composition of $Pt_{0.90}Rh_{0.10}$, whilst the smaller particle further right has a composition of $Pt_{0.70}Rh_{0.30}$.**

Further, ICP-MS of Cat-PtRh-4 gave that the metal loading on the support was 2.3 wt. %, and that the average metal composition of the metallic nanoparticles was $Pt_{0.72}Rh_{0.28}$, and Findings from TEM and ICP-MS are included in the overview Table 11.

From the overview table, Table q, it can be noted that the four synthesized catalysts, Cat-PtRh-1, Cat-PtRh-2, Cat-PtRh-3 and Cat-PtRh-4, have similarities and differences. In the discussion part of this thesis work, these observations will be elaborated in more detail. Focus will then in particular be put on:

- The different dispersions of the nanoparticles.
- The effect of the different support material
- The composition of the differently size nanoparticles after the calcination step at 900°C
-

### 4.3 Synthesis and characterization of 20 wt. % $Co_{1-x}Re_x/Al_2O_3$ catalysts

In this section, are the results obtained from the synthesis and characterization of 20 wt. % $Co_{1-x}Re_x/Al_2O_3$ catalysts with the following targeted cobalt – rhenium compositions Co,

$Co_{0.95}Re_{0.05}$, $Co_{0.90}Re_{0.10}$, and $Co_{0.85}Re_{0.15}$ presented and evaluated. All samples are prepared with the *incipient wetness* impregnation method, as described in the theory and experimental sections 2.2.4 and 3.2.3. See Table 8 in the experimental section for the definition of the short names of the produced materials.

The prepared 20 wt. %$Co_{1-x}Re_x/Al_2O_3$ catalysts will be utilized in synchrotron X-ray based studies at ESRF in Grenoble, France with the purpose to improve our understanding on the ccp/hcp stacking sequences in Co and the location of Re in the Co. However, these investigations are outside the scope of this study.

A photo of the four catalysts, Cat-CoRe-0, Cat-CoRe-5, Cat-CoRe-10 and Cat-CoRe-15, were taken after the calcination step in air for 16 hours at 320 $^oC$, see Figure 1.In Figure 1, are the different samples after calcination lined up with increasing rhenium content from left to right; Co, $Co_{0.95}Re_{0.05}$, $Co_{0.90}Re_{0.10}$, and $Co_{0.85}Re_{0.15}$. The photo shows that all samples except Cat-CoRe-0 are inhomogeneous, with some larger lumps of dark material on the top. For Cat-CoRe-5, Cat-CoRe-10 and Cat-CoRe-15 the batches contain particles with different colors. It was also observed that increasing the rhenium content a slightly lighter color of the samples.

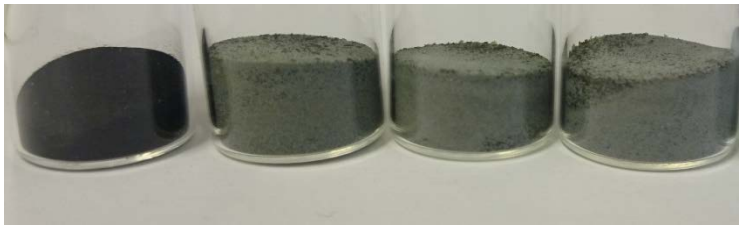

**Figure 100. Cat-CoRe-0, Cat-CoRe-5, Cat-CoRe-10 and Cat-CoRe-15after calcination at 320°C in air. Sample with lowest rhenium content to the left, and sample with the highest Rh content to the right.**

In Figure 101-101 are the XRD patterns of the support, Cat-CoRe-x (x = 0, 5, 10 and 15) after calcination at 320 °C for 16 hours, and after reduction at 390 °C for 16 hours reported. In all figures, the reflections belonging to the Si-reference are marked with '*****', the reflection belonging to the support are labeled with '**γ**' and a dotted black line, the red dotted lines indicate peaks belonging to cobalt oxide ($Co_3O_4$) and the green dotted lines mark peaks belonging to the reduced cobalt (hcp). Note that the support was measured on a holder with a single crystal Si wafer, which is why the (220) forbidden reflection from silicon is visible in the diffractograms. In the diffractograms collected for the calcinated samples (Cal-320), it can be observed that the alumina peaks overlap partially with the marked peaks of $Co_3O_4$, and they are seen as broad peaks. Note, $Co_3O_4$ reflections are not marked in the diffractograms if they overlap completely with the alumina. After reducing the materials at 390 °C in a

hydrogen containing atmosphere (Red-390), a weak unique signal from the hexagonal Co modification was identified for Cal-CoRe-0 at 2θ ~ 18.9 and 19.5, see Figure 101. No indications of the presence of metallic cobalt were observed for the other compositions in Figure 102-101 (the green dotted line indicates where the peaks should be visible). Due to the broadness of the Co-peak and the partial overlap with the alumina peak, it is not possible to determine size of the Co particles. Further, only observing small quantities of metallic cobalt in the high loading cobalt sample (Figure 101) and no in the others are in line with what Rytter *et al*.[20] report. Rytter et al. state that the reduction of Co3O4 to Co first is initiated at around ~380 - 400 °C. When the cobalt loading become smaller, as for the y = 5, 10 and 15 samples, and only a fraction of $Co_3O_4$ is reduced, the XRD signal from metallic Co will be washed out in the diffractograms.

For Cat-CoRe-5, Cat-CoRe-10 and Cat-CoRe-15 (Figure 102-101), the Re loading is increasing successively. Careful inspection of the powder X-ray diffractograms of both the calcined and reduced variants of the samples give no indication of the presence of rhenium in form of an oxide or as a metal. There can be several reasons for this; the diffraction peaks are hidden by the contributions from the other observed phases or simply that the rhenium compounds are not crystalline. The rhenium loading should be sufficient to give detectable XRD signals, if rhenium is present in crystalline phases.

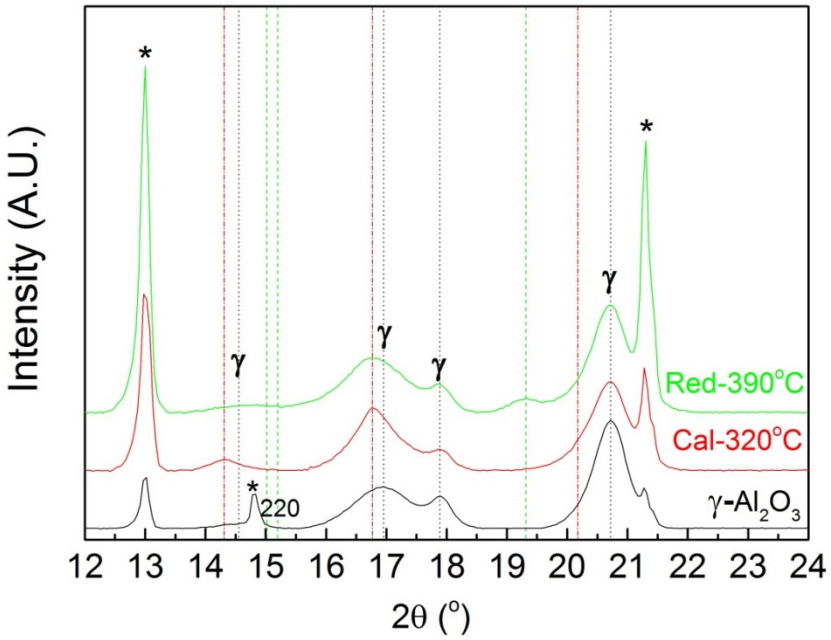


**Figure 101. PXD patterns (from Mo-instrument) of the support, the Cat-CoRe-0 after calcination at 320°C for 16 hours (Cal-320), and after reduction in a hydrogen containing atmosphere at 390°C for 16 hours (Red-390).**

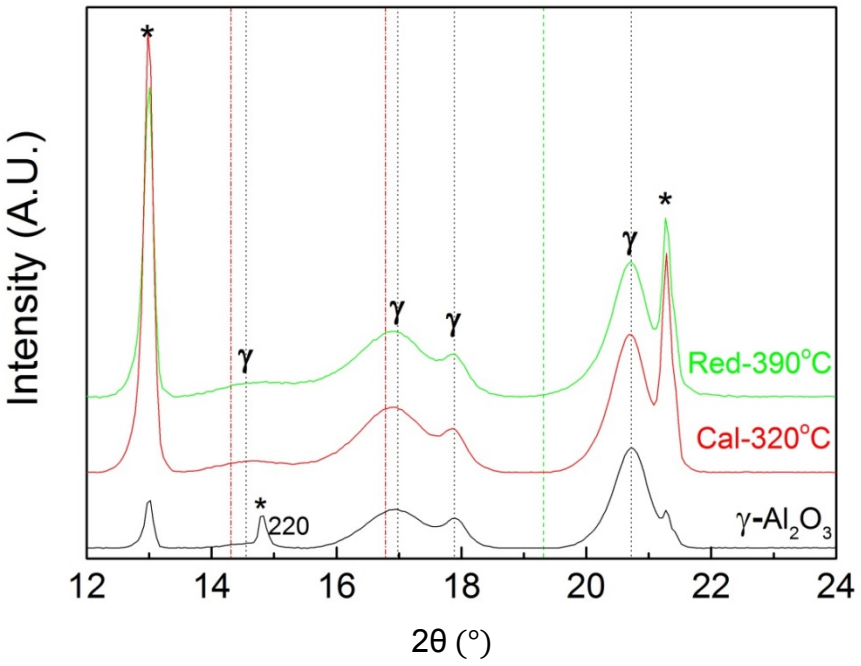


**Figure 102. Mo-PXD patterns of the support, the Cat-CoRe-5 after calcination at 320°C for 16 hours (Cal-320), and after reduction in a hydrogen containing atmosphere at 390°C for 16 hours (Red-390).**

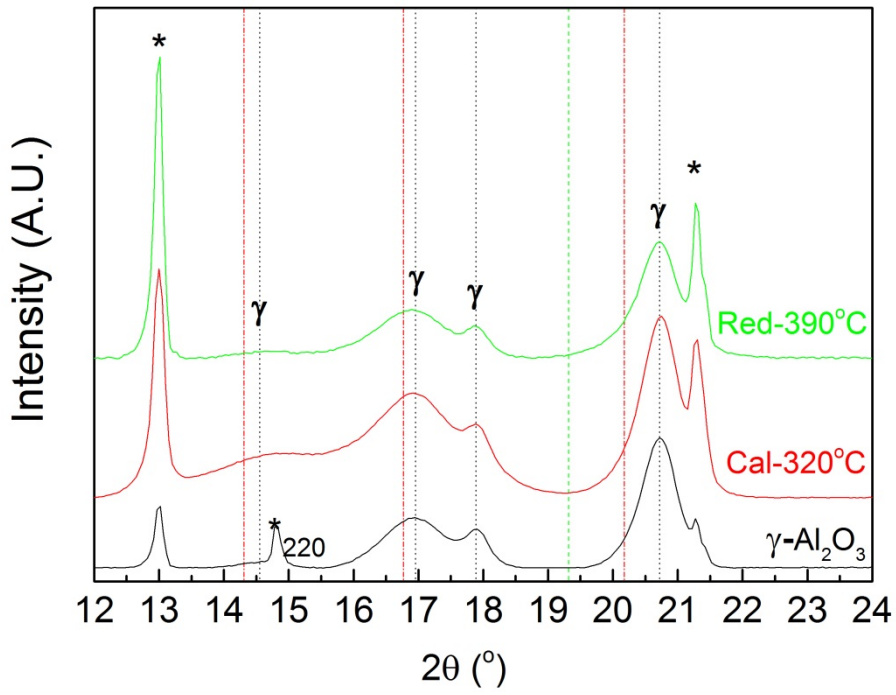


**Figure 103. Mo- PXD patterns of the support, the Cat-CoRe-10 after calcination at 320°C for 16 hours (Cal-320), and after reduction in a hydrogen containing atmosphere at 390°C for 16 hours (Red-390).**

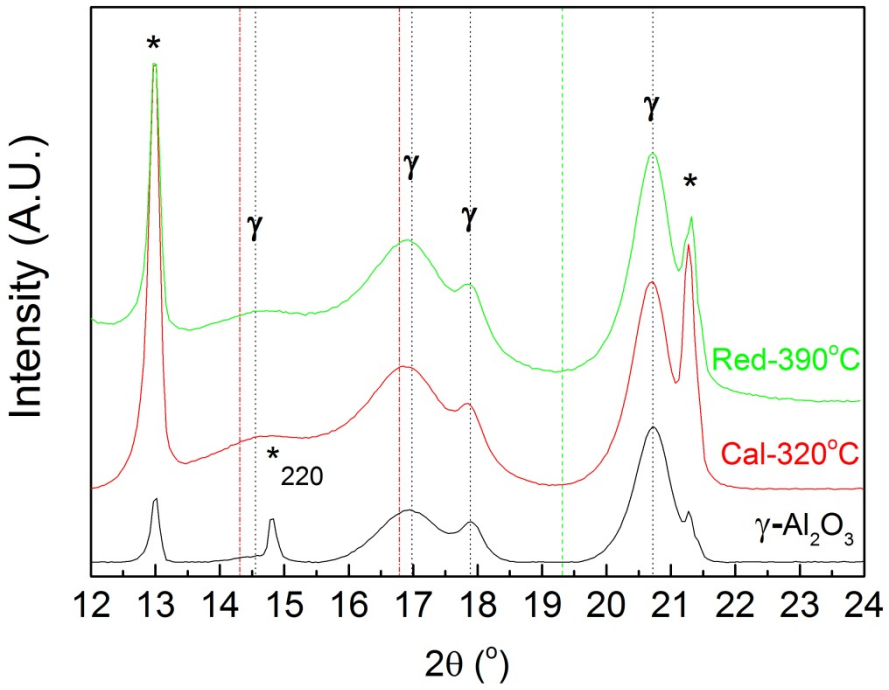


**Figure 104. Mo- PXD patterns of the support, the Cat-CoRe-15 after calcination at 320°C for 16 hours (Cal-320), and after reduction in a hydrogen containing atmosphere at 390°C for 16 hours (Red-390).**

# 5. Discussion

In this chapter, the experimental results presented in chapter 4 are compared and discussed in view of published literature. The discussion is mainly focused around the free standing $Pt_{1-x}Rh_x$ nanoparticles produced with the 'round flask' method and the 2 wt. % $Pt_{0.70}Rh_{0.30}/Al_2O_3$ catalysts.

## 5.3 Free standing $Pt_{1-x}Rh_x$ nanoparticles synthesized through the 'round flask' polyol method

**Stability of the colloidal solutions of nanoparticles:**

Generally it was concluded in the result section (3.2.1) that the $Pt_{1-x}Rh_x$ suspensions obtained in this study not are true colloidal solutions. Some few attempts were performed to optimize around different combinations of choice of washing medium and dispersing medium, with the hope that that effort should improve on the suspension stability. It was also noted that the obtained suspensions had variable stability depending on the degree of Rh substitution (x). For this reason the solutions were described as having 'unacceptable stability' or 'acceptable stability'.

In general, nanoparticles synthesised with nominal compositions x = 0.00, x = 0.20, x = 0.30 and x = 0.50 (reaction time 2 hours, reaction temperature 220 °C) were characterized as having 'unacceptable stability'. For these samples major sedimentation was observed. By inspecting the SEM images of the platinum rich members, most of the synthesized particles were observed in large agglomerates (see e.g Figures 80-81, section 4.1.1.4). Large agglomerates are too heavy to remain stable in the solvent, and will sink to the bottom. This finding is in agreement with findings reported by Park et al. [25, 26]. Park and co-workers presents TEM images of $Pt_{1-x}Rh_x$ (x = 1.00 and x=0.50) nanoparticles with significant agglomeration. The particles are produced the same way as in this study, using the same washing medium (acetone) and re-dispersed in the ethanol (which was found to give unacceptable stability in section 4.1.1). In these reports [25, 26], it is stated that the nanoparticles after this treatment were redispersed, which is assumed to mean they had stable suspensions. This finding is in conflict with our observations. It can be commented, that Pt rich nanoparticles, synthesized with 'microwave' approach using DMF as solvent and both PVP and OAm as surfactants, give free standing nanoparticles without any sign of agglomeration, according to TEM (Figure 94, section 4.2.2). Two important differences can be noted for the 'round flask' and the 'microwave' syntheses; i) 1,4-butanediol being a viscous and sticky solvent whereas DMF is neither sticky or viscous, ii) PVP is a unbranched polymer whereas OAm is linear long-chain hydrocarbon. These observations indicate that with some optimization work, it should be possible to suppress the severe agglomeration for the Pt rich nanoparticles. However, switching directly to the conditions applied in the 'microwave' approach, would most likely not work for the 'round-flask' method as DMF has a boiling point of approximately 153$^{o}$C.

The nanoparticles synthesized with the compositions x = 0.80 and x = 1.00 were evaluated to have an ‘acceptable stability’, with a black solution which remained stable for long periods of time with only some sedimentation, see Table 9 in section 3.2.1. This finding is in well agreement with the observed morphology for the Rh nanoparticles (x = 1.00). SEM imaging of pure Rh (see e.g Figures 52-55in section 4.1.2) shows that most of the nanoparticles are well dispersed. Since the Rh-suspensions were concluded to be more stable, they were also studied by DLS. However, the Rh-suspensions were according to DLS, not fully stable. DLS indicate indeed that the suspensions contain free standing nanoparticles having a hydrodynamic diameter of ~78 nm.

A general concluding comment is that production of agglomerated particles or particles not forming a stable suspension can be critical with application in mind, e.g. preparation of metal-on-support catalysts by deposition of ‘free standing’ nanoparticles.

### Variations in the a-axis with substitution grade, x, in $Pt_{1-x}Rh_x$

In Figure 105 the reported a-axis values for all syntheses of the series $Pt_{1-x}Rh_x$ carried out at the reaction temperature 220 $^{o}$C and 2 hour reaction time are presented, together with corresponding values reported by Stevanovic et al.[30] and Shen et al.[29] The a-axes reported by both Stevanovic et al.[30] and Shen et al.[29] are extracted for nanoparticles. In addition are literature values (extracted from Table 3, section 1.3) of bulk $Pt_{1-x}Rh_x$ alloys included. The data presented in Figure 105 contain much information, and in the following a discussion around some of the features will be elaborated in more detail.

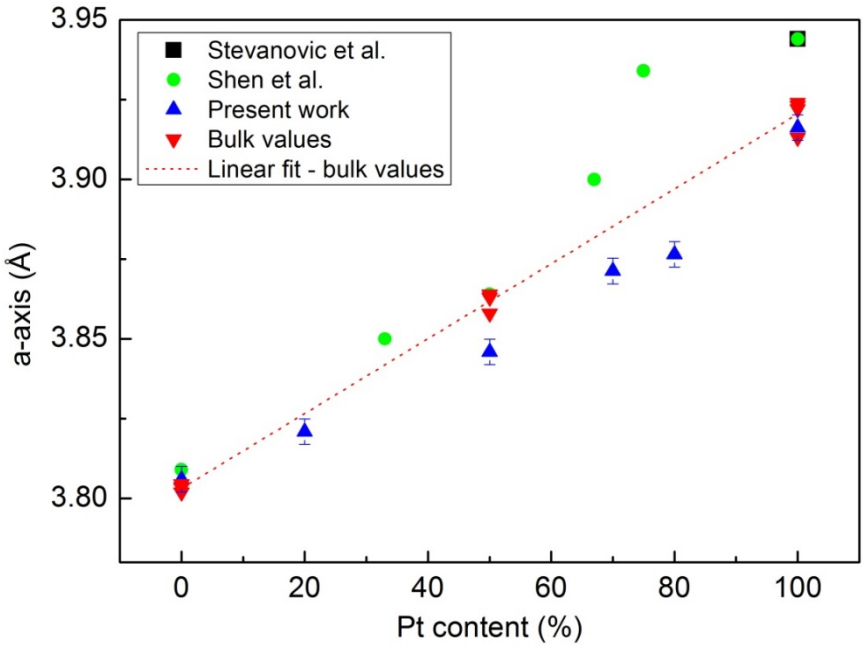


**Figure 105. Comparison of the a-axes found in the present work and literature values. References for bulk samples are reported in Table 3**

*1. Formation of a complete solid solution for $Pt_{1-x}Rh_x$ below 760 $^oC$*

By inspecting Figure 105, it is evident that the unit cell dimensions obtained in the present work are increasing with increasing platinum content throughout the entire $Pt_{1-x}Rh_x$ series. Both Pt and Rh have the fcc type structure with metallic radii's of 139 pm and 134 pm, respectively. From the observed increase in the a-axis with increasing Pt content, together with the structure and metallic radii of Rh and Pt, it can be assumed Vegard law is obeyed, meaning the obtained nanoparticles form a solid solution for the entire composition range. This finding is in line with the trend Shen et al.[29] report for their alloyed PtRh nanoparticles. Further, a similar trend is observed for bulk PtRh alloys in Figure 105.

Additional support to alloying of the nanoparticles can be found in the SEM images, since most of the nanoparticles with the nominal composition $Pt_{0.50}Rh_{0.50}$ have shapes that are not characteristic for either of the monometallic syntheses (Pt and Rh) (see e.g. Figures 66-69 in the result section. This being said, some few nanoparticles have shapes characteristic of the Rh nanoparticles (triangles) and a few also have the rectangular shapes of the Pt nanoparticles, indicating some irregularities.

The nanoparticles produced in this work and in the work by Shen et al.[29] are synthesized below 230 $^o$C (ethylene glycol used in the work by Shen et al.[29] has a boiling point of approximately 197$^o$C). According to the binary Pt-Rh phase diagram (Figure 8, section 1.3), it can be seen that binary platinum - rhodium system has a miscibility gap below 760 $^o$C, forming a two-phase with one phase being rich in Pt and the other being rich in Rh for $8 < x$ (at. % Rh) $< 92$. Since the nanoparticles in this work and in the work by Shen et al.[29] were found to have a solid solution for the entire composition range, this indicates that formation of a two-phase situation is suppressed for the nanoparticles, similar to what is found for the bulk compositions at temperatures above 760 $^o$C.

*2. Comments to scattering in reported unit cell dimensions (a-axis)*

To observe difference in reported unit cell dimensions (a-axis) between different laboratories are quite common. In order to perform a real comparison between reported values extracted from different studies, knowledge about how the unit cell dimensions are obtained becomes important. In this work a simple approach was used to extract the a-axis of the $Pt_{1-x}Rh_x$ alloys, i.e. it was calculated on basis on the max intensity of the (111) reflection after having corrected for height error from the sample holder. We did not take into account differences in shape profile of the (111) reflection between one sample to another, and the a-axis is only based on one single data point per diffractogram and not the entire diffractogram. For this reason, the uncertainty in the a-axis determination was evaluated to be within ± 0.004 Å. Unfortunately, neither Stevanovic *et al*.[30] nor Shen et al.[29] indicate the uncertainty in their reported a-axis, but both groups has used a similar approach as in this work. Assuming the uncertainty in the a-axis values reported by Stevanovic *et al*.[30]and Shen *et al*.[29] are within ± 0.004 Å, we can conclude that the difference between the values reported in this

work, and the work by Stevanovic *et al*.[30]and Shen *et al*.[29], is beyond the uncertainty for several of the compositions. It is a possibility that the real composition of the particles obtained in this work and/or the work by Shen *et al*.[29] is deviating from the nominal composition, and that this is the reason for the observed differences. But in the case of Shen *et al*.[29], the Pt rich compositions have unrealistic long a-axis, which may indicate the structure also accommodate other species than Pt and Rh.

When comparing the a-axis values reported in this work with a-axis values reported for bulk samples (see Figure 106), a good agreement with literature values and this work is found for Pt and Rh. Further, for the bulk samples, a linear expansion of the a-axis with increasing Pt content is observed. For our samples we see that the a-axis have a negative derivation for the alloys. The difference between the a-axis for our nanoparticles and the bulk samples are far beyond the uncertainty connected to choice of method in extracting the a-axis value, and it is therefore assumed to be linked to compositional differences (between Pt and Rh). In the following one possible hypothesis for why the nanoparticles reported in this study fail to reach the targeted compositions will be proposed.

*3. Hypothesis for derivation in the a-axis between alloyed $Pt_{1-x}Rh_x$ nanoparticles and bulk*

The alloyed nanoparticles synthesized in this study have a shorter a-axis than the corresponding bulk compositions, which may indicate that the nanoparticles produced in this study contain less Pt than the nominal composition given by the $Pt_{1-x}Rh_x$ formula. The reason for assuming this is that Pt is a larger atom than Rh (see above).

I should be noted that the data reported in Figure 107 represent syntheses carried out at 220 $^{o}$C and with a 2 hour reaction time. In the result section it was concluded that the a-axis of particles with the nominal composition $Pt_{0.50}Rh_{0.50}$ was expanding with increasing reaction time as well as increasing reaction temperature (see Figure 43 and Figure 64, section 4.1.2 and 4.1.3 respectively). It should be noted that the a-axis is increasing from 3.833 ± 0.004 Å to 3.851 ± 0.004 Å when increasing the reaction temperature from 190 $^{o}$C til 230 $^{o}$C, respectively. In all syntheses the supernatant was clear after the centrifugation, indicating no residues of unreduced Pt(II) (yellow) or Rh(III) (orange). The bulk value for $Pt_{0.50}Rh_{0.50}$ is reported to be in the range 3.858 – 3.864 Å. It is tempting to speculate if a slightly higher reaction temperature than 230 $^{o}$C would give an even longer a-axis. A slightly longer a-axis for the nanoparticles would then match literature values for the bulk analogue.

With basis in these observations the following alloying mechanism will be proposed:

At the onset of nucleation during synthesis of the alloyed $Pt_{1-x}Rh_x$ nanoparticles a nucleus is formed which is enriched in rhodium relative to the nominal composition (element with smallest metallic radii), and at the end of the precipitation process small clusters or a thin shell of the remaining Pt is precipitated. A homogenisation of the heterogeneously formed particles is then subsequently starting via diffusion, which is facilitated by increasing the reaction time and or the reaction temperature. The remainder of the shell would probably be too thin to be detected as pure Pt in the PXD patterns. To verify this hypothesis, knowledge on what of the two elements that precipitate easiest under the applied reaction conditions is required.

Unpublished results from our research group is supporting this theory, however, in that specific study the a-axis was decreasing with increasing reaction time, an in addition rhodium was found to be the slowest of Pt and Rh to precipitate.[32] Further, careful TEM-STEM-EDS investigations are also tools that can be called for in order to document cluster and or film formation that is enriched in Pt at early stages in the process (see Prospectives).

For the $Pt_{0.5}Rh_{0.5}$ nanoparticles the a-axis was found to increase slightly with increasing reaction time and increasing reaction temperature, indicating that less rhodium was implemented in the structure. In Figure 63, which compares the diffractograms of different reaction temperatures of the $Pt_{0.5}Rh_{0.5}$ nanoparticles, the diffractogram for the 220 $°C$ (2h) synthesis is shifted slightly to the right with respect to the other reaction temperatures, which should lead to a smaller a-axis. However, the opposite was found in the a-axis with an increase with respect to the 190$°C$, 200$°C$ and 210 $°C$ syntheses. The same is seen for the diffractograms for various reaction times (Figure 42), where the 2h (220$°C$) is shifted slightly to the right, whiles the calculated a-axis is larger than the others. The reason for this is not understood, and the same results were found after several repetitions of calculating a-axes and stacking of diffractograms. For the Rh nanoparticles an unexpected deviation in a-axis was found for the 2 h reaction time (see Figure 50), where the 2h reaction time corresponding well to literature values, and the others are slightly higher. The reason for this deviation could be that the poor intensities found in the syntheses with different reaction times of the Rh nanoparticles, and that this causes an additional uncertainty with respect to the maximum intensity and the shape of the peaks.

**3D shapes of the nanoparticles and influence of the size analysis**

In the synthesis of free standing nanoparticles, several shapes were found to be characteristic for the $Pt_{1-x}Rh_x$ nanoparticles where x= 0.00, and x=1.00 (see Figure 82-78 in section 4.1.5). Using the STEM technique 3D particles are projected onto a two dimensional plane (2D), giving rise to some discussion about the 3D structure of the particles. In the following comparing the shape and contrast of the particles with possible polygonal shapes in light of literature will be presented.

***Platinum nanoparticles***

In Figure 82 (see section 4.1.5) several different shapes are found for the platinum nanoparticles, and in the following an analysis of possible 3D structure of the particles will be given in. From the high and even contrast of the square Pt nanoparticles in Figure 82a), together with their sharp edges, there is an indication that there this is a 3 dimensional (3D) shape of a cube. Octahedral shape could also have been a possibility; however the sharp edges exclude this option. The rectangular particles seem to have the length of the sides consist with the particles being close to perfectly cubic, rather than orthorhombic or monoclinic. Cubic shapes for the platinum nanoparticles have also been reported in literature,[24, 49] and it therefore seems like the most plausible shape for the Pt nanoparticles synthesised for the Pt nanoparticles.

The hexagonal Pt nanoparticles vary in shape; some seem to be perfectly hexagonal, others have some elongated sides. The hexagonal nanoparticles that have 3 long and 3 shorter edges

and equal truncated cuboctahedrons, which has been reported for Pt NP's.[49] The perfectly hexagonal particles could arise from hexagonal plates or prisms, icosahedrons, octahedrons, or truncated cuboctahedrons. The sharp edges and even contrast of the nanoparticles make the icosahedron and octahedron less plausible, and the large contrast make it unlikely that the particles are thin plates. This leaves the hexagonal prisms and cubeoctahedron as the most likely shapes. However, from literature,[49] nanoparticles with PVP often make seeds of Wulff polyhedrons, which grow to be octahedrons, cuboctahedrons and cubes. Also, in Figure 11 b in section 2.1, the perfect hexagonal shape is reported as truncated cuboctahedral, and it is therefore more likely that this is the 3D shape of the hexagons. The hexagonal particles that have 2 long axes and 4 short could be the result of anisotropic growth.

For the platinum nanoparticles a double size distribution was found (see Figure 38-39 section 4.1.2). More information on statistics on the size versus shape could have been done to determine if the double distribution of the platinum nanoparticles is partially caused by different shapes having different sizes, however there is a clear presence of smaller nanoparticles (see e.g. Figure 38), which are the apparent main cause of the double distribution.

***Rhodium nanoparticles***

The triangles found for the rhodium nanoparticles in reported in 50-53, section 4.1.2 have different contrasts, indicating different thicknesses. The lighter grey triangular particles are thinner (because we are looking at transmission mode) and have an even contrast, and it is therefore probable they are thin triangular plates. Triangular plates have been reported to arise from twinned seeds.[49] Some triangles were darker grey and had uneven contrast, and could therefore be tetrahedrons (or possibly octahedrons). In some syntheses hexagonal plates were also found, and according to theory this could also be due to the formation of twin-defects.[49] The pentagons found in the Rh syntheses have a contrast gradient with higher contrast in the centre of the particles, and are most likely Rh dodecahedrons. This could arise from twinned seeds.[49] Twinned seeds are also the explanation for the triangle and hexagonal plates. Statistics on the occurrence of different shapes, as well as the sizes of the different shapes could be done to see if the size distribution varied with shape. (see Prospectives)

**Effect of reaction time and reaction temperature on particle size and particle size distribution**

From Figure 44, Figure 51, Figure 65 and Figure 72 (section 4.1.1 and 4.1.2) it was observed that the particles size is relatively unaffected by reaction time and temperature for the nanoparticles with composition $Pt_{1-x}Rh_x$ nanoparticles where x= 0.50, and x=1.00. From the laMer theory (Figure 9 section 2.1), the nucleation should occur as soon as the conditions are right (the reaction temperature is sufficient for reduction). The formation of seeds decreases the concentration below the supersaturation point, and then growth occurs until the precursors are 'spent'. It seems that changes in temperature do not affect the nucleation or growth of the particles for these compositions (x= 0.50 and x=1.00) within the timeframe of 2h, and that no other events occur influencing the particle size after the growth step. Also, if no additional processes occur once the growth is finished, changes in reaction time after a minimum will

not affect the particle sizes. It seems likely in light of our findings that the growth process is finished before 0.5 hours (the minimum time in this work) for the reaction temperature of 220°C.

For the platinum nanoparticles, both the average size ($\overline{D}$) and standard deviation (σ) found by SEM investigations are clearly increasing with increased reaction time and temperature (see Figure 37 and Figure 58 in section 4.1.2 and 4.1.3). It seems likely that unless nucleation occurs continuously during the reaction time, this increased standard deviation (σ) and average mean size ($\overline{D}$) is caused by Ostwald ripening. The Ostwald ripening is then continuous with time, and increases with increased reaction temperature.

### 5.4 Effect of synthesis procedure for Cat-PtRh-1, Cat-PtRh, Cat-PtRh-3 and Cat-PtRh-4

In the present study four catalysts were made based on the principle of depositing synthesized nanoparticles directly onto a support material. Two variables were explored; effect of choice of synthesis route ('polyol route' versus 'microwave route') and possible effect of performing a pre-treatment of the support material or not ('bohemite' and '$\gamma$-$Al_2O_3$'). Short names Cat-PtRh-1 ('polyol route' + 'bohemite'), Cat-PtRh-2 ('polyol route' + $\gamma$-$Al_2O_3$), Cat-PtRh-3 ('microwave route' + 'bohemite') and Cat-PtRh-4 ('microwave route' + '$\gamma$-$Al_2O_3$') were introduced.

The free standing nanoparticles used in the preparation of Cat-PtRh-1 and Cat-PtRh-2 were found to be present in form of large agglomerates prior to deposition, see e.g. Figure 87 in section 4.2.2. The agglomeration of these particles is also discussed in section 4.1.1. The nanoparticles were observed to be poorly dispersed on the support, and it is likely that this is caused by the particles being agglomerated prior to deposition. This is also assumed to be the reason why they also sinter to large particles in the μm range during the calcination step at 900°C. The 'round flask' polyol method need optimization to produce well dispersed nanoparticles. On the other side, the free standing nanoparticles deposited on Cat-PtRh-3 and Cat-PtRh-4 are well dispersed on the support. They were originally also well dispersed in the suspension prior to the deposition step. In addition, they do not tend to agglomerate during the deposition step on none of the two variants of the support. As the particles are well dispersed on the support they apparently withstand the calcination at 900$^{o}$C quite well maintaining sizes in the nm range.

For metal-on-support catalysts it is normally desirably to have the metal particles well dispersed on the support to maximize the metallic surface area. The well dispersed nanoparticles of the Cat-PtRh-3 and Cat-PtRh-4 have a higher accessible metallic surface area than the agglomerated particles of the Cat-PtRh-1 and Cat-PtRh-2, and they also stay relatively small during the calcination step compared to the agglomerated particles that sinter. Therefore, for catalytic purposes, Cat-PtRh-3 and Cat-PtRh-4 is expected to be more suitable than the Cat-PtRh-1 and Cat-PtRh-2. Catalytic testing for the Ostwald reaction will reveal which procedure is more effective with respect to nanoparticle synthesis, and choice of support, and will give the direction for further optimization.

For Cat-PtRh-3 and Cat-PtRh-4, no difference was found for the two support materials ('bohemite' and $\gamma$-$Al_2O_3$) with respect to metal dispersion. This implies that number of hydroxyl groups on the support at the point the metallic nanoparticles are anchored on the support is not critical. The nanoparticles are spread well onto the support of both support materials, and no nanoparticles were found not to be attached to the support in either catalyst, indicating that the nanoparticles attach well onto the support.

### *Composition of the catalysts*

For Cat-PtRh-3 and Cat-PtRh-4 it can be seen in Table 11 that the Pt content of the calcined catalysts was found to be higher for larger particles than for smaller particles. This can be explained by transport of $PtO_2$ in the gas phase were the platinum leaves the structure of some nanoparticles as $PtO_2$(g) and is then deposited onto other particles as Pt, giving small particles with low Pt content and large particles with higher Pt content.[68] Similar observations are also observed by Cao *et al*.[67]

The average composition given by EDS for the final catalyst of Cat-PtRh-1 is $Pt_{0.69}Rh_{0.31}$, whereas the composition given by ICP-MS is $Pt_{0.74}Rh_{0.26}$. This difference is most likely due to statistics, where the results from ICP-MS represent the average of a larger quantity of the material, and the EDS measurement is from two very small areas of the sample. The ICP-MS is therefore trusted to be the overall composition of the samples. However, the EDS give an indication of how homogeneous the sample is, and with the presence of large, Pt-rich particles and small Rh-rich particles, the sample is quite heterogeneous. The same inhomogeneities are found in Cat-PtRh-3 and Cat-PtRh-4. For the Cat-PtRh-2 only one EDS measurement was done, and this result is not likely to be representative of the sample. However, it is reasonable to believe the same trend is applicable for this catalyst.

All four catalysts were produced to give a composition of the metallic nanoparticles to be Pt0.70Rh0.30. According to ICP-MS, Cat-PtRh-1 and Cat-PtRh-2 has the average composition $P_{t0.74}Rh_{0.26}$ whereas EDS indicate $P_{t0.60}Rh_{0.40}$ . For Cat-PtRh-3 and Cat-PtRh-4 the corresponding values for ICP-MS and EDS are $P_{t0.67}Rh_{0.33}$ and $P_{t0.75}Rh_{0.25}$, respectively. There are some scattering in the reported data, however the measurements are not performed on the same stage in the process. Based on this it is difficult to conclude if the average compositions of the metallic particles are changing during the preparation step. As ICP-MS give the average composition of a larger fraction of the sample, it would have been very useful to have had ICP-MS data for the free standing particles.

The total metal loading of all the catalysts are according to ICP-MS higher than the target loading. The reason for this is not understood. It can be pointed out that the metal loading is higher for the catalysts deposited onto boehmite than the ones deposited onto alumina. This difference could partially be due to water leaving the boehmite structure during calcination.

In sum: The good dispersion found in Cat-PtRh-3 and Cat-PtRh-4 after calcination is promising with respect to catalyst synthesized by deposition of free-standing nanoparticles,

and this technique serves as a good method to obtain metal-on-support catalyst. However, the transport of $PtO_2$ found for the PtRh-system in this work is a problem with respect to the stability of the particles.

### 5.5 20 wt. % $Co_{1-x}Re_x/Al_2O_3$ catalysts

A general feature of the Cat-CoRe-x (x = 0, 5, 10 and 15) catalysts obtained in this study was that the PXD patterns (section 4.3) indicate little or no presence of metallic cobalt and Re containing phases after calcination and activation at 390 $^oC$. With respect to cobalt, this is in line with findings reported by Rytter et al.[20] According to Rytter et al., metallic cobalt is first observed by PXD at around 380-400 °C in a hydrogen containing atmosphere. For this reason it should be anticipated that cobalt still is mainly in form of $Co_3O_4$ and CoO, as the sequential reduction steps are $Co_3O_4$ → CoO → Co. However the peaks of CoO were not observed.
Lack of PXD signal from rhenium in the samples is not due to a too low Re loading, as the detection limit is normally 1-2 %. Instead it must be connected to that rhenium is not in a crystalline form or that its diffraction peaks are hidden in the background. Here, no comparison with Rytter et al.[20] can be done, as the samples investigated by them have a much lower Re loading.
Overall, it can be stated that the catalysts are as expected with respect to cobalt containing phases, but slightly surprising relative to rhenium and in what form rhenium is present in the samples. The samples will be subjected to in-situ synchrotron experiments at ESRF, Grenoble in various atmospheres. This will likely provide some more answers. However that effort is outside the definition of this project.

From the PXD-patterns in Figure 101 (section4.3) it was found that the Cat-CoRe-0 contained metallic cobalt. The reason for the missing cobalt peaks in Cat-CoRe-5, Cat-CoRe-10 and Cat-CoRe-15 is not understood, however it could be due to the lower loading of cobalt where only a fraction of $Co_3O_4$ is reduced, which is in line with what Rytter *et al*.[20] report. They also state that there reduction of the $Co_3O_4$ to Co first is initiated at around ~380 - 400 ℃, and it is possible that 390 ℃ was to low for the sample containing smaller amounts of cobalt. However since the rhenium is known to promote the reduction of cobalt oxide, the reason for this is not understood. Error in experimental procedure/equipment is not excluded.

# 6. Conclusions

A method to synthesize nanoparticles with composition $Pt_{1-x}Rh_x$ through the 'polyol route' was established, and the synthesized nanoparticles were analyzed with respect to size and lattice parameters as a function of reaction time, -temperature and composition. The size of the particles with composition x=1.00 and 0.50 were found to have sizes of (∼7 nm) independent of reaction time and -temperatures, whilst both the size and size distribution of particles with composition x = 0.00 were found to increasing with increasing time and temperature (∼9 -16 nm). This was explained by Ostwald ripening facilitated by longer reaction times and higher reaction temperatures. With respect to composition, the size was found to be invariant for the compositions x=0.20, x = 0.50, x = 0.80 and x= 1.00., and higher for the composition x = 0.00

The lattice parameters of the nanoparticles synthesized with composition $Pt_{1-x}Rh_x$ x=0.00 and x=1.00 were found to be independent of reaction time and reaction temperature. The lattice parameters of $Pt_{1-x}Rh_x$ nanoparticles with x=0.50 were found to increase with increasing reaction time and –temperature. With basis in this observation a hypostasis for the alloying mechanism of the $Pt_{0.50}Rh_{0.50}$ was suggested, where nuclei rich in rhodium are formed initially, followed by the formation of a thin shell formation of Pt around the nuclei and subsequent diffusion facilitated by increased reaction time and temperature. The remaining shell is assumed to be too thin for detection as a pure Pt phase in PXD. The lattice parameters with respect to composition were found to increase gradually with increasing Pt content, corresponding to literature and evident of the formation of complete solid solution.

Characteristic shapes were found for the Pt (cubes, truncated cuboctahedrons) and Rh (triangular plates and dodecahedrons) particles, and for the bimetallic $Pt_{1-x}Rh_x$ particles mostly undefinable shapes characteristic for neither Pt nor Rh were observed, supporting the formation of solid solutions.

Catalysts with 2 wt. % $Pt_{0.70}Rh_{0.30}/Al_2O_3$ were produced in four different ways. Free-standing nanoparticles with composition $Pt_{0.70}Rh_{0.30}$ were synthesized the 'round-flask' polyol method and the microwave method, and deposited onto two different support materials, 'boehmite' and '$\gamma$-$Al_2O_3$'. The particles were found to have different dispersions originating from the different synthesis techniques. The dispersion of the free-standing nanoparticles was found to influence all the steps of the deposition; agglomerated free-standing nanoparticles of the 'round-flask' method were poorly dispersed onto the support and sintered to large particles in the μm range during calcination; the well dispersed nanoparticles of the microwave method was well dispersed onto the support after deposition and calcination. For both methods the nanoparticles were only found onto the support, indicating that the nanoparticles attach well to the support. For Cat-PtRh-3 and Cat-PtRh-4 (who had well dispersed nanoparticles), no difference was found for the two support materials ('boehmite' and $\gamma$-$Al_2O_3$) with respect to metal dispersion.

For the Cat-CoRe-x (x = 0, 5, 10 and 15) catalysts obtained in this study the PXD patterns indicated in general little or no presence of metallic cobalt and Re containing phases after calcination and activation at 390 $^{o}$C. The low signal of metallic cobalt obtained for Cat-CoRe-

0 is consistent with literature, however the missing peak in the Cat-CoRe-x (x = 5, 10 and 15) is not understood. This is suggested to be due to the lower loading of cobalt causing the signal to be washed out, or that the metal is not reduced under the conditions given. Fault in synthesis procedure/equipment is not excluded. The lack of PXD signal from rhenium in the samples is assumed to be caused by rhenium not being in a crystalline form or that its diffraction peaks are hidden in the background. The results from PXD patterns obtained for Cat-CoRe-x (x = 5, 10 and 15) were found to be inconclusive.

# 7. Perspectives

To gain more insight into the formation of the $Pt_{1-x}Rh_x$ nanoparticles, statistics on the size of the nanoparticles with respect to different shapes would be interesting, to see if some shapes have larger sizes, and which ratios the different shapes are found (i.e. is some shapes are more preferred than others)

The metal-to-surfactant is known to have an effect on the shapes and sizes of the nanoparticles and therefore research into the effect of different metal-to-surfactant ratios would be interesting. The ratio may also influence the stability of the nanoparticles in solution. With respect to this, the effect of addition of more surfactant in the redispersing media before adding it to the particles would also be interesting to investigate in order to obtain a more stable solution. Sonication has been found to influence stability of the suspension, and this in combination with additional surfactant could increase the stability. It was found that the 'microwave' and 'polyol' route in this work gave rise to different stabilities of the suspension, and therefore additional surfactants and should be investigated for the 'polyol' route used in this work.

In order to obtain more information about the variations seen in the a-axis of different substitution grades of $Pt_{1-x}Rh_x$ some insight into the nucleation mechanism would be useful, with respect to which of the two metal-acetylacetonates are reduced first. Further, careful TEM-STEM-EDS investigations are also tools that can be called for in order to document cluster and or film formation in the bimetallic particles, and may therefore reveal the nucleation mechanism of the particles..

In order to understand the difference in obtained composition of the free standing nanoparticles synthesised for catalyst, and the finished catalyst, more characterisation techniques could be implemented in the different steps of the procedure.

# 8. Appendix

## 8.1 Appendix A

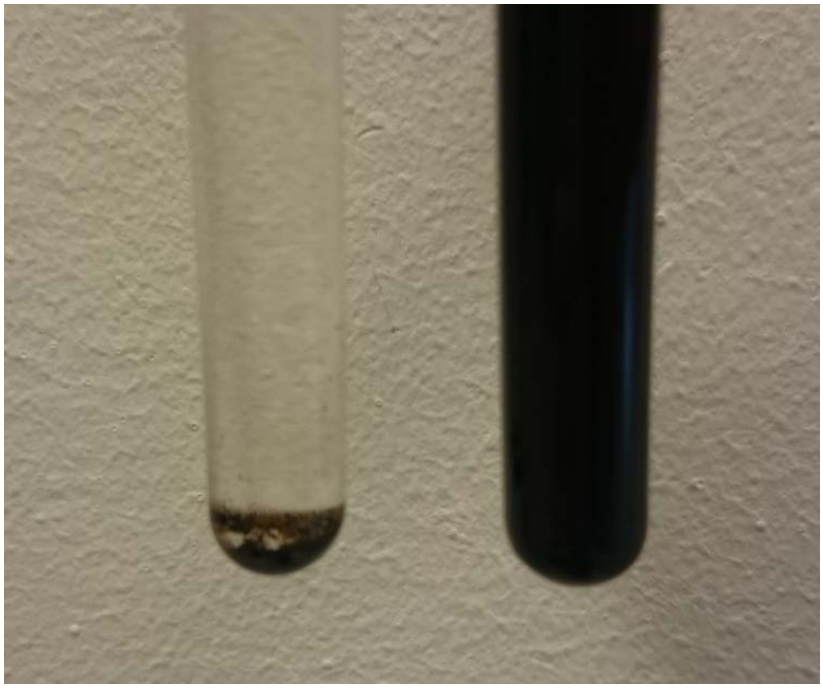

Figur 1. The unacceptable (left) and acceptable (right) stabilities found for the different substitution grades of $Pt_{1-x}Rh_x$ in section 4.1.1

## 8.2 Appendix B

### The mean sizes for each measurement of DLS, with corresponding mean with and the amount of dust seen in each measurement

*The sample with concentration 8.8 mg/mL*

| Measurement: | Mean size | Mean width | % of dust in sample based on peaks at higher nm (above 4000) |
|---|---|---|---|
| 1 | 76 | 46 | n/a |
| 2 | 78 | 51 | n/a |
| 3 | 74 | 46 | 1.7 |
| 4 | 79 | 54 | n/a |
| 5 | 76 | 49 | n/a |
| 6 | 76 | 49 | n/a |

*The sample with concentration 4.2 mg/mL*

| Masurement: | Mean size | Mean witdth | % of dust in sample based on peaks at higher nm (above 4000) |
|---|---|---|---|
| 1 | 82 | 64 | n/a |
| 2 | 72 | 54 | 2,3 |

| | | | |
|---|---|---|---|
| 3 | 81 | 62 | n/a |
| 4 | 79 | 58 | n/a |
| 5 | 72 | 47 | 5,9 |
| 6 | 71 | 43 | 1,8 |

*The sample with concentration 2.9 mg/mL*

| Masurement: | Mean size | Mean witdth | % of dust in sample based on peaks at higher nm (above 4000) |
|---|---|---|---|
| 1 | 136 | 161 | n/a |
| 2 | 134 | 145 | n/a |
| 3 | 119 | 122 | 2,5 |
| 4 | 123 | 136 | n/a |
| 5 | 123 | 144 | n/a |
| 6 | 117 | 129 | n/a |

References


1. Malvern, I., *DLS technical note*.
2. Hitachi High-Technologies Corporation, H., *Let's Femiliarize Ourselves with SEM!* 2013.
3. *http://en.wikipedia.org/wiki/Bragg's_law*. 02.01.2015].
4. F. Fischer, H.T. and 276, *Brennstoff-Chemie. 4.*
5. Tilley, R., *Understanding Solids*, ed. Wiley. 2004.
6. United Nations, o. 2012; Available from: http://esa.un.org/wpp/Demographic-Profiles/index.shtm.
7. Thomas, J.M. and W.J. Thomas., *"Principles and practice of heterogeneous catalysis"*. 1996: Wiley.
8. Rane, S.P., *Relation Between Catalyst Properties and Selectivity in Fischer-Tropsch synthesis*, in *Department of Chemical Engeneering*. 2011, NTNU: Faculty of Natrual Sciences and Technology p. 114.
9. Leksicon, S.N. 05. 11. 2014]; Available from: https://snl.no/katalysator/katalysator_i_forbrenningsmotorer.
10. Schäffer, J., et al., *NO selectivity in NH3 oxidation over supported tailored Pt and Rh nanoparticles*, in *11th European Congress on Catalysis-europacat-XI*. September 1st-6th, 2013: Lyon, France.
11. Biausque, G. and Y. Schuurman, *The reaction mechanism of the high temperature ammonia oxidation to nitric oxide over LaCoO3.* Journal of Catalysis, 2010. **276**(2): p. 306-313.
12. Schäffer, J., et al., *Highly selective ammonia oxidation to nitric oxide over supported Pt nanoparticles.* Journal of Catalysis, 2013. **301**: p. 210-216.
13. Pérez-Ramírez, J. and B. Vigeland, *Lanthanum ferrite membranes in ammonia oxidation: Opportunities for 'pocket-sized' nitric acid plants.* Catalysis Today, 2005. **105**(3–4): p. 436-442.
14. Javier Pérez-Ramírez, B.V., *Perovskite Membranes in Ammonia Oxidation: Towards Process Intensification in Nitric Acid Manufacture.* Angewandte Chemie International Edition. **44**(7): p. 1112-1115.
15. Rafiq, M.H., *Experimental Studies and Modeling of Synthesis Gas Production and Fischer-Tropsch Synthesis*, in *Department of Energy and Process Engineering*. 2012, Norwegian University of Science and Technology.

16. Melaet, G., et al., *Evidence of highly active cobalt oxide catalyst for the Fischer-Tropsch synthesis and CO2 hydrogenation.* Journal of the American Chemical Society, 2014. **136**(6): p. 2260-2263.
17. Rane, S., et al., *Relation between hydrocarbon selectivity and cobalt particle size for alumina supported cobalt Fischer–Tropsch catalysts.* Applied Catalysis A: General, 2012. **437–438**(0): p. 10-17.
18. Rønning, M., et al., *Combined XRD and XANES studies of a Re-promoted Co/γ-Al2O3 catalyst at Fischer–Tropsch synthesis conditions.* Catalysis Today, 2010. **155**(3–4): p. 289-295.
19. Bakken, V., et al., *Bimetallic Cobalt/Rhenium Systems: Preferred Position of Rhenium Through an Interdisciplinary Approach.* Catalysis Letters, 2010. **135**(1-2): p. 21-25.
20. Rytter, E., et al., *Cobalt Fischer−Tropsch Catalysts Using Nickel Promoter as a Rhenium Substitute to Suppress Deactivation.* Industrial & Engineering Chemistry Research, 2010. **49**(9): p. 4140-4148.
21. Enger, B.C., et al., *Modified alumina as catalyst support for cobalt in the Fischer–Tropsch synthesis.* Journal of Catalysis, 2011. **284**(1): p. 9-22.
22. Castleman, A.W. and K.H. Bowen, *Clusters: Structure, Energetics, and Dynamics of Intermediate States of Matter.* Journal of physical chemistry, 1996. **100**(31): p. 12911-12944.
23. Na, K., Q. Zhang, and G.A. Somorjai, *Colloidal Metal Nanocatalysts: Synthesis, Characterization, and Catalytic Applications.* Journal of Cluster Science, 2014. **25**(1): p. 83-114.
24. An, K. and G.A. Somorjai, *Size and Shape Control of Metal Nanoparticles for Reaction Selectivity in Catalysis.* ChemCatChem, 2012. **4**(10): p. 1512-1524.
25. Park, J.Y., et al., *Tuning of catalytic CO oxidation by changing composition of Rh-Pt bimetallic nanoparticles.* Nano Letters, 2008. **8**(2): p. 673-677.
26. Park, J.Y., et al., *Size effect of RhPt bimetallic nanoparticles in catalytic activity of CO oxidation: Role of surface segregation.* Catalysis Today, 2012. **181**(1): p. 133-137.
27. Quek, X.-Y., Y. Guan, and E.J.M. Hensen, *Structure sensitivity in the hydrogenation of unsaturated hydrocarbons over Rh nanoparticles.* Catalysis Today, 2012. **183**(1): p. 72-78.
28. Grass, M.E., et al., *Colloidally Synthesized Monodisperse Rh Nanoparticles Supported on SBA-15 for Size- and Pretreatment-Dependent Studies of CO Oxidation.* The Journal of Physical Chemistry C, 2009. **113**(20): p. 8616-8623.

29. Shen, S.Y., T.S. Zhao, and J.B. Xu, *Carbon supported PtRh catalysts for ethanol oxidation in alkaline direct ethanol fuel cell.* International Journal of Hydrogen Energy, 2010. **35**(23): p. 12911-12917.
30. Stevanovi´c¿, S., et al., *Microwave sinthesys and characterization of Pt and Pt-Rh-Sn electrocatalysts for ethanol oxidation.* Journal of the Serbian Chemical Society, 2011.
31. Patel, K., et al., *Synthesis of Pt, Pd, Pt/Ag and Pd/Ag nanoparticles by microwave-polyol method.* Journal of Chemical Sciences, 2005. **117**(4): p. 311-316.
32. M. Kalyva, H.F., A. O. Sjåstad, , *Manuscript in prep.*
33. Musafumi Harada, C.C., Timako Sada, *XAFS Studies of Metal Nanoparticles Prepared by Using Microwave Heating*. 2011: Photon Factory Activity Report 2011 #29 (2012)
34. (Platinum-Rhodium), P.-R. *Okamoto H., ASM International, Alloy Phase Diagram Section, Materials Park, Ohio, U.S.A.*

. [cited 2014 19.11]; Available from: http://www1.asminternational.org/asmenterprise/APD/ViewAPD.aspx?id=901940, http://x-port.uio.no/V/?func=native-link&resource=UNI11070.
35. M. Ellner, J.L., *Common Met.* . 1981. **78**: p. P21-P32.
36. Manoun, B., et al., *Thermal Expansion of Polycrystalline Ti3SiC2 in the 25°–1400°C Temperature Range.* Journal of the American Ceramic Society, 2005. **88**(12): p. 3489-3491.
37. Korolkov, I.V., A.I. Gubanov, and S.A. Gromilov, *Thermolysis of [Pt(NH3)4][ReHlg6] (Hlg = Cl, Br). Structure refinement for [Pt(NH3)4][ReCl6]*. Journal of Structural Chemistry, 2005. **46**(3): p. 479-487.
38. Online, L.-B.
39. Raub, E., *Metals and alloys of the platinum group.* Journal of the Less Common Metals, 1959. **1**(1): p. 3-18.
40. E. Raub, G.F., Z. Metallkd, 1964. **55**: p. 392-397.
41. Y. V. Shubin, A.V.Z., A. B. Venediktov, S. V. Korenev, Russ., J. Inorg. Chem., 2006. **51**: p. 202-209.
42. M. Nuding, M.E., J. Alloys Compd., 1997. **252**: p. 184-191.
43. M. Ellner, K.K., B. Predel, J. Less-Common Met. , 1991. **170**: p. 171-184.
44. K. J. Schulz, O.A.M., Y. A. Chang, J. Phase Equilib. , 1991. **12**: p. 10-14.

45. webelements. Available from: http://www.webelements.com/periodicity/metallic_radius/.
46. Müller, U., *Inorganic Structural Chemistry* 2. ed. Inorganic Chemistry, ed. Wiley. 2007.
47. Schubert, U., *Synthesis of inorganic materials*. 3rd compl. rev. and enl. ed, ed. N. Hüsing. 2012, Weinheim: Wiley.
48. B.Rogers, S.P., J.Adams, *Nanotechnology*. 2. edtition ed. 2011: CRC Press.
49. Xia, Y., et al., *Formkontrolle bei der Synthese von Metallnanokristallen: einfache Chemie, komplexe Physik?* Angewandte Chemie, 2009. **121**(1): p. 62-108.
50. Van Hove, M.A., *From surface science to nanotechnology.* Catalysis Today, 2006. **113**(3–4): p. 133-140.
51. Tsuji, M., et al., *Microwave-Assisted Synthesis of Metallic Nanostructures in Solution.* Chemistry – A European Journal, 2005. **11**(2): p. 440-452.
52. Mourdikoudis, S. and L.M. Liz-Marzán, *Oleylamine in Nanoparticle Synthesis.* Chemistry of Materials, 2013. **25**(9): p. 1465-1476.
53. Melaet, G., A.E. Lindeman, and G.A. Somorjai, *Cobalt particle size effects in the fischer-tropsch synthesis and in the hydrogenation of CO2 studied with nanoparticle model catalysts on silica.* Topics in Catalysis, 2014. **57**(6-9): p. 500-507.
54. C. B. Murray, S.H.S., H. Doyle, T. Betley, *Monodisperse 3d transition-metal (Co, Ni, Fe) nanoparticles and their assembly into nanoparticle superlattices.* Mrs Bulletin. **26**(12): p. 985-991.
55. Borg, Ø., et al., *Electron Microscopy Study of γ-Al2O3 Supported Cobalt Fischer–Tropsch Synthesis Catalysts.* Catalysis Letters, 2008. **126**(3-4): p. 224-230.
56. Hung, C.M., W.L. Lai, and J.L. Lin, *Removal of gaseous ammonia in Pt-Rh binary catalytic oxidation.* Aerosol and Air Quality Research, 2012. **12**(4): p. 583-591.
57. Santos, P.S., H.S. Santos, and S.P. Toledo, *Standard transition aluminas. Electron microscopy studies.* Materials Research, 2000. **3**: p. 104-114.
58. http://en.wikipedia.org/wiki/Aluminium_oxide#Structure. [cited 02.01.2015.
59. Company, S., *High purity activated aluminas.*
60. Stub, S.Ø., *Syntese og karakterisering av p-type transparente ledende oksider*, in *Chemical institute*. 2013, University of Oslo.
61. D. Brandon, W.D.K., *Microstructural Characterization of Materials* 2. edition ed. 2008: Wiley.
62. Russo, P., *A Practical Minicourse in Dynamic Light scattering*. 2012.

63. Teck, H.H. [cited 2014 26, NOVEMBER]; Available from: http://www.hht-eu.com/cms/41934.html.
64. D.B. Williams, C.B.C., *Transmission Electron Microscopy, A Textbook for Materials Science*. Second ed.: Springer.
65. http://en.wikipedia.org/wiki/BET_theory. [cited 2015 01.12].
66. Analytical, P. [cited 2015 01.12].
67. Cao, A. and G. Veser, *Exceptional high-temperature stability through distillation-like self-stabilization in bimetallic nanoparticles.* Nat Mater, 2010. **9**(1): p. 75-81.
68. Sjaastad, A.O. 2015.